

Open Issues in Heritage Conservation

Lead Guest Editor: Alessio Cascardi

Guest Editors: Salvatore Verre, Stefano De Santis, and Arkadiusz Kwiecien



Open Issues in Heritage Conservation

Advances in Civil Engineering

Open Issues in Heritage Conservation

Lead Guest Editor: Alessio Cascardi

Guest Editors: Salvatore Verre, Stefano De Santis,
and Arkadiusz Kwiecien



Copyright © 2022 Hindawi Limited. All rights reserved.

This is a special issue published in "Advances in Civil Engineering." All articles are open access articles distributed under the Creative Commons Attribution License, which permits unrestricted use, distribution, and reproduction in any medium, provided the original work is properly cited.






Chief Editor

Cumaraswamy Vipulanandan, USA
















Associate Editors

Chiara Bedon , Italy
Constantin Chalioris , Greece
Ghassan Chehab , Lebanon
Ottavia Corbi, Italy
Mohamed ElGawady , USA
Husnain Haider , Saudi Arabia
Jian Ji , China
Jiang Jin , China
Shazim A. Memon , Kazakhstan
Hossein Moayedi , Vietnam
Sanjay Nimbalkar, Australia
Giuseppe Oliveto , Italy
Alessandro Palmeri , United Kingdom
Arnaud Perrot , France
Hugo Rodrigues , Portugal
Victor Yepes , Spain
Xianbo Zhao , Australia

Academic Editors

José A.F.O. Correia, Portugal
Glenda Abate, Italy
Khalid Abdel-Rahman , Germany
Ali Mardani Aghabaglou, Turkey
José Aguiar , Portugal
Afaq Ahmad , Pakistan
Muhammad Riaz Ahmad , Hong Kong
Hashim M.N. Al-Madani , Bahrain
Luigi Aldieri , Italy
Angelo Aloisio , Italy
Maria Cruz Alonso, Spain
Filipe Amarante dos Santos , Portugal
Serji N. Amirkhania, USA
Eleftherios K. Anastasiou , Greece
Panagiotis Ch. Anastasopoulos , USA
Mohamed Moafak Arbili , Iraq
Farhad Aslani , Australia
Siva Avudaiappan , Chile
Ozgur BASKAN , Turkey
Adewumi Babafemi, Nigeria
Morteza Bagherpour, Turkey
Qingsheng Bai , Germany
Nicola Baldo , Italy
Daniele Baraldi , Italy

Eva Barreira , Portugal
Emilio Bastidas-Arteaga , France
Rita Bento, Portugal
Rafael Bergillos , Spain
Han-bing Bian , China
Xia Bian , China
Huseyin Bilgin , Albania
Giovanni Biondi , Italy
Hugo C. Biscaia , Portugal
Rahul Biswas , India
Edén Bojórquez , Mexico
Giosuè Boscato , Italy
Melina Bosco , Italy
Jorge Branco , Portugal
Bruno Briseghella , China
Brian M. Broderick, Ireland
Emanuele Brunesi , Italy
Quoc-Bao Bui , Vietnam
Tan-Trung Bui , France
Nicola Buratti, Italy
Gaochuang Cai, France
Gladis Camarini , Brazil
Alberto Campisano , Italy
Qi Cao, China
Qixin Cao, China
Iacopo Carnacina , Italy
Alessio Cascardi, Italy
Paolo Castaldo , Italy
Nicola Cavalagli , Italy
Liborio Cavaleri , Italy
Anush Chandrappa , United Kingdom
Wen-Shao Chang , United Kingdom
Muhammad Tariq Amin Chaudhary, Kuwait
Po-Han Chen , Taiwan
Qian Chen , China
Wei Tong Chen , Taiwan
Qixiu Cheng, Hong Kong
Zhanbo Cheng, United Kingdom
Nicholas Chileshe, Australia
Prinya Chindaprasirt , Thailand
Corrado Chisari , United Kingdom
Se Jin Choi , Republic of Korea
Heap-Yih Chong , Australia
S.H. Chu , USA
Ting-Xiang Chu , China

Zhaofei Chu , China
Wonseok Chung , Republic of Korea
Donato Ciampa , Italy
Gian Paolo Cimellaro, Italy
Francesco Colangelo, Italy
Romulus Costache , Romania
Liviu-Adrian Cotfas , Romania
Antonio Maria D'Altri, Italy
Bruno Dal Lago , Italy
Amos Darko , Hong Kong
Arka Jyoti Das , India
Dario De Domenico , Italy
Gianmarco De Felice , Italy
Stefano De Miranda , Italy
Maria T. De Risi , Italy
Tayfun Dede, Turkey
Sadik O. Degertekin , Turkey
Camelia Delcea , Romania
Cristoforo Demartino, China
Giuseppe Di Filippo , Italy
Luigi Di Sarno, Italy
Fabio Di Trapani , Italy
Aboelkasim Diab , Egypt
Thi My Dung Do, Vietnam
Giulio Dondi , Italy
Jiangfeng Dong , China
Chao Dou , China
Mario D'Aniello , Italy
Jingtao Du , China
Ahmed Elghazouli, United Kingdom
Francesco Fabbrocino , Italy
Flora Faleschini , Italy
Dingqiang Fan, Hong Kong
Xueping Fan, China
Qian Fang , China
Salar Farahmand-Tabar , Iran
Ilenia Farina, Italy
Roberto Fedele, Italy
Guang-Liang Feng , China
Luigi Fenu , Italy
Tiago Ferreira , Portugal
Marco Filippo Ferrotto, Italy
Antonio Formisano , Italy
Guoyang Fu, Australia
Stefano Galassi , Italy

Junfeng Gao , China
Meng Gao , China
Giovanni Garcea , Italy
Enrique García-Macías, Spain
Emilio García-Taengua , United Kingdom
DongDong Ge , USA
Khaled Ghaedi, Malaysia
Khaled Ghaedi , Malaysia
Gian Felice Giaccu, Italy
Agathoklis Giaralis , United Kingdom
Ravindran Gobinath, India
Rodrigo Gonçalves, Portugal
Peilin Gong , China
Belén González-Fonteboa , Spain
Salvatore Grasso , Italy
Fan Gu, USA
Erhan Güneyisi , Turkey
Esra Mete Güneyisi, Turkey
Pingye Guo , China
Ankit Gupta , India
Federico Gusella , Italy
Kemal Haciefendioğlu, Turkey
Jianyong Han , China
Song Han , China
Asad Hanif , Macau
Hadi Hasanzadehshooiili , Canada
Mostafa Fahmi Hassanein, Egypt
Amir Ahmad Hedayat , Iran
Khandaker Hossain , Canada
Zahid Hossain , USA
Chao Hou, China
Biao Hu, China
Jiang Hu , China
Xiaodong Hu, China
Lei Huang , China
Cun Hui , China
Bon-Gang Hwang, Singapore
Jijo James , India
Abbas Fadhil Jasim , Iraq
Ahad Javanmardi , China
Krishnan Prabhakan Jaya, India
Dong-Sheng Jeng , Australia
Han-Yong Jeon, Republic of Korea
Pengjiao Jia, China
Shaohua Jiang , China

MOUSTAFA KASSEM , Malaysia
Mosbeh Kaloop , Egypt
Shankar Karuppannan , Ethiopia
John Kechagias , Greece
Mohammad Khajehzadeh , Iran
Afzal Husain Khan , Saudi Arabia
Mehran Khan , Hong Kong
Manoj Khandelwal, Australia
Jin Kook Kim , Republic of Korea
Woosuk Kim , Republic of Korea
Vaclav Koci , Czech Republic
Loke Kok Foong, Vietnam
Hailing Kong , China
Leonidas Alexandros Kouris , Greece
Kyriakos Kourousis , Ireland
Moacir Kripka , Brazil
Anupam Kumar, The Netherlands
Emma La Malfa Ribolla, Czech Republic
Ali Lakirouhani , Iran
Angus C. C. Lam, China
Thanh Quang Khai Lam , Vietnam
Luciano Lamberti, Italy
Andreas Lampropoulos , United Kingdom
Raffaele Landolfo, Italy
Massimo Latour , Italy
Bang Yeon Lee , Republic of Korea
Eul-Bum Lee , Republic of Korea
Zhen Lei , Canada
Leonardo Leonetti , Italy
Chun-Qing Li , Australia
Dongsheng Li , China
Gen Li, China
Jiale Li , China
Minghui Li, China
Qingchao Li , China
Shuang Yang Li , China
Sunwei Li , Hong Kong
Yajun Li , China
Shun Liang , China
Francesco Liguori , Italy
Jae-Han Lim , Republic of Korea
Jia-Rui Lin , China
Kun Lin , China
Shibin Lin, China

Tzu-Kang Lin , Taiwan
Yu-Cheng Lin , Taiwan
Hexu Liu, USA
Jian Lin Liu , China
Xiaoli Liu , China
Xuemei Liu , Australia
Zaobao Liu , China
Zhuang-Zhuang Liu, China
Diego Lopez-Garcia , Chile
Cristiano Loss , Canada
Lyan-Ywan Lu , Taiwan
Jin Luo , USA
Yanbin Luo , China
Jianjun Ma , China
Junwei Ma , China
Tian-Shou Ma, China
Zhongguo John Ma , USA
Maria Macchiaroli, Italy
Domenico Magisano, Italy
Reza Mahinroosta, Australia
Yann Malecot , France
Prabhat Kumar Mandal , India
John Mander, USA
Iman Mansouri, Iran
André Dias Martins, Portugal
Domagoj Matesan , Croatia
Jose Matos, Portugal
Vasant Matsagar , India
Claudio Mazzotti , Italy
Ahmed Mebarki , France
Gang Mei , China
Kasim Mermerdas, Turkey
Giovanni Minafò , Italy
Masoomah Mirrashid , Iran
Abbas Mohajerani , Australia
Fadzli Mohamed Nazri , Malaysia
Fabrizio Mollaioli , Italy
Rosario Montuori , Italy
H. Naderpour , Iran
Hassan Nasir , Pakistan
Hossein Nassiraei , Iran
Satheeskumar Navaratnam , Australia
Ignacio J. Navarro , Spain
Ashish Kumar Nayak , India
Behzad Nematollahi , Australia

Chayut Ngamkhanong , Thailand
Trung Ngo, Australia
Tengfei Nian, China
Mehdi Nikoo , Canada
Youjun Ning , China
Olugbenga Timo Oladinrin , United Kingdom
Oladimeji Benedict Olalusi, South Africa
Timothy O. Olawumi , Hong Kong
Alejandro Orfila , Spain
Maurizio Orlando , Italy
Siti Aminah Osman, Malaysia
Walid Oueslati , Tunisia
SUVASH PAUL , Bangladesh
John-Paris Pantouvakis , Greece
Fabrizio Paolacci , Italy
Giuseppina Pappalardo , Italy
Fulvio Parisi , Italy
Dimitrios G. Pavlou , Norway
Daniele Pellegrini , Italy
Gatheeshgar Perampalam , United Kingdom
Daniele Perrone , Italy
Giuseppe Piccardo , Italy
Vagelis Plevris , Qatar
Andrea Pranno , Italy
Adolfo Preciado , Mexico
Chongchong Qi , China
Yu Qian, USA
Ying Qin , China
Giuseppe Quaranta , Italy
Krishanu ROY , New Zealand
Vlastimir Radonjanin, Serbia
Carlo Rainieri , Italy
Rahul V. Ralegaonkar, India
Raizal Saifulnaz Muhammad Rashid, Malaysia
Alessandro Rasulo , Italy
Chonghong Ren , China
Qing-Xin Ren, China
Dimitris Rizos , USA
Geoffrey W. Rodgers , New Zealand
Pier Paolo Rossi, Italy
Nicola Ruggieri , Italy
JUNLONG SHANG, Singapore

Nikhil Saboo, India
Anna Saetta, Italy
Juan Sagaseta , United Kingdom
Timo Saksala, Finland
Mostafa Salari, Canada
Ginevra Salerno , Italy
Evangelos J. Sapountzakis , Greece
Vassilis Sarhosis , United Kingdom
Navaratnarajah Sathiparan , Sri Lanka
Fabrizio Scozzese , Italy
Halil Sezen , USA
Payam Shafigh , Malaysia
M. Shahria Alam, Canada
Yi Shan, China
Hussein Sharaf, Iraq
Mostafa Sharifzadeh, Australia
Sanjay Kumar Shukla, Australia
Amir Si Larbi , France
Okan Sirin , Qatar
Piotr Smarzewski , Poland
Francesca Sollecito , Italy
Rui Song , China
Tian-Yi Song, Australia
Flavio Stochino , Italy
Mayank Sukhija , USA
Piti Sukontasukkul , Thailand
Jianping Sun, Singapore
Xiao Sun , China
T. Tafsirojjaman , Australia
Fujiao Tang , China
Patrick W.C. Tang , Australia
Zhi Cheng Tang , China
Weerachart Tangchirapat , Thailand
Xiixin Tao, China
Piergiorgio Tataranni , Italy
Elisabete Teixeira , Portugal
Jorge Iván Tobón , Colombia
Jing-Zhong Tong, China
Francesco Trentadue , Italy
Antonello Troncone, Italy
Majbah Uddin , USA
Tariq Umar , United Kingdom
Muahmmad Usman, United Kingdom
Muhammad Usman , Pakistan
Mucteba Uysal , Turkey

Ilaria Venanzi , Italy
Castorina S. Vieira , Portugal
Valeria Vignali , Italy
Claudia Vitone , Italy
Liwei WEN , China
Chunfeng Wan , China
Hua-Ping Wan, China
Roman Wan-Wendner , Austria
Chaohui Wang , China
Hao Wang , USA
Shiming Wang , China
Wayne Yu Wang , United Kingdom
Wen-Da Wang, China
Xing Wang , China
Xiuling Wang , China
Zhenjun Wang , China
Xin-Jiang Wei , China
Tao Wen , China
Weiping Wen , China
Lei Weng , China
Chao Wu , United Kingdom
Jiangyu Wu, China
Wangjie Wu , China
Wenbing Wu , China
Zhixing Xiao, China
Gang Xu, China
Jian Xu , China
Panpan , China
Rongchao Xu , China
HE YONGLIANG, China
Michael Yam, Hong Kong
Hailu Yang , China
Xu-Xu Yang , China
Hui Yao , China
Xinyu Ye , China
Zhoujing Ye, China
Gürol Yildirim , Turkey
Dawei Yin , China
Doo-Yeol Yoo , Republic of Korea
Zhanping You , USA
Afshar A. Yousefi , Iran
Xinbao Yu , USA
Dongdong Yuan , China
Geun Y. Yun , Republic of Korea







Hyun-Do Yun , Republic of Korea
Cemal YİĞİT , Turkey
Paolo Zampieri, Italy
Giulio Zani , Italy
Mariano Angelo Zanini , Italy
Zhixiong Zeng , Hong Kong
Mustafa Zeybek, Turkey
Henglong Zhang , China
Jiupeng Zhang, China
Tingting Zhang , China
Zengping Zhang, China
Zetian Zhang , China
Zhigang Zhang , China
Zhipeng Zhao , Japan
Jun Zhao , China
Annan Zhou , Australia
Jia-wen Zhou , China
Hai-Tao Zhu , China
Peng Zhu , China
QuanJie Zhu , China
Wenjun Zhu , China
Marco Zucca, Italy
Haoran Zuo, Australia
Junqing Zuo , China
Robert Černý , Czech Republic
Süleyman İpek , Turkey

Contents




A Multiplex Conversion of a Historical Cinema

Alessio Cascardi , Salvatore Verre , Alessandra Sportillo, and Gaetano Giorgio
Research Article (15 pages), Article ID 2191315, Volume 2022 (2022)

An Alternative Method for Long-Term Monitoring of Thai Historic Pagodas Based on Terrestrial Laser Scanning Data: A Case Study of Wat Krachee in Ayutthaya

Peerasit Mahasuwanchai , Chainarong Athisakul , Phasu Sairuamyat , Weerachart Tangchirapat ,
Sutat Leelataviwat , and Somchai Chucheepsakul 
Research Article (17 pages), Article ID 5587046, Volume 2021 (2021)

A New Artificial Neural Network Model for the Prediction of the Effect of Molar Ratios on Compressive Strength of Fly Ash-Slag Geopolymer Mortar

Shaish K. John, Alessio Cascardi , Yashida Nadir , Maria Antonietta Aiello , and K. Girija
Research Article (17 pages), Article ID 6662347, Volume 2021 (2021)

Study on the Seismic Performance of Small-Diameter Bolts Reinforced in Grottoes

Ningbo Peng , Bo Sun , Jizhong Huang , Yun Dong , and Ye Zhu 
Research Article (12 pages), Article ID 5550648, Volume 2021 (2021)

Research Article

A Multiplex Conversion of a Historical Cinema

Alessio Cascardi ¹, Salvatore Verre ², Alessandra Sportillo,³ and Gaetano Giorgio⁴

¹ITC-CNR National Council of Research, Sede Secondaria di Bari-70124, Italy

²University of Calabria, Rende-87036, Italy

³University of Salento, Lecce-73100, Italy

⁴Studio “Giorgio&Partners”, Toritto-70020, Italy

Correspondence should be addressed to Alessio Cascardi; alessio.cascardi@itc.cnr.it

Received 10 June 2021; Revised 25 January 2022; Accepted 24 February 2022; Published 16 March 2022

Academic Editor: Andreas Lampropoulos

Copyright © 2022 Alessio Cascardi et al. This is an open access article distributed under the Creative Commons Attribution License, which permits unrestricted use, distribution, and reproduction in any medium, provided the original work is properly cited.

The cultural building Heritage is a valuable trace of the past social life in a city. One peculiar typology of building is the theatre or, more recently, the cinema. Within this indoor space, the community of people actively live an emotional feeling over the time causing memories linked to not only the show itself, but also to the place. Furthermore, cinemas are often located in city centers where buildings are historical-oriented form the architectural point of view and, for this reason, their added-value needs to be recognized. Currently, the modernization and the improvement of old cinemas is becoming an interesting topic in the field of civil engineering. In order to empathize this aspect, the structural strengthening for a multiplex conversion of an historical cinema is herein reported. The studied structure required a seismic joint (separating the masonry to the reinforced concrete structural bodies) and a severe strengthening of a very long span beam due to a relevant overloading (in seismic loads combination) caused by the new architectonical project. The numerical simulations demonstrated the validity of two bending strengthening systems (i.e. Fiber Reinforced Polymer-plate and *Beton Plaquè*) in terms of both load bearing capacity and maximum deflection. This overview is a part of a larger study in the way of a global structural interventions which will also involve the masonry members.

1. Introduction

Currently, the construction business is more oriented on the conservation, strengthening and regeneration of existing buildings instead of new constructions. This aspect is particularly felt in the case of the social and cultural building Heritage. In fact, the public buildings often cannot be erected in new places since the serviceability and the accessibility are linked aspects. Thus, the structures located in city centers need to be focused. An example is the cinema/theatre. In Italy, there are many cases of old cinemas which are now abandoned because not able to cover the modern demand from the public anymore. In fact, the structures are often ancient from the normative point of view (e.g. in seismic capacity) and the projection rooms are inadequate in terms of both the technology and the dimensions/capacity. In order to reuse this important Heritage, the seismic update is mandatory while a more functional architectonic project is

attended. Therefore, the structural analysis involves many action steps: geometrical and structural survey (diagnostic), global analysis *ante-operam*, choice of the strengthening interventions, design, global analysis *post-operam* and monitoring according to the ISCARSAH's Recommendations and many other cases study, [1–6].

In the past decades, there were many examples of cinema reconversions or updating, [7]. For example, in Italy many cinemas were converted into multiplexes in the 2000s following major renovations: the *Cinema Massimo* in Turin, the *Cinema Orfeo* in Milan and the *Cinema Massimo* in Lecce. In particular, the *Cinema Massimo* in Turin was built in the 1930s and had only one auditorium with 1000 seats capacity. It was re-designed a few years later due to the bombings of 1942 (II World War). Following the crisis of the 1980s, the cinema was closed and re-opened in 2001 after a renovation. Currently, the *Cinema Massimo* is arranged into three projection rooms: one with 453 seats and two with 147 seats.

The *Cinema Orfeo* in Milan was opened in 1936 and damaged in 1943 by bombing (again during the II World War). It had a single 2500-seats auditorium and was considered for many years the largest cinema in Milan and among the largest in Europe. In 2004, following a renovation, the cinema was converted into a multiplex with three new rooms: one with 720 seats and two with 290 seats. Finally, the construction of the *Cinema Massimo* in Lecce began in 1939, but it was interrupted during the II World War, only to be resumed later. At the beginning, it had only one theatre with 700 seats. Towards the end of the 1990s, renovation work occurred and the cinema was converted into a multiplex with five auditoriums: one with 675 seats and an opening roof, two auditoriums with 150 seats, one with 144 seats and the last one with 130 seats.

In the present paper, the case-study of the ex “*Supercinema*” in *Trani* is reported and discussed. The study is new and the findings are original. The peculiarities of the selected building are recognizable in its mixed-structure (almost half masonry and half reinforced concrete made) and the presence of a very long-span beam which is the target of a *Finite Element* (FE) analysis herein performed.

2. Descriptions of the Building

The so called *Supercinema* is placed in the center of the *Trani*, a quite small city in the south of Italy (see Figure 1(a)). The structure consists in two adjacent bodies of a different construction system: masonry and reinforced concrete (RC) as illustrated in Figure 1(b). An intermediate floor makes the conjunction of the two bodies.

Passing throughout the main entrance, according to the original functional conception (Figure 2(a)), the building has a load-bearing masonry structure, consisting of two elevations above the ground. At the ground floor, the one used for the cinema/theatre purpose, an entrance hall is dominating the space; while a small projection room (Figure 2(b)) is on the left opposite to the offices and the toilets. The roofs of the first level are barrel vaults, with a maximum height of 5.20 m. Before entering into the theatre, a short-lived of the transition area under the conjunction floor is found. It is a single-story area consisting of a connecting slab. Here, a corner bar is located (Figures 2(c) and 2(d)). The RC-building which houses the theatre consists of three floors above ground and one basement, all of them can be accessed by stairs located at the corners. On the ground floor there is the stage and the stalls, currently without seats, while on the first and second floors there are two galleries that will be converted into recreational areas (on the first floor) and three additional halls (on the second floor) as better shown in the next sections. When entering within the “core” of the theatre, a very long span beam, supported on octagonal cross section columns, dominate the structural behavior and the architectural view (Figure 2(e)). The mentioned span is about 14 m and, therefore, much longer than the others, which have an average length of 4.00 m. For this reason, a series of transversal beams were constructed in order to limit the potential mid-span deflection (Figures 2(f) and 2(g)). The other beams are

supported by prismatic cross section columns (Figure 2(h)). The whole photos views are reported in Figure 2 in order to make the understanding of the building conceptual design cleaner and easier.

There were about two thousand seats, which are currently dismantled. The floor height of the stalls ranging between 6.00 m to 9.90 m, while the height of the galleries on the second and third floors is about 2.75 m. Instead, the height of the stage is 12.00 m.

2.1. Territorial Framework. *Trani* is located on the Adriatic coast, 45 km north from the capital city of Bari. Together with *Andria* and *Barletta*, it makes one of the six provincial capitals of the *Apulia* region. According to an ancient legend, the name *Trani* is linked to *Tyrrhenus*, son of the Greek mythological hero *Diomedes*, who founded the city in the 3rd century a.C. However, some modern scholars have established two different hypotheses regarding the origin of the name: the first is that *Trani* may be the shortened form of *Trajan* (a name that may have been given to the city in honor of the Roman Empire) and the second is that the name derives from the medieval term “*trana*”, which indicated an inlet suitable for fishing: an inlet that currently corresponds to the city port. In urban terms, *Trani* is divided into three main areas:

- (1) The historic center, surrounded by huge masonry walls by 1846, embellished by palaces and historical monuments, as well as, by narrow and winding streets. It is the most characteristic area of the city, close to the port and the cathedral.
- (2) Nineteenth-century village, a wealthy and aristocratic area, characterized by villas and palaces of the period. The *Supercinema* falls within this area.
- (3) A residential and modern area, which grew rapidly at the beginning of the 20th century due to the expansion of the city. It branches off beyond the 19th-century village, mainly to the south towards *Bisceglie* and from the 1950s also to the west towards *Andria* and *Corato*. There were no expansion northwards towards *Barletta* due to the presence of the industrial area.

2.2. Historical Background. The *Supercinema* was commissioned by Giuseppe Boccasini, who had returned to *Trani* after had success in America, Domenico Di Mango, foreman of the Aswan dam and an expert in reinforced concrete structure, Domenico Persano, a large landowner from Lecce, and Nicola Guacci, stationmaster, with his wife Lucia Laurora. The Figure 3(a) shows the principals of the *Supercinema* at the early-stage construction. The on-site activities began in 1934 under the supervision of the engineer Enrico Bovio and the inauguration took place the following year, arousing great amazement from the *Trani* public and numerous foreigners who flocked to the town to see a film in the area’s first state-of-the-art cinema, even though it was the only cinema with about two thousand seats (see Figure 3(b)).

The theatre has undergone several modifications:



FIGURE 1: The SUPER CINEMA in Trani: (a) front view and (b) structure typologies individuation.

- (i) in 1991 the renovation of the installations, the stage and the dressing rooms;
- (ii) in 1991 the construction of a false ceiling;
- (iii) in 1995 the general renovations and adaptations;
- (iv) in 2002 the construction of a new hall to replace the second gallery and the conversion of an internal room into a projection room.

However, it has now been closed since 2008 and subjected to historical and architectural restrictions. Lastly, in April 2019, the removing of the asbestos roof was performed.

2.3. In-Situ Surveys. The accuracy of a structural strengthening design is based, above all, on the initial knowledge mining phase, by carrying out a preliminary test campaign that investigates the mechanical properties of the construction materials, the geometry, the state of decay, the level of damage, etc. According to Italian code NTC 2018 [8, 9], based on the quantity and the typology (destructive or not destructive) of the investigations carried out in the cognitive phases, a certain LC (*Level of Confidence*) is reached. The LC has three options: LC1, LC2 and LC3. As a congruence, a corresponding partial factor is identified, namely the CF (*Confidence Factors*), which can assume the value of 1.35, 1.2 and 1 respectively. The aspects that define the levels of confidence are: geometry of the structure, construction details, material properties, connections between the various elements and their presumed modes of collapse. The confidence factor is used for the reduction of the average values of the mechanical parameters from in-situ tests (e.g. strength of the materials) and must be understood as indicators of the

level of detailing achieved. Concerning the herein reported case-study, only the RC building was investigated by performing non-destructive tests. Instruments used were the pacometer, the thermo-camera and the combined *SonReb* test. Therefore, the investigations were limited at that moment providing a LC1 and a $FC = 1.35$. More details of the diagnosis are reported in the following sections.

2.3.1. Pacometer. In the *Supercinema*, the pacometric tests were carried out on the beam with a 13.9 m span and on the 30×35 cm rectangular cross section columns near the exits on the opposite side of the platform. By referring to the beam (see Figure 4), the recordings revealed that the cross section has uniform concrete cover with 1–2 cm thickness, a total of $5\Phi 20$ bottom longitudinal reinforcement rebars and $\Phi 8/30$ cm stirrups, although the span was not constant. The upper longitudinal reinforcement was assumed equal to $2\Phi 20$ to be on the conservative side. On the other hand, the column (see Figure 5) figured out an almost uniform concrete cover with 1–2 cm thickness, a set of $3\Phi 20$ longitudinal rebars per side and $\Phi 8/35$ cm arranged for transversal reinforcement.

2.3.2. SonReb. The in-situ compressive strength of the concrete can be influenced by numerous factors, such as carbonation, amount of internal reinforcing steel, as well as, their location and/or the aggregate size. It is well-known that the most accurate compressive strength estimation can be determined by combining different testing techniques. For example, the correlation of data from the *Schmidt hammer* and *ultrasonic tester* to the existing compressive strength

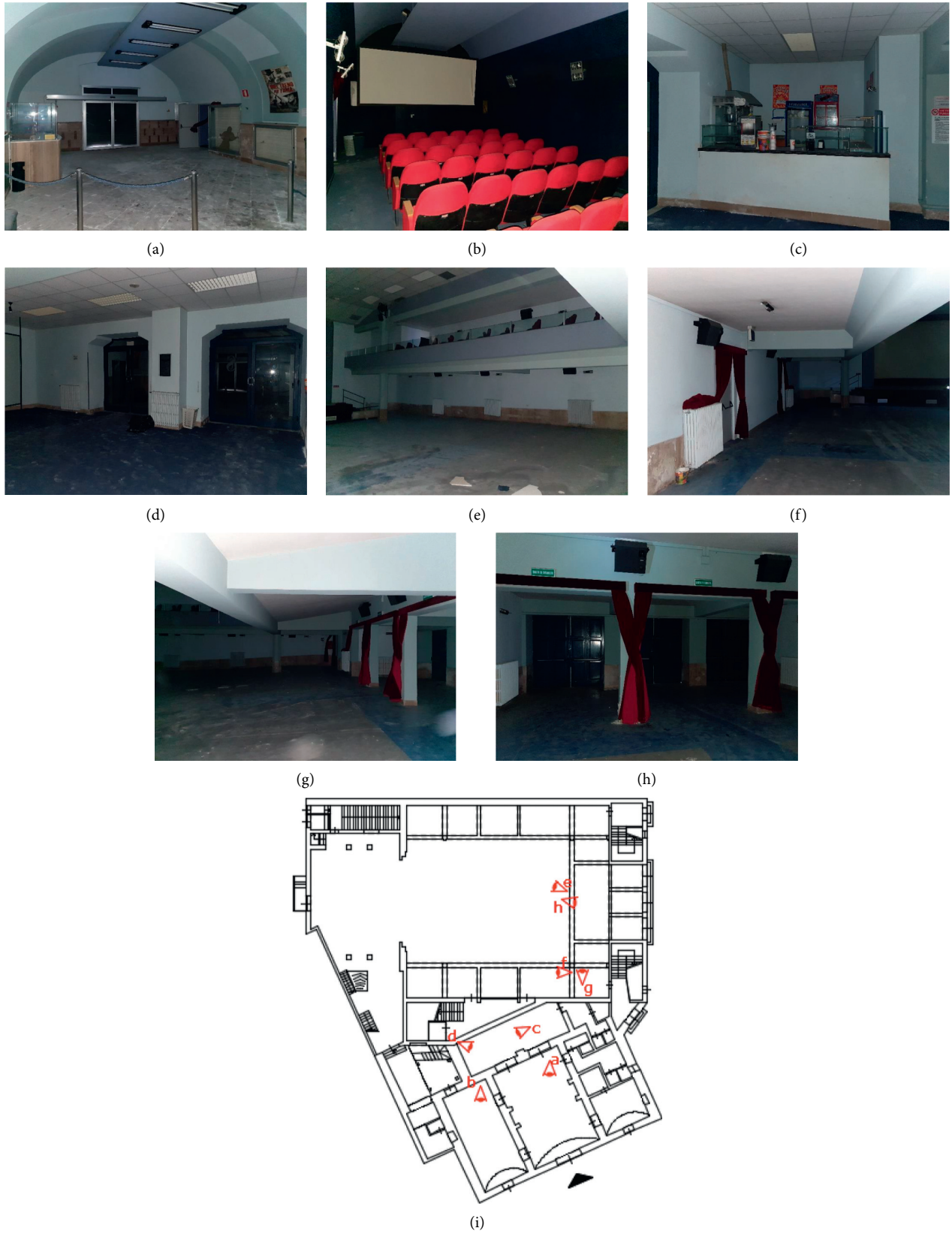


FIGURE 2: (a-h) inside photos and (i) plan with trigger points.



FIGURE 3: Historical photos: principals (a) and original structure design (b).

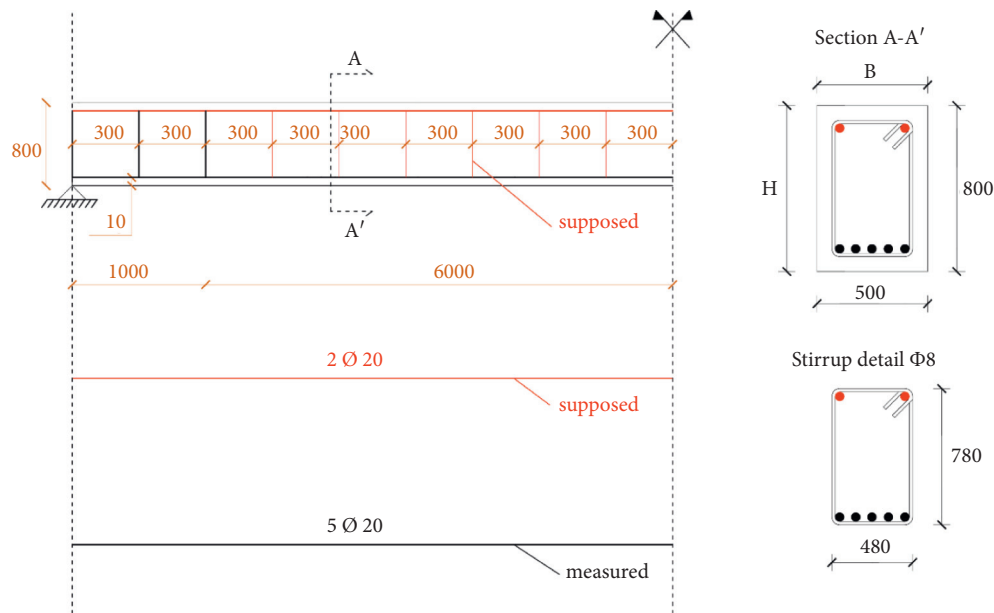


FIGURE 4: Identification of internal reinforcing bars of the very long span beam: cross section (a) and longitudinal section (b).

data is one of the most accurate predictor investigations. Researchers have developed an algorithm whereby the rebound value from the Schmidt hammer and the compression wave velocity from the ultrasonic test can be correlated with actual compressive strength of the concrete. The correlation of the different testing methods with actual compressive strength is commonly known as the SONREB (i.e. SONic REBound) method. The conducted investigation in the *Supercinema* were performed on a series of two beams and four columns and provided an average compressive strength of the concrete equal to ~23 MPa. The measures had a scatter <10%, thus no more investigations were needed since the quality of the concrete can be considered uniform in the RC structure.

2.3.3. *Thermo-Camera*. The area in front of the bar (see again Figures 2(c) and 2(d)) was roofed with a horizontal floor covered by a plastic-based countertop. The latter, when partially removed, allowed to point out the thermo-camera. The result is shown in Figure 6. A floor connecting the masonry and RC structures emerged by the difference in temperature. It is evident the scheme of the joists (at 9–10°C) and the brick pots (at 14–16°C). This floor was joined to the structures by a simply supported lateral beams (Figure 7). Furthermore, using a laser meter, it was discovered that the soffit of the floor is at an intermediate height between the soffit of the masonry building and the soffit of the reinforced concrete building according to Figure 8.

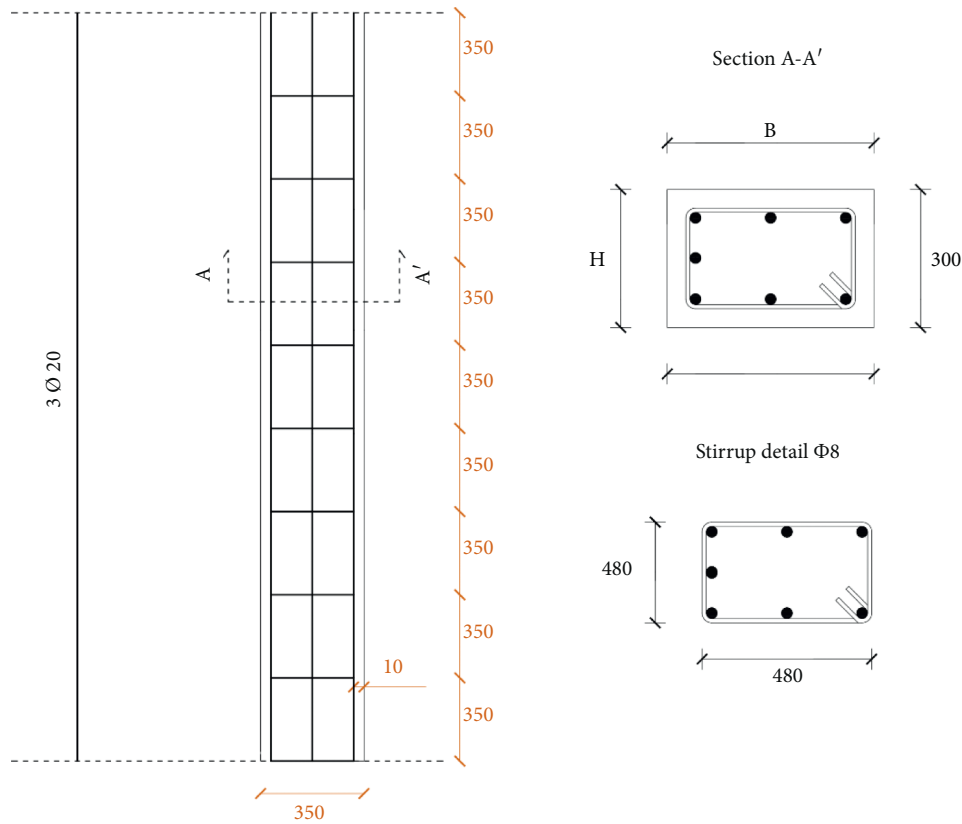


FIGURE 5: Identification of internal reinforcing bars of the column: cross section (a) and longitudinal section (b).

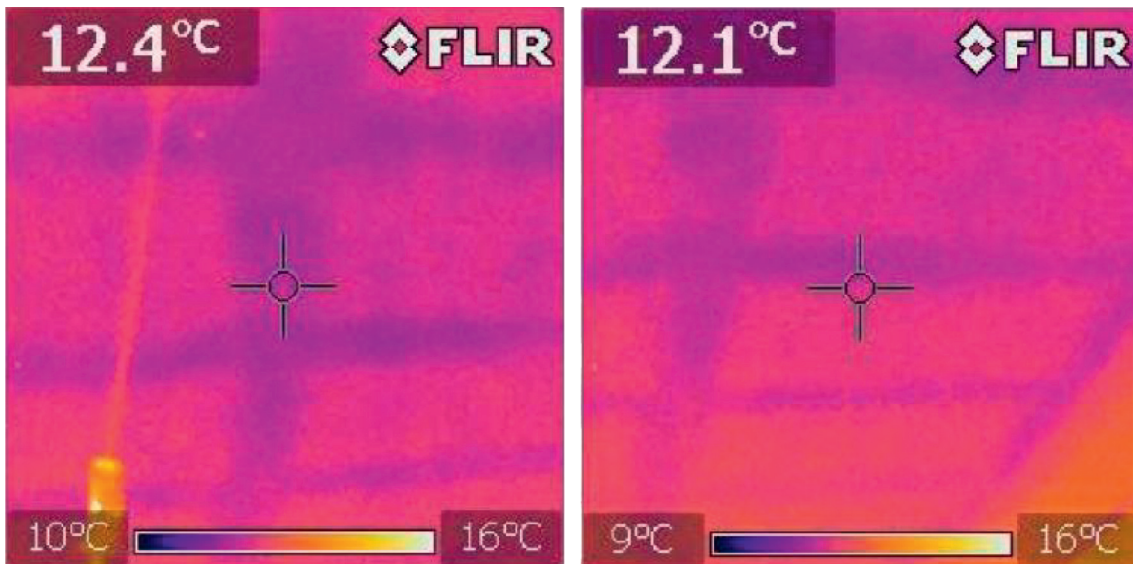


FIGURE 6: Thermo camera outcomes.

3. Architectural Project

The *Supercinema* is intended to be converted from a cinema-theatre to a multiplex with five projection rooms (three new) and different areas for entertainment and/or alternative service. While, the layout and functionality of the individual rooms within the masonry building are planned to be

maintained unaltered according to Figure 9. So, an entrance with a box office and bar corner, the auditorium (ROOM 2), the office and a bookshop corner are prepared. On the ground floor of the reinforced concrete building, the stalls in ROOM 1 will be renovated. On the first floor (see Figure 10), the galleries to the side of the stage will be converted into an alternative use of the space with tables and chairs, while the

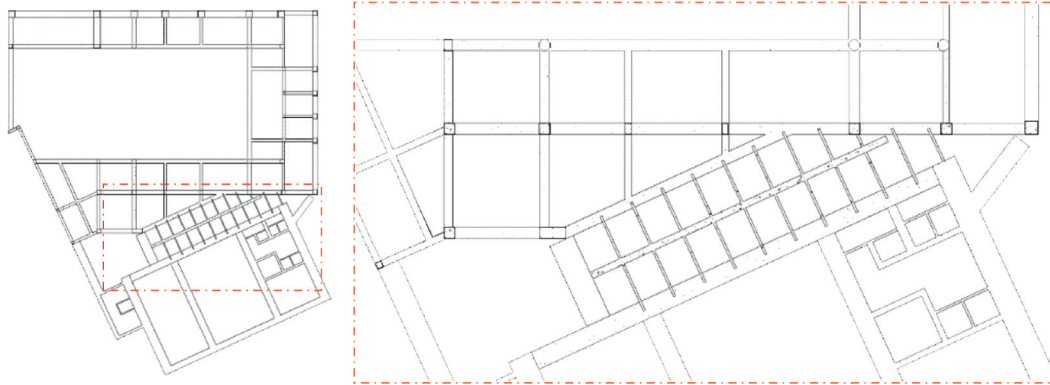


FIGURE 7: Detail of the connecting floor: identification (a) and zoom (b).

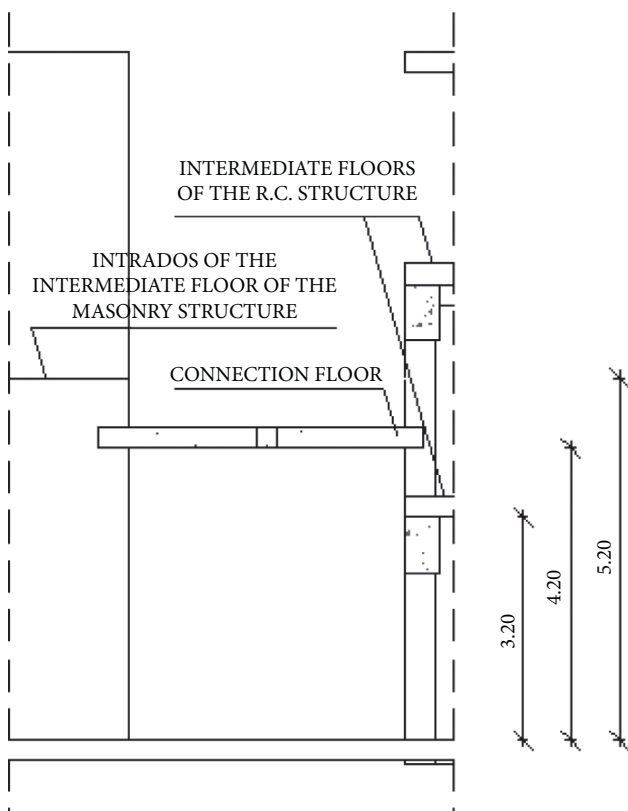


FIGURE 8: Transversal view of the connecting floor.

one in front of the stage will remain in its original function. On the second floor, the galleries at the side of the stage will become two halls (ROOM 3 and ROOM 4) following the 1.80 m extension of the ceiling, while the one at the front will become an additional hall (ROOM 5) as shown in Figure 11. Furthermore, toilets for the disabled and lift shafts will be added. The architectural design envisages seating arrangements as follows: 54 seats for ROOM 2, 416 seats for ROOM1, 56 seats for the first-floor gallery, 58 for ROOMS 3 and 5 and 63 for ROOM 4, for a total of 705 seats. A few render views are illustrated in Figure 12 in order to give and idea of the project when completed.

Expanding the floor between the second and third decks in order to create three new halls at the current galleries

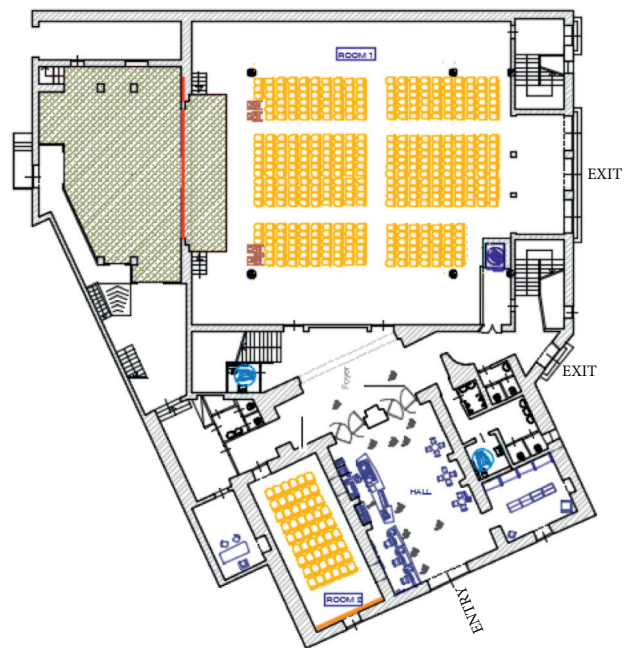


FIGURE 9: Ground floor layout.

means a higher load due to both crowding and the presence of seats that will act at along the almost 14 m long span of the beam which is already poorly reinforced. Therefore, in the following paragraphs, the bending behavior of the beam is studied, constrained at the ends by two simply supports in order to maximize the deflection in the middle-span cross section. Moreover, the strengthening is also simulated. In particular, the beam was studied using finite element software, i.e. MIDAS FEA NX [10], and the bending reinforced was proposed because of the Superintendence advised against the construction of a new support column at the middle span of the overloaded beam. In this scenario, the use of composite materials, i.e. carbon fiber plate (CFRP-Carbon Fiber Reinforced Polymer) installed on the intrados, is a suitable solution by taking advantage of their lightness, high mechanical strength and high resistance to corrosion. In addition, reinforcement was also studied using metal reinforcement plate on the intrados and extrados of the beam, connected by connectors.

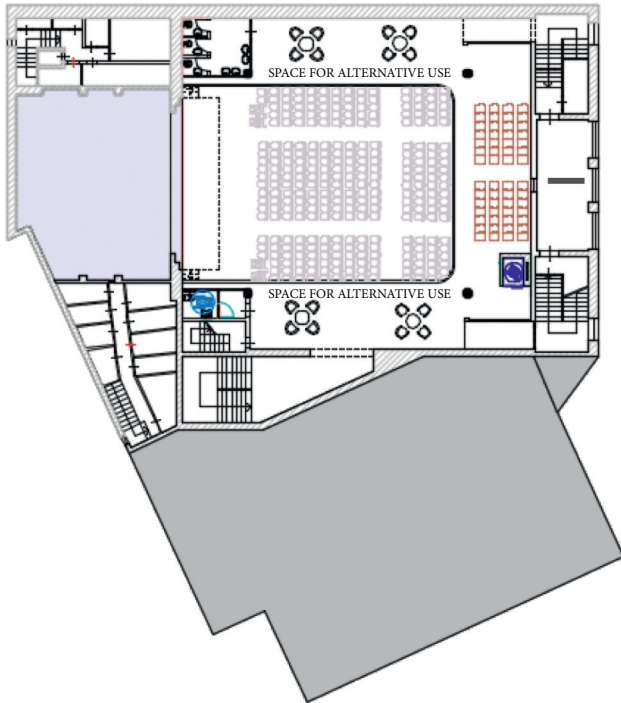


FIGURE 10: First floor layout.

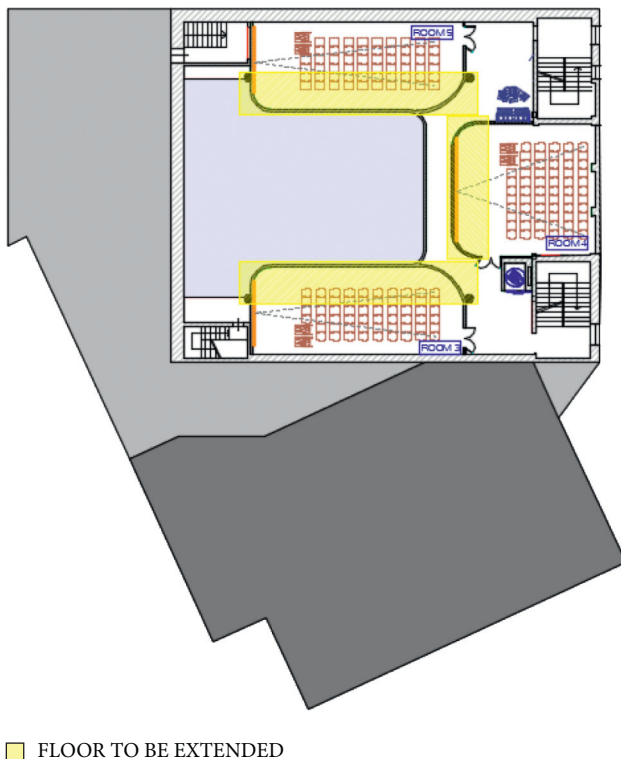


FIGURE 11: Second floor layout.

4. Seismic Upgrading Project

Transforming the cinema into a multiplex, changing the serviceability load of the building, does not only mean architecturally designing the arrangement of the rooms, but

also possibly increasing the demand of a structural element; therefore, the bending behavior of the beam on which the floor to be extended was studied and its structural reinforcement was designed. With the help of Autodesk Revit software [11], which uses the BIM (*Building Information Modeling*) methodology, starting from the architectural model (Figure 13(a)), the structural model (Figure 13(b)) was built with the structural elements (beams and columns) with their reinforcements and load-bearing walls.

Since the masonry building has not been investigated and since the two structures are made of different construction materials, a seismic joint was designed for separating the two bodies and avoids the phenomenon of hammering in the event of an earthquake. Particular attention must be focused when two buildings are placed next to each other, since in the event of seismic action they will have a different response in terms of lateral displacement depending on their mass and stiffness despite being subjected to the same ground acceleration since having a different and independent vibrating mode. Therefore, the joint must ensure an adequate reciprocal distance between two adjacent buildings, whether new or existing. This distance was foreseen in the design phase by calculating the displacements, due to seismic action, of the points of the constructions facing each other and respecting the minimum limits foreseen by the technical regulations. According to the NTC 2018, a distance between two adjacent constructions must be ensured such as to avoid hammering, which is equal to:

$$\frac{1}{100} \cdot \frac{2 \cdot a_g \cdot S}{g} \cdot h. \quad (1)$$

With:

- (i) h building height;
- (ii) a_g maximum horizontal acceleration at the site;
- (iii) g acceleration of gravity;
- (iv) S coefficient considering the subsoil category and typographical conditions, equal to: $S = S_S \cdot S_T$;
- (v) S_S stratigraphic amplification coefficient;
- (vi) S_T topographic amplification coefficient.

To calculate the maximum horizontal acceleration at the site, the parameters related to the site were considered as following listed down:

- (i) nominal life (50 years);
- (ii) class of use (III);
- (iii) reference life (75 years);
- (iv) spectrum (SLV 10%);
- (v) probability of exceeding the reference life (10%);
- (vi) return period (712 years).

The outcomes are reported in Table 1.

A minimum distance between the two buildings of 4 cm was computed. As can be seen in Figure 14, in order to separate the two buildings (red line), the load-bearing walls need to be cut (indicated by the green hatching), a 30 cm

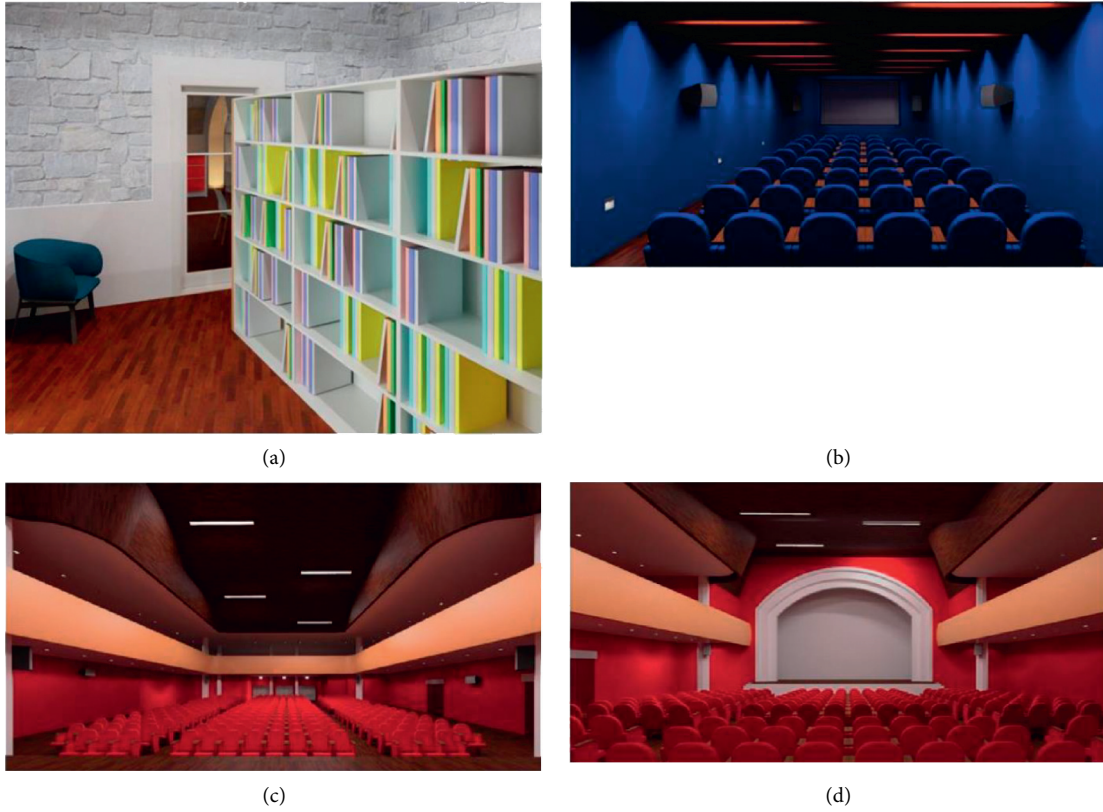


FIGURE 12: Render simulation of the Supercinema: (a) recreation area, (b) ROOM2 and (c-d) ROOM1.

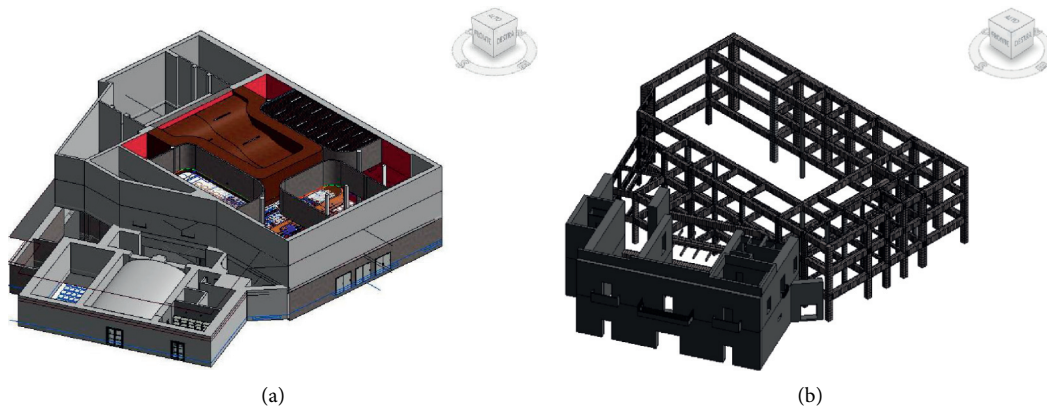


FIGURE 13: Supercinema: (a) architecture and (b) structure evidences.

TABLE 1: Seismic data.

h	S_s	S_T	a_g/g	F_o	T_c
[m]	[-]	[-]	[-]	[-]	[s]
9.90	1.20	1.00	0.107	2.5	0.37

beam is created (indicated by the yellow hatching) on which the connecting floor will rest, and 3 rectangular 50×30 cm pillars and 1 trapezoidal pillar are built (indicated by the blue hatching).

The use of BIM was useful in the transition from the architectural model to the structural model in order to better

understand the *skeleton* of the two structures and to be able to produce the joint in a feasible way. The global behavior of the structure was studied using the PRO_SAP [12] calculation software in order to evaluate and verify the principal stresses. Only the reinforced concrete building was modelled by inserting beams, columns and floor frames. The

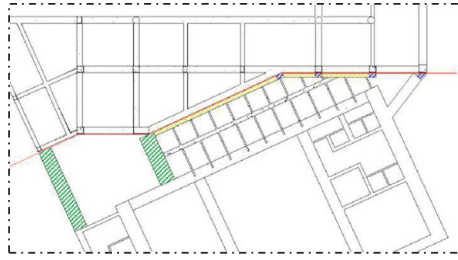


FIGURE 14: Seismic joint location.

constraints were perfect fixed type. The model and the acting stresses represented in the Figure 15(a) and 15(b) were obtained. It is evident as the critical element is the very long span beam, which figured out the maximum bending stress (see redo color in Figure 15(b)). In particular, the value of the load acting on the beam, with the most unfavorable combination (seismic combination), is 52.89 kN/m: this value was then inserted as a uniformly distributed load on the beam span to carry out the analyses with the Midas FEA NX software.

5. Local Beam

The bending deficiency of the *very long span beam* (VLSB), about 14 m, was before mentioned. The problem is related to two main aspects: the high sustained load on the span itself ratio and the poor-quality concrete with the modest internal steel strengthening (both stirrups and longitudinal steel rebars). Therefore, the bending strengthening was focused on the *External Bonded* (EB) systems and designed by means of *Finite Element Method* (FEM). In particular the use of laminate plates was considered by comparing two different materials: carbon (CFRP - *Carbon Fiber Reinforced Polymer*) and steel (BP - *Beton Plaqué*). The numerical procedure was assessed using the commercial code MIDAS FEA NX [10]. It is in the knowledge of the authors that the majority of the RC beams tested in the laboratory have a length ranging in 3–5 m according to the literature, [13–16]. In particular, the adopted test setup is simply supported with punctual applied load (P) in almost all cases. In [17] it is possible to observe the continuous (on three supports) RC beams with an exceptional length of 8.5 meters, but the test setup adopted reported the RC beams with two bending spans of 4.25 m. In [18] it is possible to observe different boundary conditions, at one end the RC beams was clumped while at the other end a torsional constraint in order to test beams at torsion. Definitely, the literature regarding the case study presented in this work (type applied load and the entire RC beam long) is poor.

5.1. Geometrical Modelling and Boundary Conditions. The beam was three-dimensions (3D) modelled in order to replicate the entire beam in the most reliable way. Since the imposed load was full-gravitational oriented, the end constraints were simulated to be reactive only against the vertical translation. In addition, one of the ends constraints was also set to avoid the horizontal translation in the perspective of

numerically consider an isostatic structural member. However, the considered beam was a continuous element simply supported by many columns (more than two), the static schema was assumed to be the uniformly distributed load on two simply supports, in order to emphasize the deflection in the middle of the beam given the high span of about 14.0 m. It is felt by the authors that the choice is consistent with the real case study since the critical span was highly longer than the others while the overloading is acting only on it. Moreover, the limited number of the internal rebars, associated to their level of corrosion, are both factors indicating that a rotation at the ends of the VLSB is potentially reliable and, anyway, on the conservative side. The geometry and the internal reinforcement are both illustrated in Figure 4. This modelling technique, find in literature [19–26], is useful for establishing the real behavior and the complete crack pattern along the entire beam. The technical literature is rich of case studies where the FE technique is used to study the behavior of the entire structure or individual members [27–35]. The herein considered beam was modelled using a structured mesh with tetrahedral type elements. The characteristic element length equal to 10 mm was evaluated through the relationship provided by Midas [10]. The internal reinforcement was modelled through a linear truss, while the external reinforcement was modelled by a shell element with linear interpolation functions. Finally, a perfect bond was assumed both between the beam and external reinforcement and the concrete and internal reinforcement. In Figure 16, a 3D FE mesh was reported. In particular, the adhesion between the concrete and the reinforcing rebars was defined through the internal function called embedded regions. The embedded technique is used to specify that the internal reinforcement is embedded in host elements (beam).

5.2. Materials Model. The concrete smeared cracking function was used to model the two principal concrete failure mechanisms such as the tensile cracking and the compressive crushing. This model is designed for the applications in which the concrete is subjected to essentially monotonic loading and it uses oriented damaged elasticity concepts (smeared cracking) to describe the reversible part of the material's response after cracking failure. The constitutive compressive law of concrete was modelled by non-linear relationship proposed by *Thoronfeldt et al.* [36], where f_c and ε_c are the compressive strength and relative strain. The descending branch is possible to define it through a

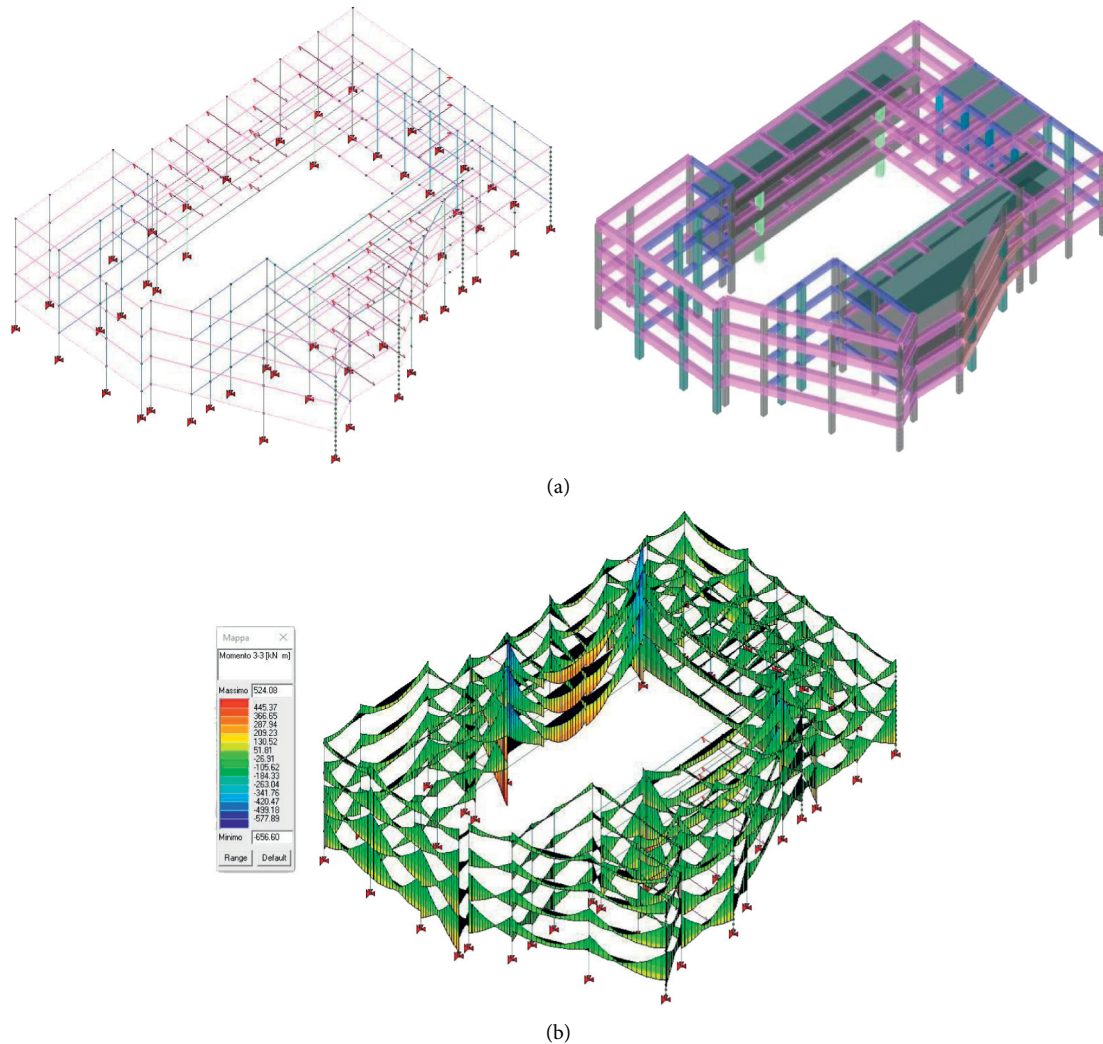


FIGURE 15: RC-structure global model in seismic load combination without any strengthening: (a) beam and 3D model and (b) results.

coefficient k , as reported in [36]. The constitutive tensile law was modelled by the relationship proposed by Hordijk, [37]. The model's parameters used are the tensile strength $f_t = 1.59$ MPa, the fracture energy $G_f = 0.08$ N/mm. In Figure 17 the materials constitutive laws were reported.

The steel constitutive law used to model the longitudinal steel and the stirrups was considered by means of elastic-plastic hardening trend, both in tension and compression. In the linear elastic range, the behavior has been defined by the density ($\rho = 7.85$ g/cm³), Young's modulus ($E_s = 210$ GPa) and Poisson's ratio ($\nu = 0.3$). Instead, the plastic-hardening branch has been defined through the yield strength (equal to 356 MPa), the ultimate strength (equal to 856 MPa) and the deformation values corresponding to the two strengths considered. The investigated beam was reinforced with two reinforcement systems CFRP and BP. Both systems were modelled as a homogenous material by a shell element with the linear interpolation functions. Therefore, the constitutive tensile laws were linear elastic until failure for the CFRP system, while linear elastic until the yield stress and then perfect plastic for BP-system. The input data parameters are modulus (E_f), thickness (t), yield stress (f_y) and the ultimate strain (ϵ_u) and

they were summarized in Table 2. In addition, the CFRP system has been applied on a part of the beam width equal to 15 cm in the tension zone, while the BP system was applied on the whole beam width. In particular, the external reinforcement was applied both in the flexural compression and tensile side of the existing beam. The two steel plates, in the numerical model was not connected. The selected reinforcement systems are BP and CFRP. Both systems have the drawback of employing skilled workers. The CFRP system presents a thickness of just over 1 mm and its installation is easy and fast. The main advantage consists of the not sensitivity to the corrosion differently to the steel. The disadvantage of CFRP is that it has linear elastic until the rupture behavior which means poor ductility. Furthermore, it is sensible to high temperature. The BP system has greater resistance to high temperatures and has non-linear behavior. The disadvantages are the thicknesses and installation time of the reinforcement.

5.3. Numerical Results. The analysis was conducted under enforcing displacements $-\lambda u$ in y -directions and the non-linear equations were solved by the well-known Newton's

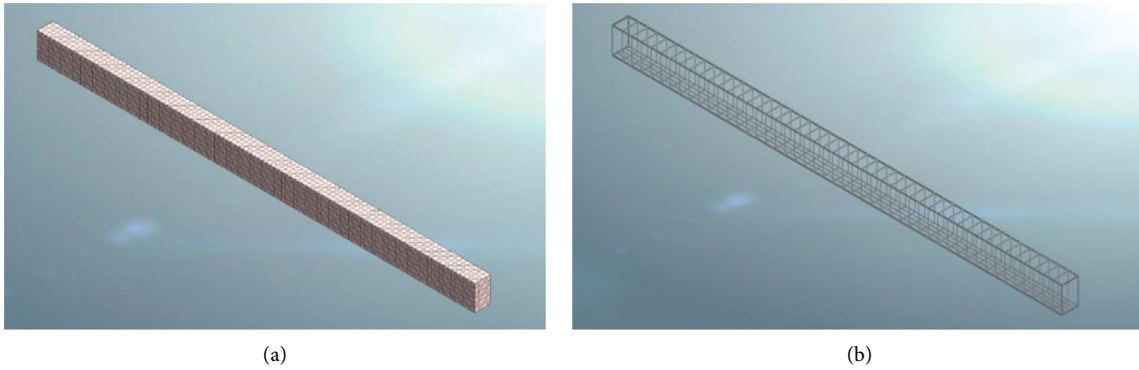


FIGURE 16: Geometrical modelling and FE resolution: (a) concrete and (b) internal reinforcement.

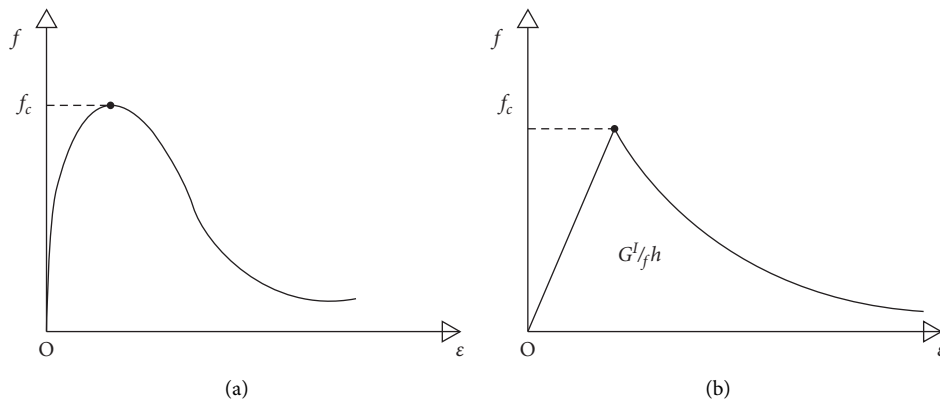


FIGURE 17: Material constitutive laws: (a) compression and (b) tension.

TABLE 2: Parameters for the EBs.

External reinforcement	E [GPa]	t [mm]	f_y [MPa]	ϵ_u [%]
CFRP plate	170	1.4	—	1
BP	210	5	275	2

modified method. The aim is to recompute the global stiffness of the structure at each load step. Consequently, the method is costly from the computational point of view in the n -step while faster at global level. Moreover, the Newton's modified method for determining a root of a nonlinear equation $f(x) = 0$ has long been favored for its simplicity and fast rate of convergence. *Newton's modified method* iteratively produces a sequence of approximation that converge quadratically to a simple root. While a few rules with higher order convergence have long been known, these have the disadvantage of requiring higher order derivatives.

Figure 18 shows the numerical curves in terms of applied total load versus mid-span section deflection. In addition, the dashed lines indicate the load value to which the existing beam is currently subjected, which is equal to 224 kN (green line), and the load to which it will be subjected after the change of serviceability of the building and, at the same time, the extension of the floor (see Section "Architectural project") or rather equal to 589 kN (orange line).

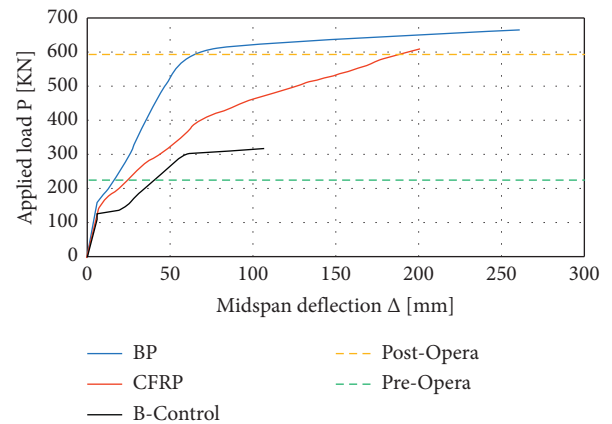


FIGURE 18: Load vs deflection law: comparison of the results.

First of all, from Figure 18 it can be seen that the actual capacity of the beam (black line) is largely major of the potential original design load (i.e. 224 kN), while it is dramatically minor when compared with the demand reached after the multiplex conversion (i.e. 589 kN). The red and blue numerical curves represent the reinforcement scenario of the existing beam with CFRP and BP, respectively. Both the reinforcement systems resulted, in terms of applied load, to

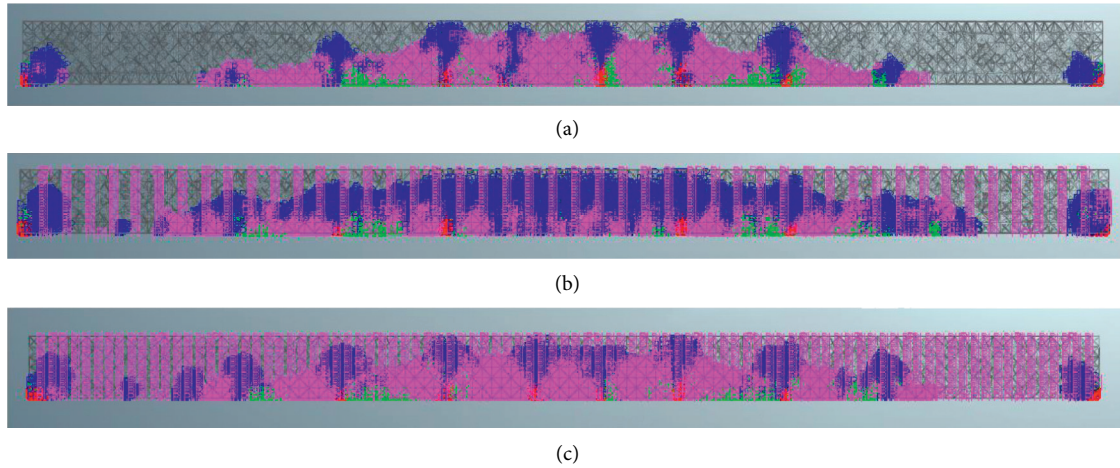


FIGURE 19: Crack pattern when the first crack opening: (a) B-Control, (b) CFRP and (c) BP.

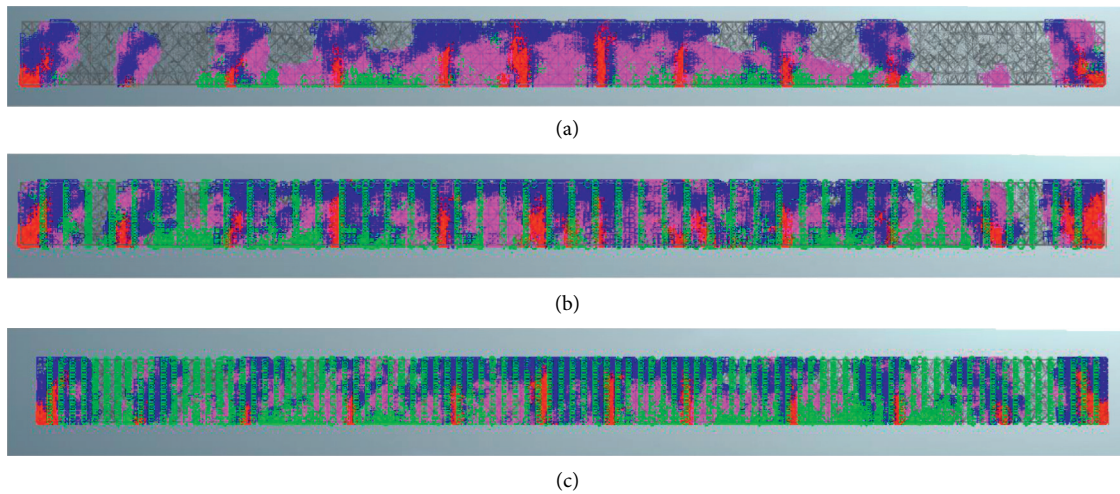


FIGURE 20: Crack pattern at ultimate limit state: (a) B-Control, (b) CFRP and (c) BP.

have greater load bearing capacity if in contrast with the required limit load, again 589 kN. On the other hand, the bending capacity expressed in terms of deflection is a further crucial aspect. In fact, the CFRP solution exhibited a larger deformation (i.e. 200 mm) at the mid-span level when compared with the BP alternative before the yielding (i.e. 61.44 mm). nonetheless, in both cases the deflection is relatively low if normalized per the span of the beam providing an optimal solution in order to take into consideration of the limitations in the Italian standard [8]. Furthermore, the stiffness in the elastic range is considerably higher for BP instead of CFRP. Moreover, according to Figure 18, the reinforcement called BP satisfied the mechanical performance required of the structure post-opera. The adopted solution affords the reinforced element an increase in terms of initial stiffness if compared with the other solution. Moreover, the BP reinforcement system in terms of midspan deflection after the yield point shows an applied load response curve with a plateau very emphasized. This solution presents a disadvantage in terms of added thickness (see Table 2) in comparison with the CFRP reinforcement

technique. The reliability of the proposed FE model is testified also by the evaluation of the failure modes. At this scope the comparison of the crack patterns at the first crack opening step and at the ultimate limit state condition are illustrated in Figures 19 and 20, respectively. As expected, the first crack (in red) opens at mid-span level and the next one tends to have constant distance each other in between two consecutive stirrups. By observing the ultimate state, the development of the cracks (again in red) is more evident with a pseudo vertical trend. It is also noticeable that the number of cracks is almost the same in all the configurations.

6. Conclusions

The case study herein presented report on the common problem of overloading and seismic deficiency due to the chance of serviceability of a cultural Heritage: the *Super-cinema* in Trani (Italy). The study dealt with a scientific key, or rather the aid of advanced tools for surveying, analyzing and verifying the structures. In order to be able to carry out the three new projecting rooms in correspondence with the

current galleries on the second floor, it was decided to design the attic between the second and third deck. In these new rooms, the overloading was fully located on an approximately 14 m long span RC-beam.

Before proceeding with the study and reinforcement of the beam, since the building is composed of two adjacent structures of different construction system, the structural model was first developed, starting from the architectural model, thanks to the help of the Autodesk Revit BIM software that allowed to better understand the position of the structural elements. Subsequently, a seismic structural joint was designed in order to “separate” the two structures.

Secondly, modelling the beam within the Midas FEA NX finite element software was performed aiming to simulate the bending strengthening by means of both CFRP-plate (CFRP) and *Beton Plaquè* (BP), in a non-linear static analysis. The results demonstrated the effectiveness of the two proposed solutions in terms of both loads bearing capacity (almost doubled) and mid-span deflection (ranging between two and three times more). It was found the steel strengthening is the most suitable for the intervention since it is significantly stiffer.

Data Availability

all data are available on request.

Conflicts of Interest

The authors declare to have not conflicts of interest.

Acknowledgments

The authors would like to sincerely thank the owners of the building for having guaranteed access and the possibility to investigate and study the structure.

References

- [1] ICOMOS/Iscarsah Committee, “Recommendations for the Analysis, Conservation and Structural Restoration of Architectural Heritage,” 2005, <http://www.icomos.org>.
- [2] A. Formisano, A. Massimilla, G. Di Lorenzo, and R. Landolfo, “Seismic retrofit of gravity load designed RC buildings using external steel concentric bracing systems,” *Engineering Failure Analysis*, vol. 111, Article ID 104485, 2020.
- [3] M. D’Amato, A. Gigliotti, and R. Laguardia, “Seismic isolation for protecting historical buildings: a case study,” *Frontiers in Built Environment*, vol. 5, no. 87, 2019.
- [4] A. Miano, G. Chiumiento, A. Formisano, and A. Prota, “Influence of different knowledge levels on the seismic retrofit cost assessment of a RC school building,” in *AIP Conference Proceedings*, vol. 2293, no. 1, AIP Publishing LLC, Article ID 380014, 2020.
- [5] M. Laterza, M. D’Amato, and R. Gigliotti, “Modeling of gravity-designed RC sub-assemblages subjected to lateral loads,” *Engineering Structures*, vol. 130, pp. 242–260, 2017.
- [6] R. J. Williams, P. Gardoni, and J. M. Bracci, “Decision analysis for seismic retrofit of structures,” *Structural Safety*, vol. 31, no. 2, pp. 188–196, 2009.
- [7] N. Berlucchi and S. Cicognetti, “Restauro e adeguamento normativo di un teatro all’italiana: il Sociale di Camogli,” *Restauro e adeguamento normativo di un teatro all’italiana: il Sociale di Camogli*, vol. 9, pp. 27–42, 2020.
- [8] Ntc 2018, *Ntc 2018 – Nuove Norme Sismiche Per Il Calcolo Strutturale*, 2018.
- [9] Circolare, *Istruzioni per l’applicazione dell’«Aggiornamento delle “Norme tecniche per le costruzioni”» di cui al decreto ministeriale 17 gennaio 2018*, 2019.
- [10] F. E. A. Midas, *Advanced Nonlinear and Detail Program, Analysis and Algorithm*, 1989.
- [11] L. Khemlani, *Autodesk Revit: Implementation in Practice*, 2004.
- [12] PROfessional Structural Analysis Program, “PROfessional Structural Analysis Program,” 2020, <https://www.2si.it/it/>.
- [13] A. Balsamo, F. Nardone, I. Iovinella, F. Ceroni, and M. Pecce, “Flexural strengthening of concrete beams with EB-FRP, SRP and SRCM: experimental investigation,” *Composites Part B: Engineering*, vol. 46, pp. 91–101, 2013.
- [14] O. Rosenboom and S. Rizkalla, “Modeling of IC debonding of FRP-strengthened concrete flexural members,” *Journal of Composites for Construction*, vol. 12, no. 2, pp. 168–179, 2008.
- [15] M. A. Aiello, M. Leone, and L. Ombres, “Structural analysis of reinforced concrete beams strengthened with externally bonded FRP (fiber reinforced polymers) sheets,” in *Proceedings of the Third International Conference on “composites in Constructions”*, pp. 11–18, Lyon, France, July, 2005.
- [16] L. Ombres, “Flexural analysis of reinforced concrete beams strengthened with a cement based high strength composite material,” *Composite Structures*, vol. 94, no. 1, pp. 143–155, 2011.
- [17] A. F. Ashour, S. A. El-Refai, and S. W. Garrity, “Flexural strengthening of RC continuous beams using CFRP laminates,” *Cement and Concrete Composites*, vol. 26, no. 7, pp. 765–775, 2004.
- [18] M. Y. Alabdulhady, L. H. Sneed, and C. Carloni, “Torsional behavior of RC beams strengthened with PBO-FRCM composite-an experimental study,” *Engineering Structures*, vol. 136, pp. 393–405, 2017.
- [19] L. Ombres and S. Verre, “Experimental and numerical investigation on the steel reinforced grout (srg) composite-to-concrete bond,” *Journal of Composites Science*, vol. 4, no. 4, p. 182, 2020.
- [20] F. Bencardino, M. Nisticò, and S. Verre, “Experimental investigation and numerical analysis of bond behavior in SRG-strengthened masonry prisms using UHTSS and stainless-steel fibers,” *Fibers*, vol. 8, no. 2, p. 8, 2020.
- [21] L. Ombres and S. Verre, “Numerical modeling approaches of FRCMs/SRG confined masonry columns,” *Frontiers in Built Environment*, vol. 5, p. 5, 2019.
- [22] L. Ombres and S. Verre, “Flexural strengthening of RC beams with steel-reinforced grout: experimental and numerical investigation,” *Journal of Composites for Construction*, vol. 23, no. 5, 2019.
- [23] S. Verre, “Three-dimensional numerical modeling of RC beam strengthened in shear with steel reinforced grout (SRG),” in *Proceedings of the 1st Fib Italy YMG Symposium on Concrete and Concrete Structures*, pp. 64–71, Krakow, Poland, May, 2019.
- [24] L. Ombres and S. Verre, “Numerical analysis of the structural response of masonry columns confined with SRG (steel reinforced grout),” *MetroArchaeo*, vol. 2017, pp. 718–722, 2019.
- [25] S. Verre, A. Cascardi, M. A. Aiello, and L. Ombres, “Numerical Modelling of FRCMs Confined Masonry Column,” *Key Engineering Materials*, vol. 817, 2019.

- [26] L. Ombres and S. Verre, "Masonry columns strengthened with steel fabric reinforced cementitious matrix (S-FRCM) jackets: experimental and numerical analysis," *Measurement*, vol. 127, pp. 238–245, 2018.
- [27] H. Pirsaeheb, P. Wang, M. Javad Moradi, and G. Milani, "A Multi-Pier-Macro MPM method for the progressive failure analysis of perforated masonry walls in-plane loaded," *Engineering Failure Analysis*, vol. 127, Article ID 105528, 2021.
- [28] A. Ferrante, E. Giordano, F. Clementi, G. Milani, and A. Formisano, "FE vs. DE modeling for the nonlinear dynamics of a historic church in Central Italy," *Geosciences*, vol. 11, no. 5, p. 189, 2021.
- [29] F. Clementi, "Failure analysis of apennine masonry churches severely damaged during the 2016 central Italy seismic sequence," *Buildings*, vol. 11, no. 2, p. 58, 2021.
- [30] A. Ferrante, M. Schiavoni, F. Bianconi, G. Milani, and F. Clementi, "Influence of stereotomy on discrete approaches applied to an ancient church in Muccia, Italy," *Journal of Engineering Mechanics*, vol. 147, no. 11, Article ID 04021103, 2021.
- [31] M. Valente, "Seismic vulnerability assessment and earthquake response of slender historical masonry bell towers in South-East Lombardia," *Engineering Failure Analysis*, vol. 129, Article ID 105656, 2021.
- [32] V. Sarhosis, D. Dais, E. Smyrou, Í. E. Bal, and A. Drougkas, "Quantification of damage evolution in masonry walls subjected to induced seismicity," *Engineering Structures*, vol. 243, Article ID 112529, 2021.
- [33] A. Ferrante, D. Loverdos, F. Clementi et al., "Discontinuous approaches for nonlinear dynamic analyses of an ancient masonry tower," *Engineering Structures*, vol. 230, Article ID 111626, 2021.
- [34] A. Kita, N. Cavalagli, M. G. Masciotta, P. B. Lourenço, and F. Ubertini, "Rapid post-earthquake damage localization and quantification in masonry structures through multidimensional non-linear seismic IDA," *Engineering Structures*, vol. 219, Article ID 110841, 2020.
- [35] N. Grillanda, L. Cantini, L. Barazzetti, G. Milani, and S. Della Torre, "Advanced modeling of a historical masonry umbrella vault: settlement analysis and crack tracking via adaptive NURBS kinematic analysis," *Journal of Engineering Mechanics*, vol. 147, no. 11, Article ID 04021095, 2021.
- [36] E. Thorenfeldt, A. Tomaszewicz, and J. J. Jensen, "Mechanical properties of highstrength concrete and applications in design," in *Proceedings of the Symp. Utilization of High-Strength Concrete (Stavanger, Norway)*, Trondheim, Norway, January, 1987.
- [37] D. A. Hordijk, "Local Approach to Fatigue of Concrete," PhD Thesis, Delft University of Technology, Delft, Netherlands, 1991.

Research Article

An Alternative Method for Long-Term Monitoring of Thai Historic Pagodas Based on Terrestrial Laser Scanning Data: A Case Study of Wat Krachee in Ayutthaya

Peerasit Mahasuwanchai , Chainarong Athisakul , Phasu Sairuamyat ,
Weerachart Tangchirapat , Sutat Leelataviwat , and Somchai Chucheepsakul 

Department of Civil Engineering, Faculty of Engineering, King Mongkut's University of Technology Thonburi, Bangkok 10140, Thailand

Correspondence should be addressed to Chainarong Athisakul; chainarong.ath@kmutt.ac.th

Received 14 February 2021; Revised 6 May 2021; Accepted 18 May 2021; Published 3 June 2021

Academic Editor: Alessio Cascardi

Copyright © 2021 Peerasit Mahasuwanchai et al. This is an open access article distributed under the Creative Commons Attribution License, which permits unrestricted use, distribution, and reproduction in any medium, provided the original work is properly cited.

This article presents an alternative method for the long-term monitoring of heritage pagodas in Thailand. In this method, terrestrial laser scanning (TLS) is used in combination with permanent survey markers. The Wat (temple) Krachee in the Ayutthaya Province of Thailand was chosen as a case study. This temple has several fantastic elements, including an inverted bell-shaped pagoda, two intertwined trees growing within it, and a chamber inside the pagoda. The preservation team working on the pagoda encountered a challenging problem and faced a decision to trim or not to trim the tree since it has a long-term effect on the pagoda's structural stability. A high-accuracy terrestrial laser scanner was used to collect three-dimensional point cloud data. Permanent survey markers were constructed in 2018 to be used in long-term monitoring. The 3D surveying of the temple and the monitoring of the pagoda were carried out in five sessions during a period ending in 2020. A point cloud data analysis was performed to obtain the current dimensions, a displacement analysis, and the pagoda leaning angle. The results revealed that the terrestrial laser scanner is a high-performance piece of equipment offering efficient evaluation and long-term monitoring. However, in this study, permanent survey markers were also required as a benchmark for constraining each monitoring session. The 3D point cloud models could be matched with the assumption model elements to evaluate the damaged shape and to determine the original form. The significant elements of an inverted bell-shaped pagoda were investigated. Trimming the tree was found to cause the leaning angle of the pagoda to decrease. An equation was developed for predicting the leaning angle of the Wat Krachee pagoda for preservation and restoration planning in the future. From the results of this study, it is recommended that periodic monitoring should continue in order to preserve Thai pagodas in their original forms.

1. Introduction

The cultural heritage sites of Thailand are considered an invaluable resource for the nation. Over time, the heritage sites have been inevitably affected by natural disasters and damage by humans. For this reason, assessment and monitoring of the historical structures are essential to prevent future damage. In traditional surveying methods, the surveyors or engineers must collect information by hand, which is a time-consuming process with low precision. It also requires a surveyor's specific expertise to investigate the

anomalies of this historic structure. Today, the most effective instrument for surveying and monitoring is the terrestrial laser scanner (TLS). It has been used for the massive collection of three-dimensional data for structures in their current condition. An advantage of this technology is the relatively short time and its high accuracy in digitizing real-world objects [1]. This information can be processed and developed for the assessment and risk management of historic buildings [2–4]. Previous research has reported the application of the terrestrial laser scanner in engineering, architecture, and various other fields, such as prototyping

[5], geomorphology [6], and characterization of slope instability [7]. In terms of the conservation of historical buildings, surveying based on TLS technology has various applications, such as roof deformation analysis [8], deformation monitoring of structures [9–11], geometric anomalies analysis [12, 13], and leaning angle analysis [14].

Many researchers have utilized terrestrial laser scanners for data collection to assess structural stability and conduct seismic analyses of historical buildings. For example, Jiao et al. [15] carried out a building damage analysis from earthquake loading by acquiring data from 3D laser scanners. The results revealed that the three-dimensional information from TLS provides enough data for the analysis of building damage. Fortunato et al. [16] studied the seismic vulnerability of San Giovanni in Tumba (Italy) by surveying with a 3D laser scanner to develop a shape model for structural analysis under seismic loading. Quagliarini et al. [17] reported that the risk assessment of historical buildings in their current condition using the 3D laser scanner for data collection provided a fast, low-cost, and safe methodology. Moreover, Micelli and Cascardi [18] presented a drone-based survey of a historic bell tower in Italy for the generation of geometry for structural assessment and seismic analysis. The results showed that drone-based surveys can reduce the time-cost. However, for data collection in a lightless area or small chamber, it may be essential to use TLS technology.

Point cloud data from TLS can accurately provide the geometrical shape of a structure for its current surface condition. In the literature, there are related reports on the point cloud analysis of historic structures. For example, Bertacchini et al. [19] described the monitoring of three historical towers in Italy. The data obtained from TLS was used to determine that the maximum displacements and tilt angles of the three towers were in the range of 0.71–2.38 meters and 1.04–1.51 degrees, respectively. Jo and Lee [20] presented the displacement analysis procedure to evaluate the structural stability of a stone pagoda in Korea. The results showed that the stone pagoda had moved in the northeast direction. Moreover, the authors suggested that continuous monitoring of the pagoda's deformation should be required to preserve its original form. Fregonese et al. [21] presented the use of TLS technology for surveying and monitoring an ancient building. The results demonstrated that such technology could accurately detect the displacement of the ancient structural movements. Teza and Pesci [22] presented the results of a survey of an old bell tower in Italy. The point cloud data analysis was able to evaluate the wall inclination of the bell tower.

In Thailand, TLS technology is relatively new for engineering applications, especially for the assessment and structural health monitoring of building structures. Leelataviwat et al. [23] have pioneered the preservation of many important historical sites in Thailand, and they recommended that continuous assessment and long-term monitoring are the best ways to preserve cultural heritage. One of the most well-known cultural heritage sites in Thailand is Ayutthaya Historical Park, which has been declared a World Heritage Site by UNESCO. In this historical park, there are

many important temples that need to be preserved. One of these is the Wat Krachee. This temple is dominated by two intertwined trees growing and entrancing inside the pagoda chamber. Over time, the Wat Krachee has been damaged by deteriorating materials, and the tree growth may have affected the pagoda's structural stability. Accordingly, in 2018, the Wat Krachee Conservation Project was started with the cooperation of the Fine Arts Department of the Ministry of Culture and UNESCO Bangkok of Thailand [24, 25]. However, the project faced the challenge of how to preserve the pagoda with two intertwined trees growing inside it and becoming part of the pagoda's structure. For this reason, long-term monitoring of the pagoda was required to protect it against damage.

The primary problem for the long-term monitoring of historic buildings using terrestrial laser scanners is to ensure that the point cloud data has been obtained correctly. This is not always the case due to errors in referencing the position in fieldwork and data processing. Abellán et al. [26] reported the monitoring of rockfalls based on the use of a terrestrial laser scanner for detection and spatial prediction. They noted in the results that the registration process was carried out through the visual identification of homologous points. In practice, it is challenging to choose the exact point of reference in the data processing for each monitoring session. To reduce the error in this process, a new method must be developed. Quagliarini et al. [17] identified the alignment error in each dataset as one of the main issues. Reducing this error would help to improve the technique. From the aforementioned studies on fieldwork monitoring using TLS, it was found that errors might occur in the data processing when using point-by-point referencing in manual operations.

Consequently, to reduce the errors in the long-term monitoring of Thai historic pagodas, the purpose of this study is to present an alternative method based on TLS in combination with permanent survey markers. The permanent survey markers are constructed to constrain the point cloud data for each monitoring session. This procedure is essential for the long-term monitoring of Thai pagodas to ensure that the registration corresponds to the real-world coordinates, and these should not be moved so that they can be used for future reference. The five monitoring session results for the Thai pagoda over a period of approximately two years and six months are reported. The significant elements are investigated, including the dimensions of the inverted bell-shaped pagoda, the chamber inside the pagoda, the leaning angle, and the horizontal displacement. The effect of trimming the tree is evaluated. Moreover, a prediction equation for the leaning angle of the Wat Krachee pagoda is proposed for future preservation and construction planning.

2. A Case Study of Wat Krachee in Ayutthaya

Wat Krachee is located in Ayutthaya Historical Park in Phra Nakhon Si Ayutthaya Province, as shown in Figure 1. Ayutthaya Historical Park is one of the most important archaeological sites in Thailand and was declared a UNESCO



FIGURE 1: Location of Wat Krachee, Phra Nakhon Si Ayutthaya Province, Thailand.

World Heritage Site in 1991. Figure 2 shows the differential environment of Wat Krachee at three points in time, namely, AD 1987, AD 2005, and AD 2018. It can be observed that the remaining shape of the pagoda is an inverted bell shape. Moreover, this temple has a dominant pagoda with two intertwined trees growing inside it and an entrance into the pagoda chamber, as shown in Figure 3. According to archaeological assumptions, the Wat Krachee pagoda was constructed in the middle period of Ayutthaya, in approximately AD 1550 (2093 BE), meaning that the Wat Krachee pagoda is almost 470 years old [19, 20]. At present, the material deterioration and the growth of the two intertwined trees may be affecting the stability of the Wat Krachee pagoda. In 2018, the Wat Krachee Conservation Project was started through cooperation with the Fine Arts Department of Thailand's Ministry of Culture and UNESCO Bangkok. This conservation project has brought together a multidisciplinary group of engineers, architects, materials scientists, archaeologists, arborists, craftspeople, and professionals from other related fields. Therefore, this study provides supporting information for the Wat Krachee Conservation Project.

3. Methods

A method for the long-term monitoring of rockfalls was reported in the research by Abellán et al. [26]. The registration process was carried out through the visual identification of homologous points before starting the Iterative Closest Points (ICP) procedure. However, it was difficult to choose the homologous point in each monitoring period, which may cause an alignment error in each dataset. Moreover, Quagliarini et al. [17] found that the alignment error was the main problem for assessing the position of the measuring point. They suggested that this process should be improved to increase the accuracy of the data analysis.

To alleviate the error from the target-less registration process, the present study proposes an alternative method for the long-term monitoring of pagodas in Thailand based on terrestrial laser scanning technology in combination with permanent survey markers. A flowchart of the monitoring procedure is presented in Figure 4. In the initial phase, the

planning and surveying were set up and the permanent survey markers were constructed to define the coordinate system for long-term monitoring. A terrestrial laser scanner was then used, together with spherical targets, to generate the initial coordinate system. The purpose of using the permanent survey markers was to reduce (or minimize) the error from the registration process by constraining the coordinate system of the monitoring period in three-dimensional space.

In the monitoring phase, the data acquisition of the pagoda was first carried out using TLS together with the initial coordinates and spherical targets. Then, the point cloud data were processed using FARO Scene software [27]. In this process, point cloud data were transformed into the control coordinates. Next, the preparation of the point cloud data involved cleaning and removing noise to reduce the amount of data. Then, the postprocessing results of the point cloud data were exported as an RCP file. In the last step, the data analysis procedure, the geometrical properties, the dimensions, the inclination direction, and several essential elements of the pagoda were investigated using Autodesk Revit software [2]. The monitoring phase was repeated for each monitoring session until the data analysis was complete.

3.1. Planning and Surveying. Five sessions were completed as part of the long-term monitoring of the Wat Krachee pagoda, as shown in Figure 5. The operations were carried out in February 2018, March 2018, July 2018, July 2019, and August 2020.

The surrounding area of the Wat Krachee is soft soil, which has the potential to subside due to the surveying. Therefore, it was necessary to create permanent survey markers to ensure a registration corresponding to the real-world coordinates, which should be kept in place for future reference. In this study, four permanent survey markers were constructed on-site for the sake of monitoring, as shown in Figure 6. These survey markers were made of reinforced concrete with a drill hole diameter of 0.1 meters and a depth below the surface of approximately 15–20 meters. In addition, a steel pin was attached to the survey markers to support the spherical targets.

In the procedure for the creation of coordinates for the long-term monitoring of the pagoda, the essential equipment for defining the reference coordinates are standard spherical targets with a radius of 0.0695 meters. These spherical targets were installed on the survey markers, as shown in Figure 7. Then, TLS was used for collecting the coordinates of the four spherical targets. After that, the Scene software was used to automatically detect the spherical targets, as shown in Figure 8. The obtained coordinates (X , Y , Z) were derived from the center points of the spherical targets. These coordinates, listed in Table 1, will be used as the reference coordinates for future monitoring.

3.2. Data Acquisition with Terrestrial Laser Scanning (TLS). TLS technology is a high-performance technology that is used to collect massive amounts of point cloud data for

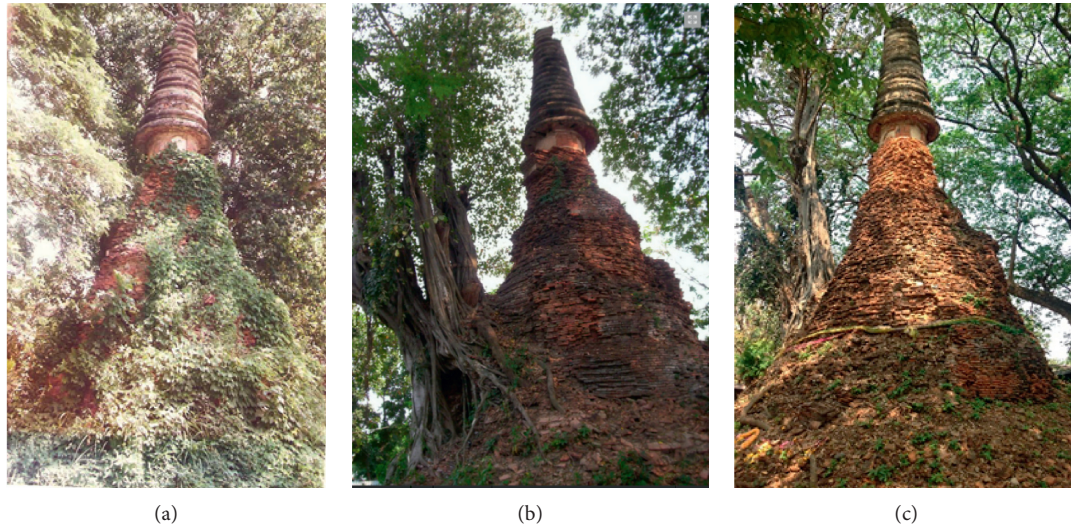


FIGURE 2: Images of Wat Krachee pagoda at three points in time. (a) AD 1987 [24]. (b) AD 2005 [25]. (c) AD 2018.

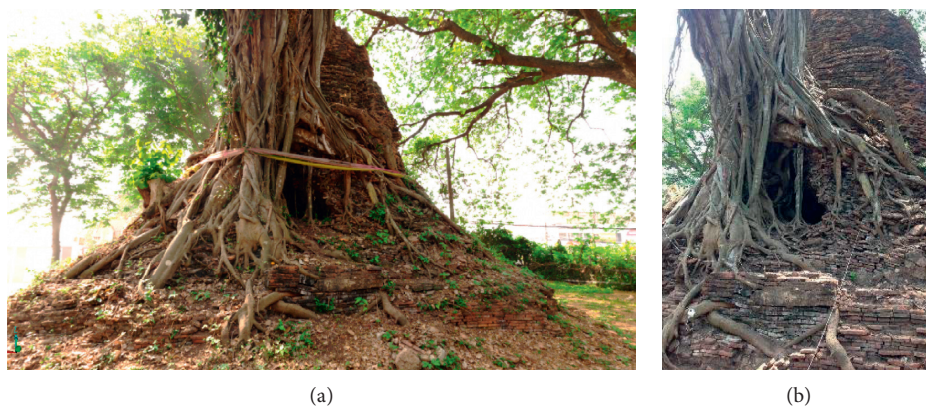


FIGURE 3: The two intertwined trees and the entrance to the chamber inside the pagoda.

objects with a complex surface [14]. In this study, TLS technology by FARO Focus3D X-330 [27] was applied for the data collection in each monitoring session. This TLS model uses phase-shift technology to measure distance, recording the vertical and horizontal angles simultaneously with the associated distance measurement. The fields of view in the vertical and horizontal directions are 300 degrees and 360 degrees, respectively. These angles and distances are transformed into Cartesian coordinates (X, Y, Z). Moreover, terrestrial laser scanners have important sensors to help with the registration process, consisting of an inclinometer (dual-axis compensator), a compass, an altimeter, and GPS. The performance specifications of the terrestrial laser scanner are shown in Table 2.

The TLS technology was applied to attain the 3D point cloud data of the Wat Krachee pagoda for each monitoring session, as displayed in Figure 9. Pueschel [28] noted that parameters such as scan resolution and scan speed had an influence on obtaining point cloud data. Therefore, for each monitoring session, these parameters were controlled using

a resolution of 28.2 million points and a speed scan of 122,000 points per second for the whole scan. Furthermore, the color photograph mode was enabled to save eighty-five images per station. With these parameters (scan resolution, scan speed, and capturing the image), it took TLS approximately eight minutes for each scanner position together with the survey markers and the standard spherical targets.

The details of the data collection process during field-work are as follows. First, the four standard sphere targets were installed on the permanent reference steel pins that had previously been constructed. TLS scanning was then carried out to collect the four spherical target positions, including the surrounding conditions of the pagoda. Next, the terrestrial laser scanner was moved to a new position, and scanning was performed while considering the overlap of the environment of the previous position to reduce alignment error in the registration process. Then, the scanner was relocated to the next position and the scanning process was repeated until the plan was completed. This process was

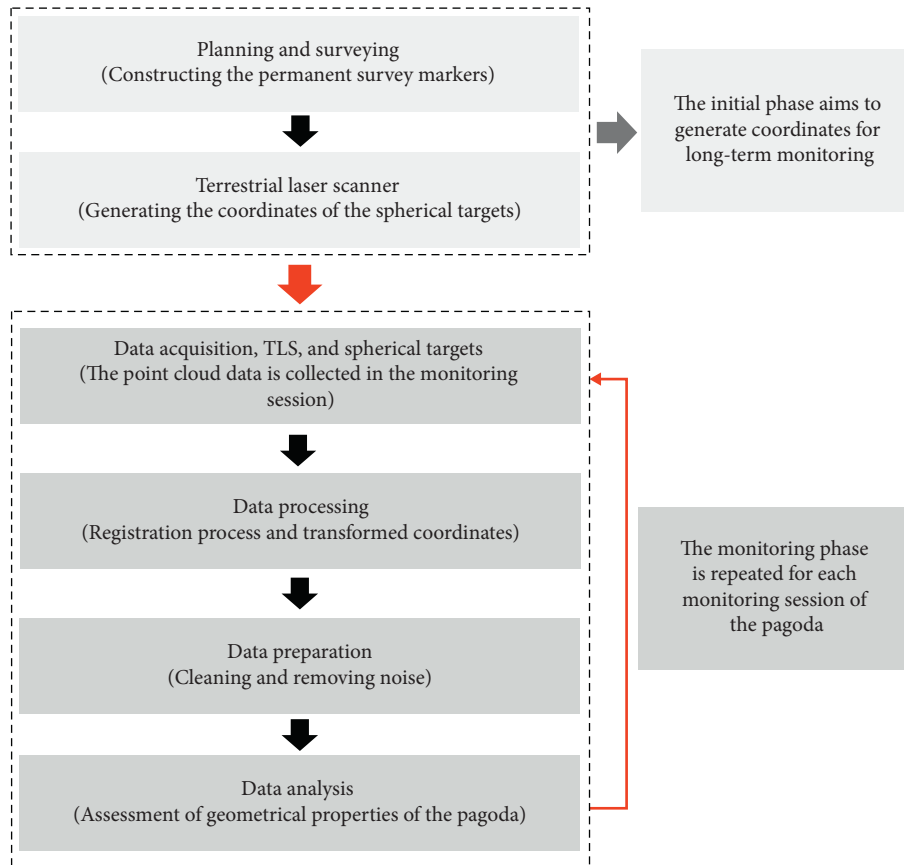


FIGURE 4: Method for long-term monitoring of Thai historic pagoda.

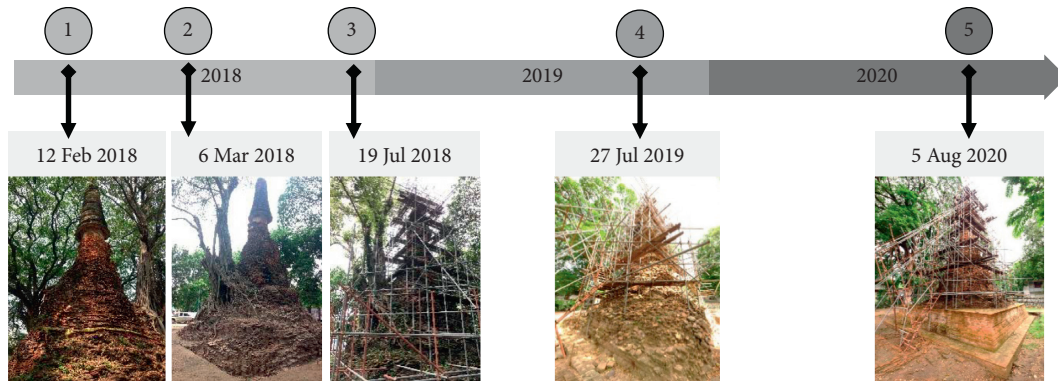


FIGURE 5: A schedule for the long-term monitoring of the Wat Krachee pagoda.

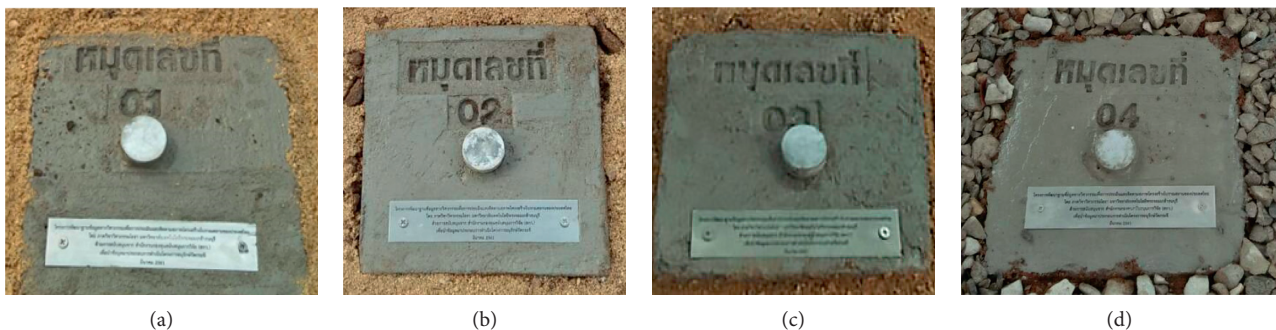


FIGURE 6: The four survey markers for the long-term monitoring of the Wat Krachee pagoda.

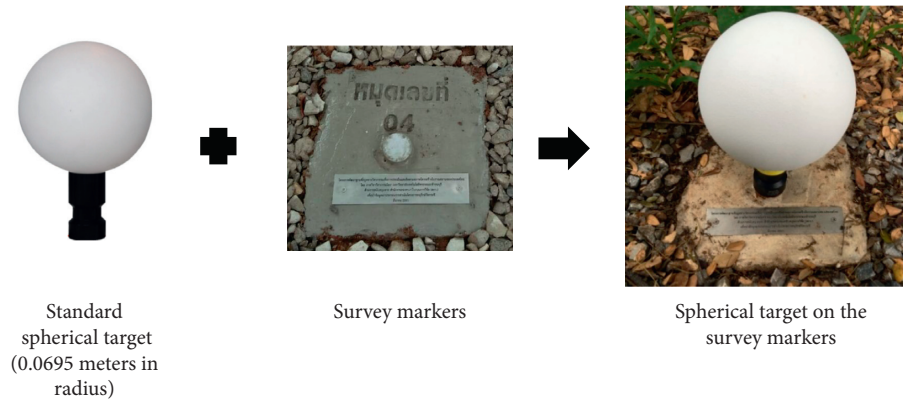


FIGURE 7: The combination of standard spherical targets and survey markers.

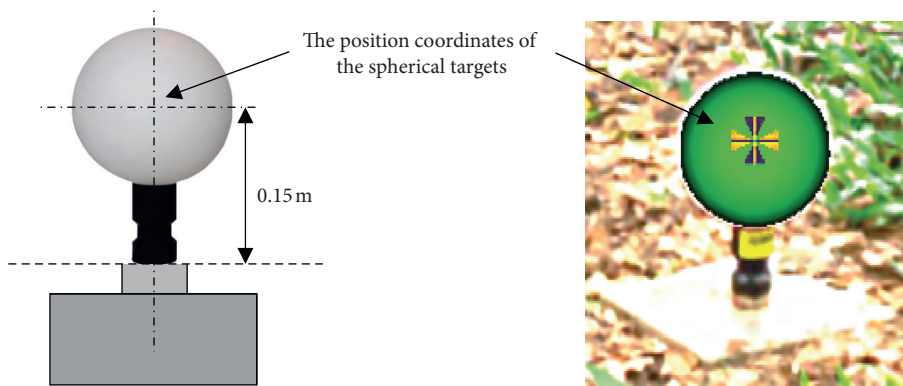


FIGURE 8: The position coordinates of the spherical targets on the survey markers.

TABLE 1: The coordinates of the spherical targets on the survey markers.

Survey markers	X (east)	Y (north)	Z (up)
SM 01	30.0000	30.0000	5.0000
SM 02	25.1550	21.9685	5.0215
SM 03	24.7339	10.0152	4.9913
SM 04	25.5419	25.0275	5.4381

TABLE 2: Performance specifications of the terrestrial laser scanner used in this study.

Effective range	0.6 m to 330 m
Field of view (vertical/horizontal)	300°/360°
Measurement speed	Up to 976,000 points per second
Laser class	Laser class1
Wavelength	1550 nm
Beam diameter at the exit	2.25 mm
Ranging error	±2 mm at 25 m
Resolution	Up to 710.7 million points per scan

applied for collecting field data during five monitoring sessions to assess the changes in the Wat Krachee pagoda structure.

On February 12, 2018, a survey of the surrounding conditions of the Wat Krachee temple was performed. It was found that this temple has some fantastic features, such as an inverted bell-shaped pagoda, two intertwined trees growing within it, and a chamber inside the pagoda. From a visual inspection, the pagoda clearly tilts; this may be due to the growth of the intertwined trees on the north side, as shown in Figure 10(a). Furthermore, a small chamber was constructed in this pagoda. The survey of this area required multiple scans of the data, and eight scan positions were collected during the first monitoring session. The second session was carried out on March 6, 2018. The environmental conditions of Wat Krachee had changed. Excavations had been made for archaeological exploration in some areas surrounding the pagoda. The two intertwined trees had been trimmed significantly in comparison to the first session, as shown in Figure 10(b). The data collection for the second monitoring session required sixteen positions to cover the archaeological excavation site. The third monitoring session took place on July 19, 2018, approximately five months after the first period. The critical problem for collecting data this time was that the surrounding pagoda was obscured by scaffolding, as shown in Figure 10(c). Moreover, the survey showed that one of the essential components of the Wat Krachee pagoda is a small chamber inside the pagoda. In this session, fourteen scans, including ten scans outside and four scans inside the pagoda, were carried out. One year and six

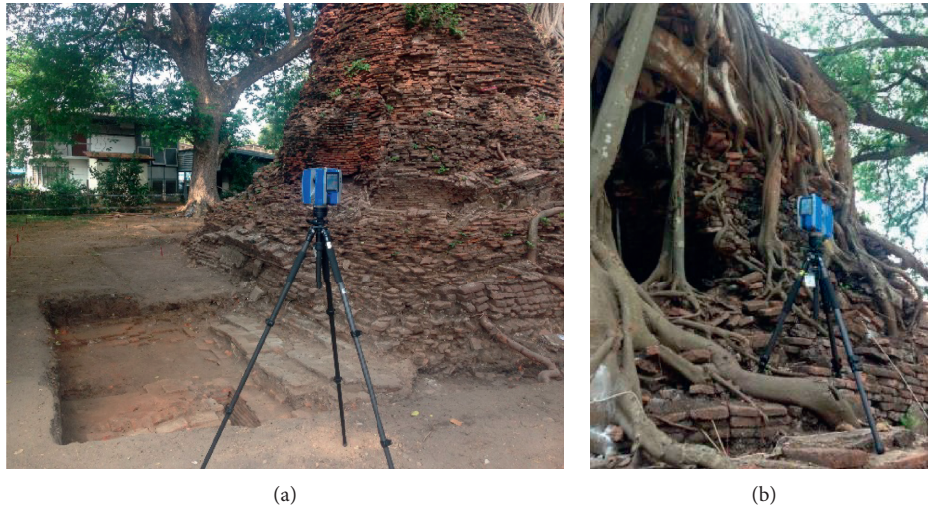


FIGURE 9: Fieldwork at the Wat Krachee temple using a terrestrial laser scanner.

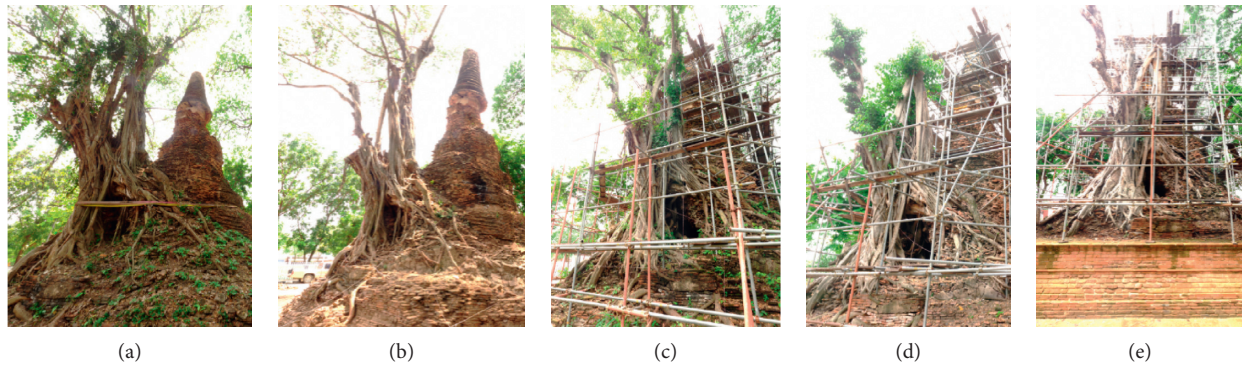


FIGURE 10: The surroundings of the Wat Krachee during the five monitoring sessions. (a) First survey. (b) Second survey. (c) Third survey. (d) Fourth survey. (e) Fifth survey.

months after the first survey, it was determined that tree trimming had slowed down the growth of the two intertwined trees, as shown in Figure 10(d). The scaffolding for preservation work was still attached to the pagoda. In this surveying session, thirteen stations of TLS were performed to gather the point cloud data. At this point, changes in the pagoda had been monitored for two years and six months from the first survey. In the fifth monitoring session, the Than Pra Thaksin section of the pagoda had been reconstructed based on archaeological assumptions, as shown in Figure 10(e). The other elements of the pagoda had not been restored. Therefore, the surveying teams carried out ten scan positions of the Wat Krachee pagoda surroundings.

3.3. Data Processing and Data Preparation. The FARO Scene software was used for data processing throughout the monitoring period. The data processing phase starts with importing the raw data into the local coordinate system from the laser scanner. Target-less registration (also referred to as cloud-to-cloud registration) was employed to combine the overlapping point clouds from each data scan. According to previous research by Wilson et al. [2], this registration

method can be applied for the data processing of historical buildings. Upon completion of this process, the 3D point cloud models are obtained. The results showed that the mean point error in each dataset from the five monitoring sessions was less than 8 mm. According to the manufacturer's [27] recommendation, the best mean error in the registration process should be less than 8 mm, for which the status is shown with a green light. An important process at this point involves constraining the dataset with the control coordinates before the data analysis, as seen in Table 1. To ensure the coordinates for each dataset were obtained through translation onto the survey control, the coordinates of the four spherical targets in each dataset were investigated. The results show that the coordinates of the spherical targets for each model were not significantly different compared with the survey control coordinates.

In the data preparation process before the point cloud analysis, it is necessary to clean the data obtained from the area surrounding the pagoda, such as scaffolding and unwanted objects. However, removing this point cloud data can only be done by filtering it out by hand, which takes a long time. The pagoda 3D models have been defined to conform to the realistic sites, as shown in Figure 11(a). The

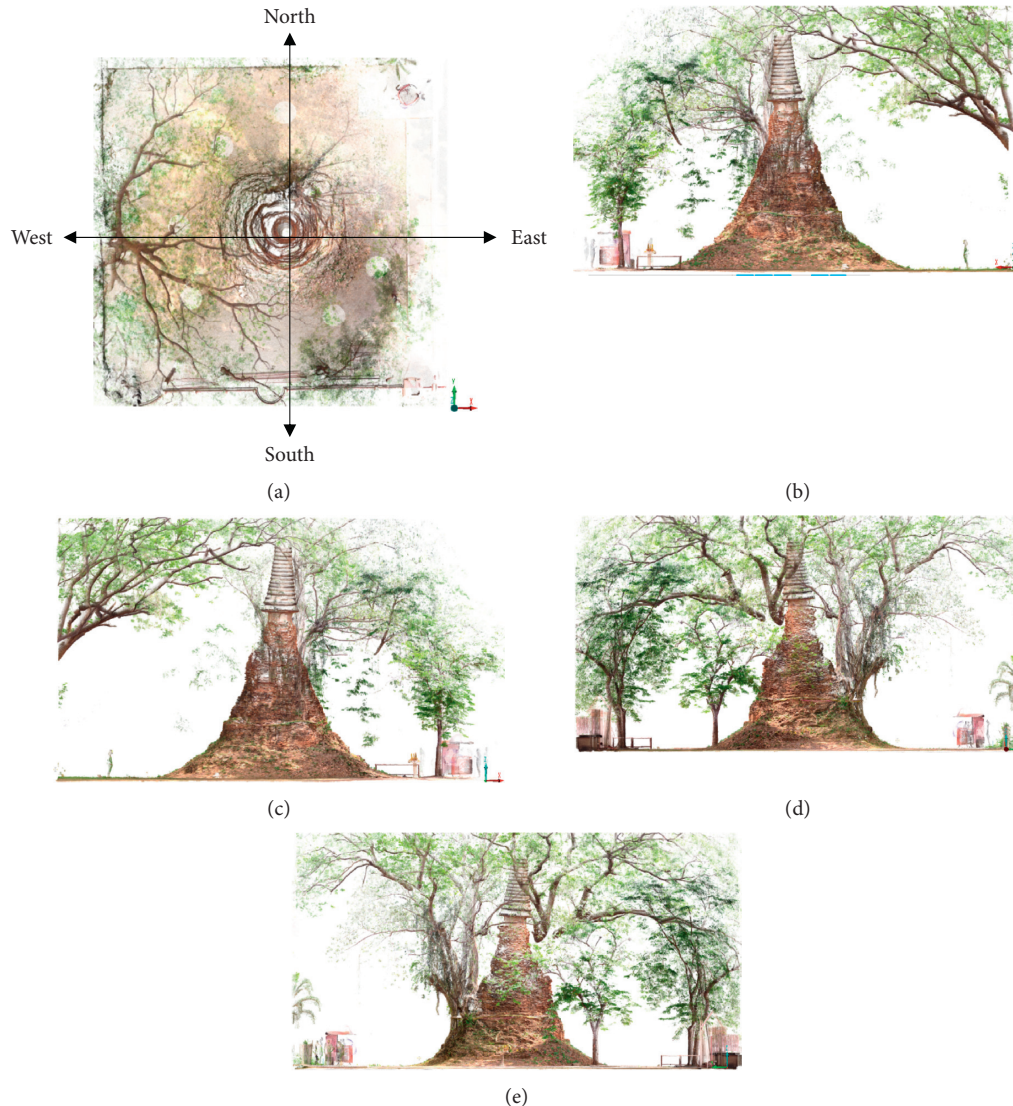


FIGURE 11: Plan view and side views of the point clouds collected in the Wat Krachee. (a) Plan view of the Wat Krachee. (b) South view. (c) North view. (d) West view. (e) East view.

side views of the four directions of the pagoda are illustrated in Figures 11(b)–11(e). The 3D point cloud models from the five monitoring sessions after passing the data processing and data preparation stages are shown in Figure 12. Finally, each model's point cloud dataset was exported as an RCP file and then transferred to Autodesk Revit software for the point cloud analyzing process.

3.4. Point Cloud Analysis. This section presents the procedure for the point cloud analysis. According to Korumaz et al. [14], the analysis of a tall building's verticality can be completed by cutting the point cloud and evaluating the obtained sections. In addition, Bertacchini et al. [19] have suggested that the trend of the vertical axis can be calculated by determining the center of each section and combining them. Therefore, this technique can be used to determine the

direction of the maximum inclination of the pagoda. The point cloud analysis of the Wat Krachee pagoda was investigated using tools in the Autodesk Revit software. The 3D point cloud models in the RCP file were inserted into the Autodesk Revit software. The point cloud dataset positioning was then selected using the origin-to-origin function so that the coordinate system was not changed. In this step, the pagoda dimensions and the change in the leaning angle for each monitoring session were assessed. Moreover, the effect of trimming the trees was investigated. A comparative analysis of the point cloud datasets was possible via CloudCompare software [7, 17]. The point cloud dataset for each monitoring session was compared with the first dataset before measuring the pagoda elements, as shown in Figure 13.

Before the assessment, the point cloud dataset required definitions for the inclination direction and the leaning angle

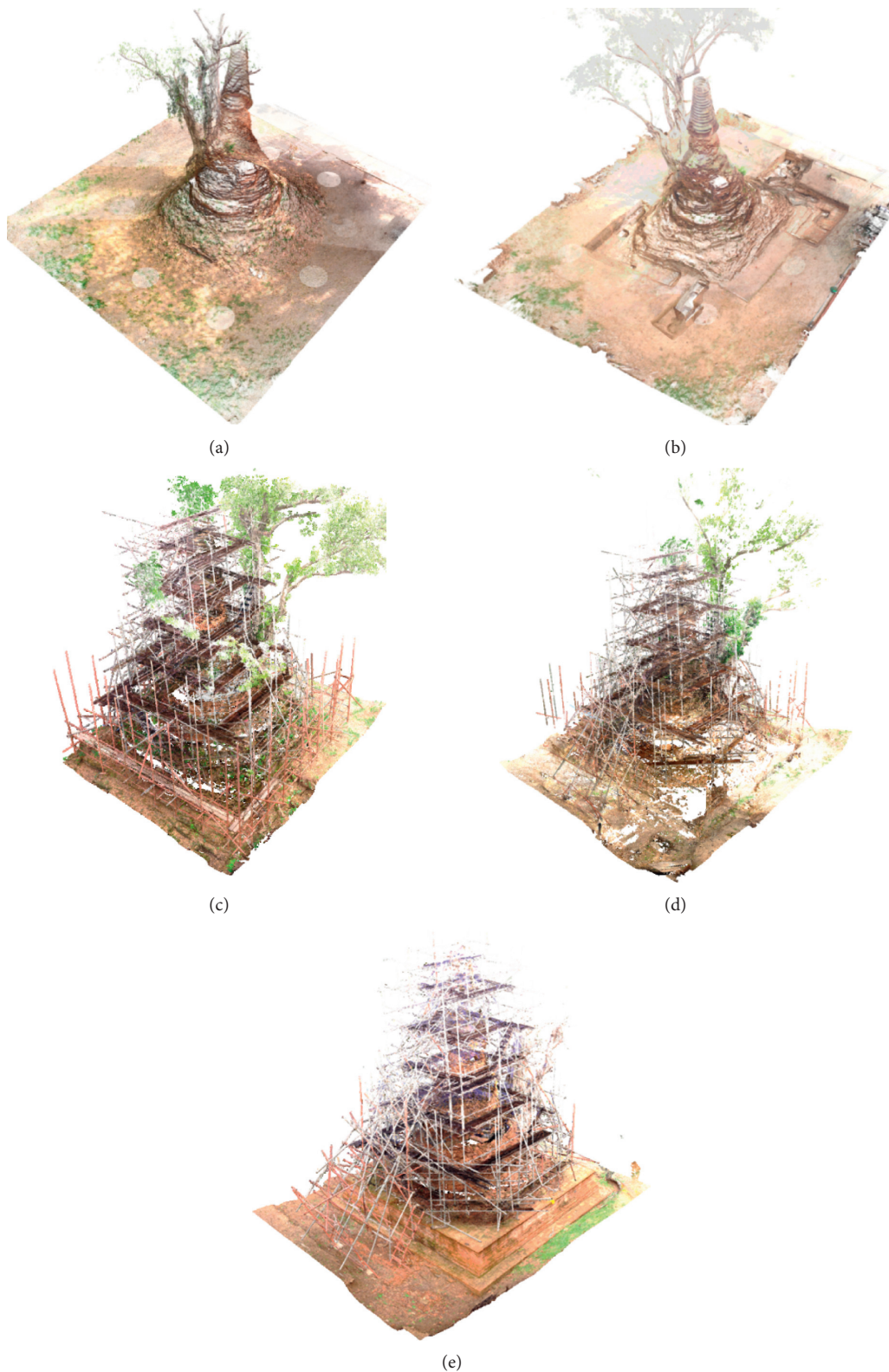


FIGURE 12: 3D point cloud models of the Wat Krachee from the five monitoring sessions. (a) February 12, 2018. (b) March 6, 2018. (c) July 19, 2018. (d) July 27, 2019. (e) August 5, 2020.

for ease of reference. Therefore, the beta (β) angle was defined from the south axis and the alpha (α) angle was determined from the east axis as the inclination direction of

the pagoda, as shown in Figure 14(a). The pagoda leaning angle is defined as the zeta (θ) angle at the inclination direction plane, as shown in Figure 14(b).

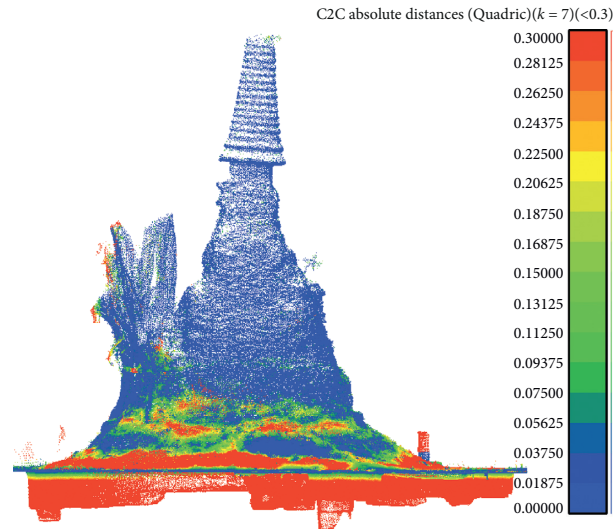


FIGURE 13: A comparative analysis between two datasets.

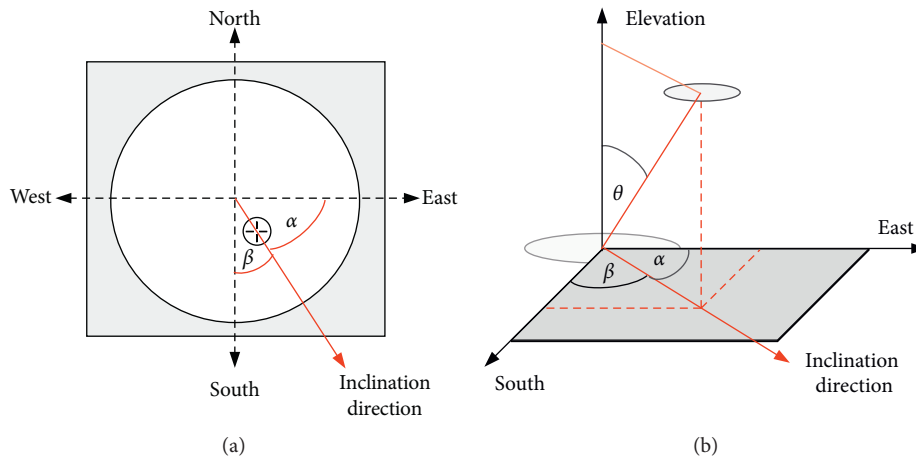


FIGURE 14: Side elevation of the pagoda with the central axis and inclination direction. (a) Plan view. (b) 3D view.

In the process of creating the geometry for the assessment of the pagoda, a level line for each component of the pagoda and a vertical axis were created, as shown in Figure 15. The Than Keang section of the pagoda was defined as a reference base for creating the vertical axis. The vertical line was generated based on the center of the Than Keang section. Afterward, a geometrical shape for each element of the pagoda was created using guidelines from the point cloud data. Then, the center of each geometric element was applied to find the pagoda inclination direction. The pagoda leaning angle could then be calculated by measuring the displacement differences between the center of each element's geometrical shape and the exact vertical line. This procedure will continue to be applied to assess the leaning angle for the long-term monitoring of the pagoda.

4. Results and Discussion

Each session for monitoring the Wat Krachee pagoda over the period of two years and six months was assessed. The

benefit of the point cloud dataset is that it could be used to analyze the dimensions of the bell-shaped pagoda element, the dimensions of the chamber inside the pagoda, the thickness of the pagoda, and the effect of tree trimming. Moreover, the pagoda's changing leaning angle was investigated to develop a prediction equation for the pagoda's future leaning angle. Details are given in the following sections.

4.1. Dimension Analysis. The 3D point cloud models of the Wat Krachee pagoda for the first monitoring session are shown in Figure 16(a). According to a report by the Fine Arts Department [29], the assumption model for this temple pagoda is an inverted bell-shaped pagoda, which consists of the Than Pra Thaksin, Than Keang, Than Pat, Malai Thao, bell shape, Banlang, Kan Chat, Falami Lotus, Plong Chanai, and Pli Yod sections, as shown in Figure 16(b). A comparison between the bell-shaped pagoda elements based on the assumption model and the 3D point cloud models can be precisely matched for each pagoda element. It was observed

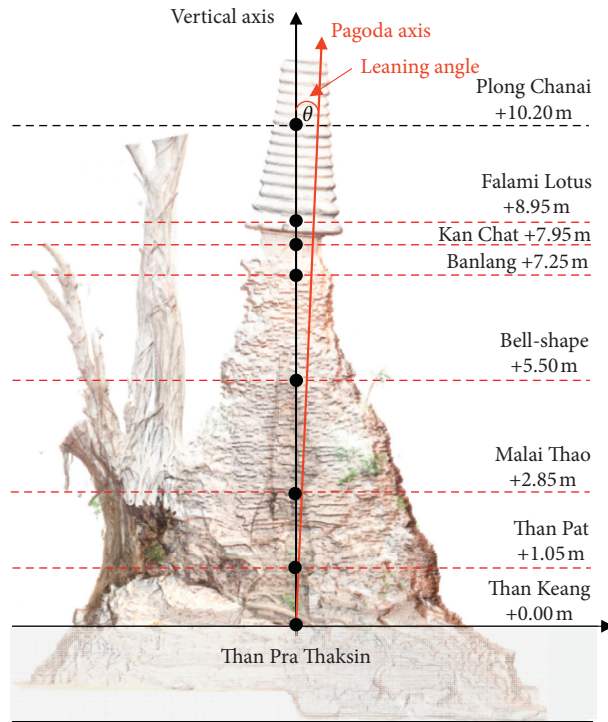


FIGURE 15: Section of the pagoda with the central axis and inclination direction.

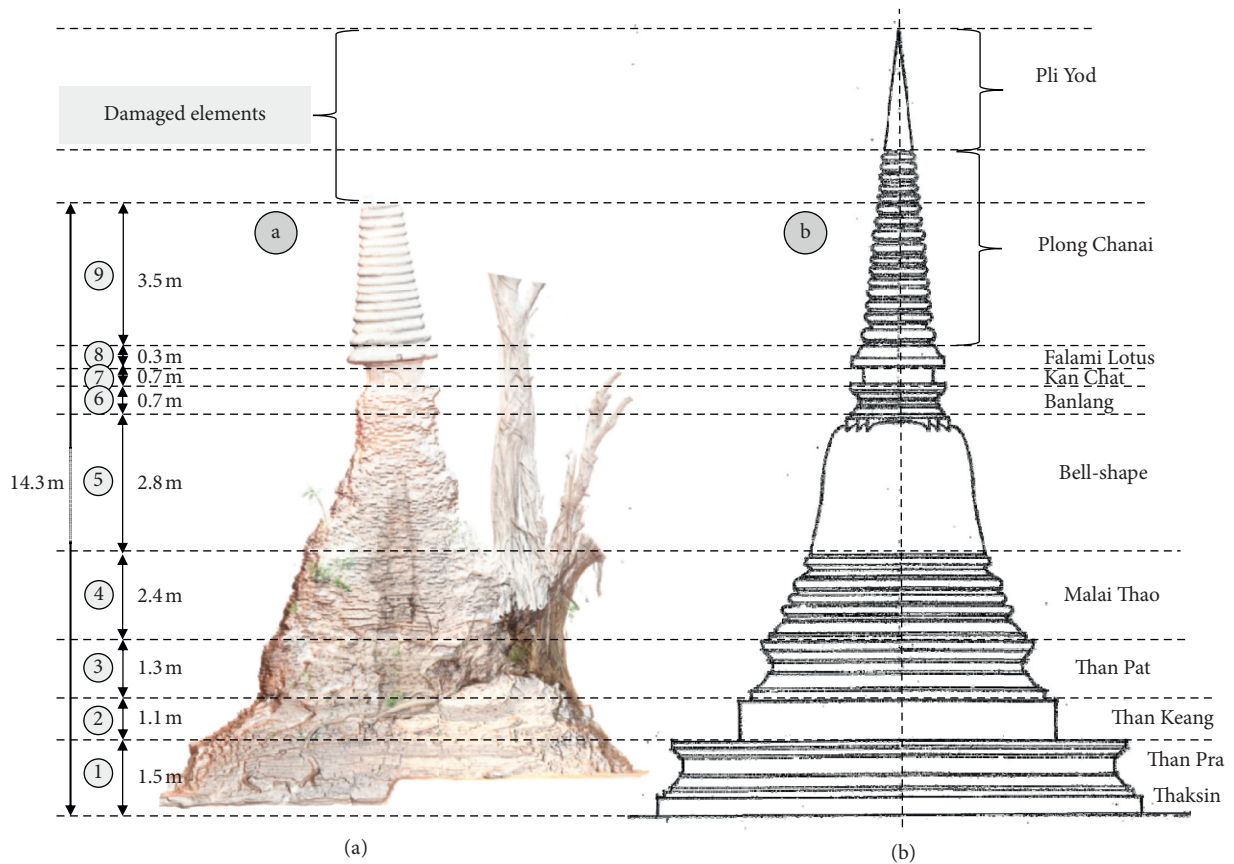


FIGURE 16: The comparison elements of the Wat Krachee pagoda. (a) 3D point cloud model. (b) Assumption model [29].

that the Pli Yod and some of the Plong Chanai sections were damaged compared to the assumption models. However, it was not clear when the damage occurred. Furthermore, the 3D point cloud models reported dimensions for each element based on the assumption model's pagoda elements.

The dimensions of each element of the realistic bell-shaped pagoda can be measured in terms of height, base dimension, and geometrical shape, as presented in Table 3. These results reveal that the point cloud data are useful for the preservation of the pagoda to its original form. The obtained dimensions of each element of the pagoda were applied to the reconstruction phase. In 2020, the Than Pra Thaksin section of the pagoda was entirely reconstructed using assumption models as a square base, as shown in Figure 17, and the other elements are in the process of being renovated.

One of the essential elements of the pagoda is the complexity inside the chamber. After postprocessing, the 3D point cloud data were utilized to investigate the complicated shape of the chamber inside the pagoda. Figure 18 shows cross-section A–A in the west direction and the measured dimensions of the pagoda. The results revealed that the entrance of the chamber is adjacent to the trees, and the height of the cavity is an average of 1.0 m. The total length of the chamber from the access point to the last chamber has a horizontal distance of 4.1 m. The smallest thickness of the pagoda in the west direction is equal to 1.0 m in the upper part of the chamber. Figure 19 displays cross-section B–B in the south direction of the pagoda, representing the detailed measurement. The findings showed that the dimensions of the chamber in the first layer are 1.2×1.2 m. There are three layers of the chamber inside the pagoda. The first layer has a height of 1.75 m, the second has a height of 1.55 m, and the third layer has a height of 2.4 m to the top layer of the chamber; thus, the total height of the chamber is 5.7 m. The smallest wall thickness is 0.5 m, located at 6.0 m above ground level. The horizontal and vertical lengths of the cavity opening were measured at 0.7 m and 1.2 m, respectively. This method collected the point cloud data inside and outside of the pagoda. Therefore, the thickness of the pagoda could be precisely assessed.

The highlight of the Wat Krachee pagoda is the two intertwined trees growing within it. The changes in the trees surrounding the pagoda at the time of each monitoring session are represented in Figure 20. In 2018, surveying and evaluation found that the height of the main tree trunk was approximately 11.45 m, and the total size of the tree was 15.5 m with respect to the ground level. During a multi-department meeting, it was agreed that the growth of the trees might affect the structural stability of the pagoda in the long term. Therefore, in 2019, arborists carried out tree trimming to slow down the growth. The height of the trimmed area was 6.8 m so that the main tree remained at the height of 8.7 m.

4.2. Monitoring Results. In this study, long-term monitoring of the Wat Krachee pagoda was carried out over a period of two years and six months. The first pagoda

TABLE 3: The dimension of each element of the bell-shaped pagoda.

No.	Elements of the bell-shaped pagoda	Height (m)	Base dimension (m)	Geometrical shape
1	Than Pra Thaksin	1.5	10.2×10.0	Square
2	Than Keang	1.1	7.5	Circle
3	Than Pat	1.3	7.3	Circle
4	Malai Thao	2.4	5.8	Circle
5	Bell shape	2.8	3.5	Circle
6	Banlang	0.7	1.85×2.0	Square
7	Kan Chat	0.7	1.35	Circle
8	Falami Lotus	0.3	2.1	Circle
9	Plong Chanai	3.5	1.8	Circle

monitoring session revealed that the pagoda had leaned toward the southeast direction, in which the beta and alpha angles were 20.85 and 69.15 degrees, respectively. This inclination direction was applied to assess the distance from the vertical axis to the center of each element of the pagoda, as shown in Figure 21. The first monitoring session calculated that the maximum leaning angle of the pagoda was equal to 3.567 degrees. The second monitoring session of the pagoda found that the leaning angle had not changed significantly because the monitoring took place shortly after the first period, as represented in Figure 22. Four months later, the inclination direction and the horizontal displacement were determined, as displayed in Figure 23. From this monitoring, it was found that the leaning angle of the pagoda had increased by 0.019 degrees. Therefore, the leaning angle of the pagoda during the third monitoring session was equal to 3.586 degrees. Moreover, it was found that the beta angle had increased in the east direction when compared to the first monitoring. One year and six months after the first session, the assessment inclination direction and the leaning angle were determined, as shown in Figure 24. The results revealed that the leaning angle of the pagoda had become 3.618 degrees or an increase of 0.051 degrees from the first measurement. The beta angle continuously increased to 21.85 degrees. The results from the fifth monitoring session of the pagoda, two years and six months after the first one, are shown in Figure 25. The maximum distance of the vertical axis of 0.652 m was obtained on the Plong Chanai section of the pagoda, and the leaning angle was 3.655 degrees.

Furthermore, the assessment of the leaning angle for each monitoring session can generate the relationship between time and the leaning angle of the Wat Krachee pagoda, as shown in Figure 26. The results show that the leaning angle might have increased significantly if the recommendation to trim the trees had been ignored. Considering the actual monitoring, the results also indicate that time influences the leaning angle of the pagoda. However, a regression analysis was applied using the least-squares fit method with a linear trend line, as presented in equation (1). The result revealed that the slope ($d\theta/dt$) and the coefficient of determination (R^2) of this equation are 0.0001 and 0.99, respectively.

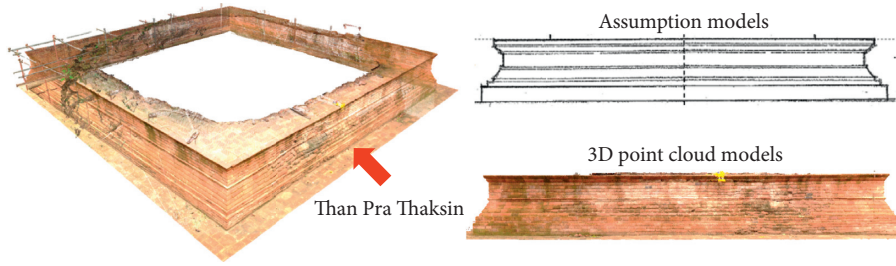


FIGURE 17: Addition of the Than Pra Thaksin section of the Wat Krachee pagoda.

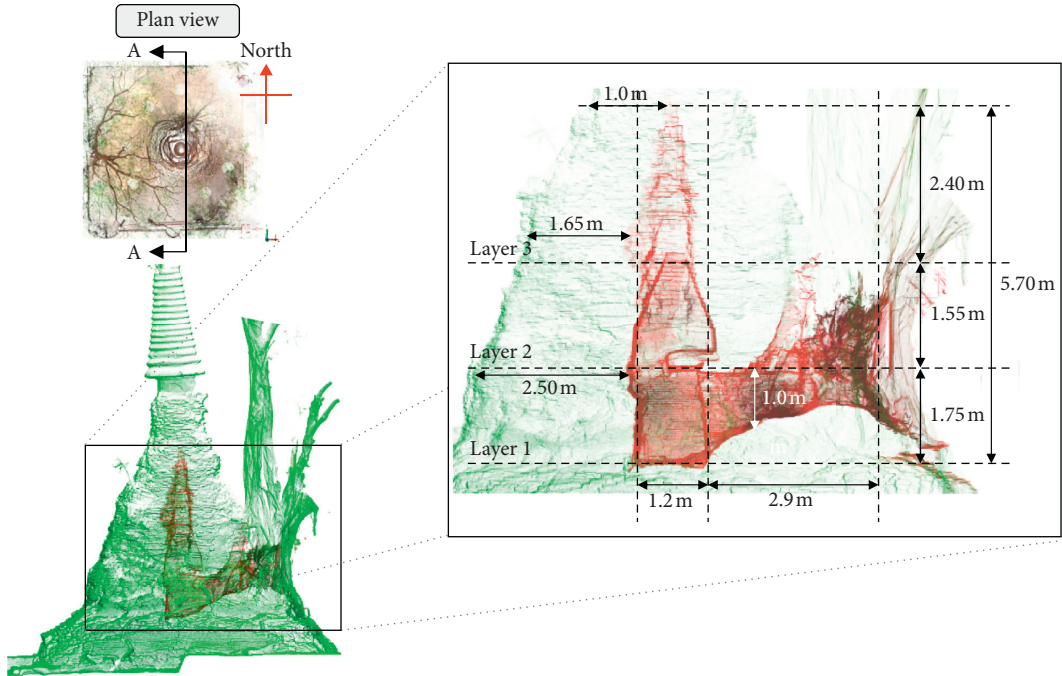


FIGURE 18: Section A-A in the west direction.

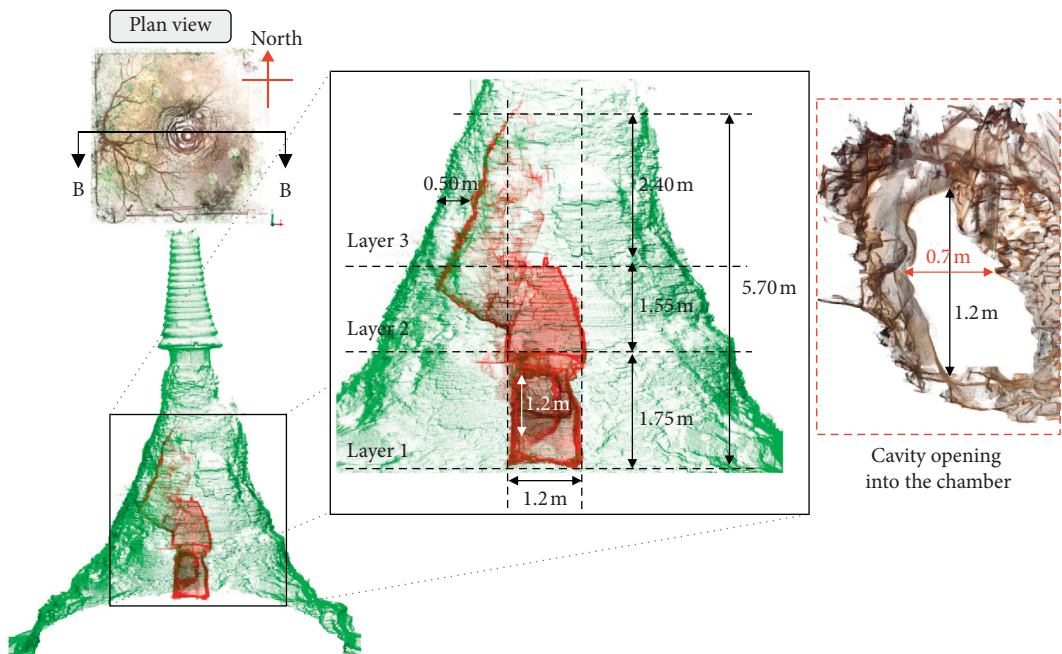


FIGURE 19: Section B-B in the south direction and a cavity opening into the chamber.

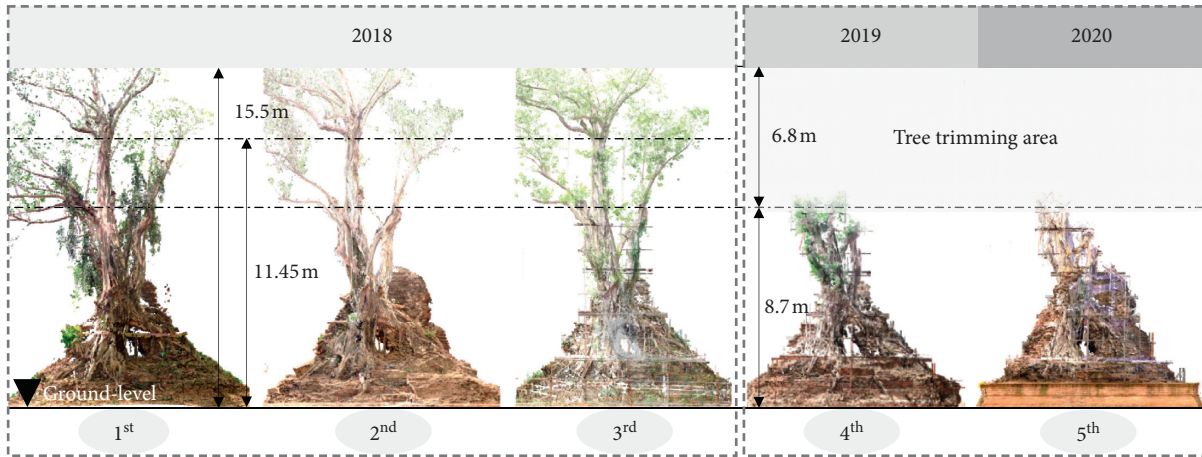


FIGURE 20: The changing of the trees surrounding the Wat Krachee.

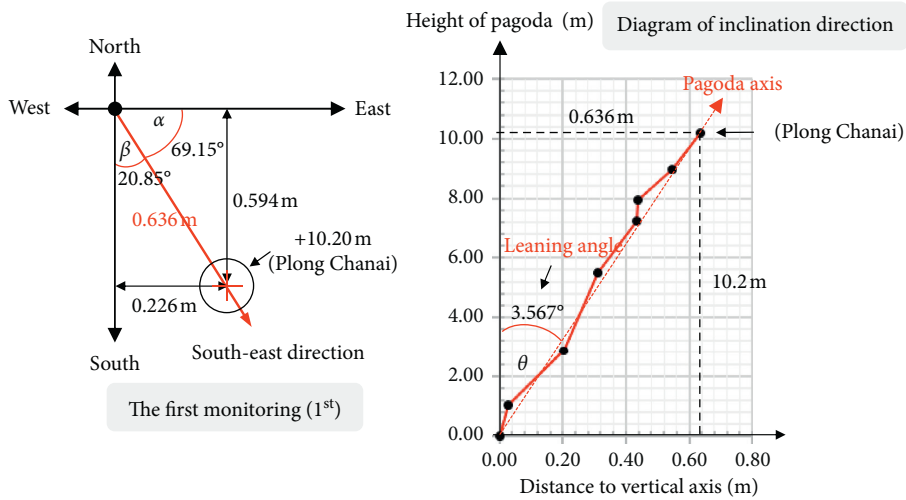


FIGURE 21: First monitoring session (February 2018).

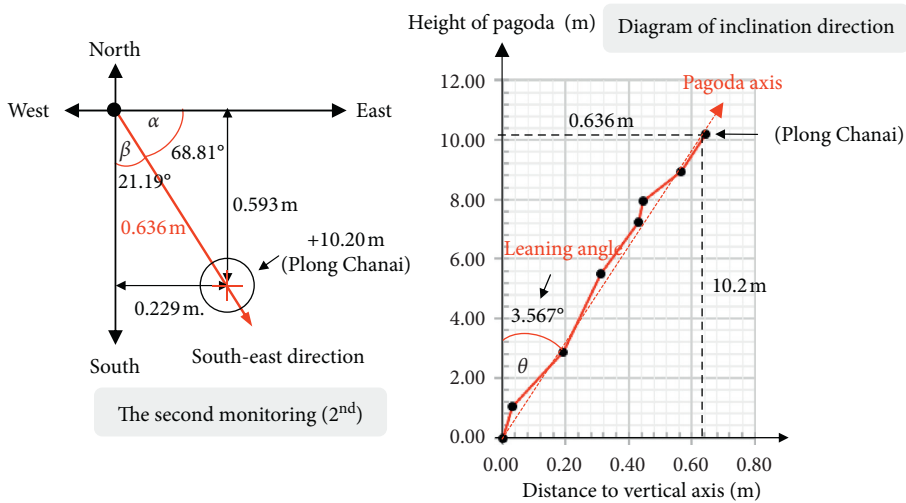


FIGURE 22: Second monitoring session (March 2018).

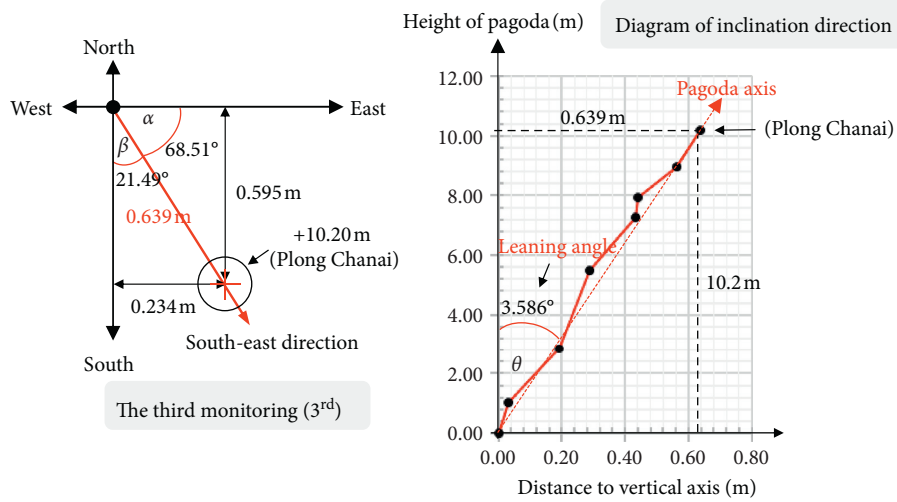


FIGURE 23: Third monitoring session (July 2018).

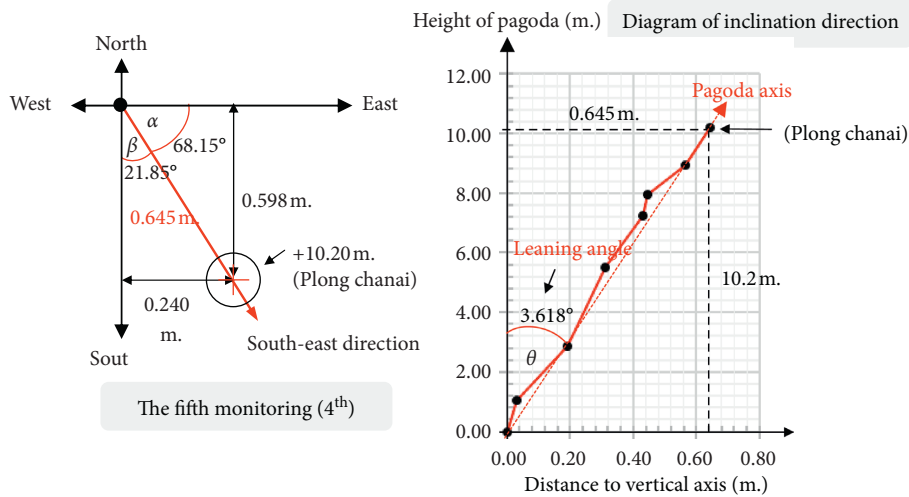


FIGURE 24: Fourth monitoring session (July 2019).

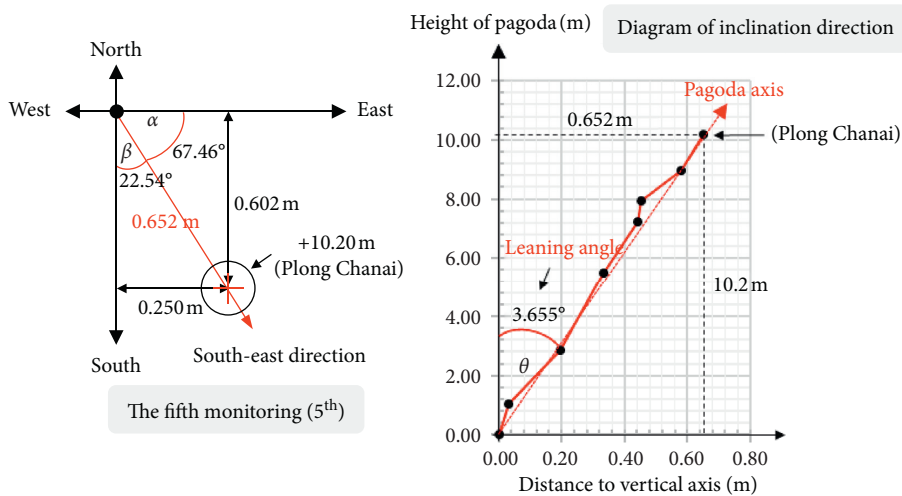


FIGURE 25: Fifth monitoring session (August 2020).

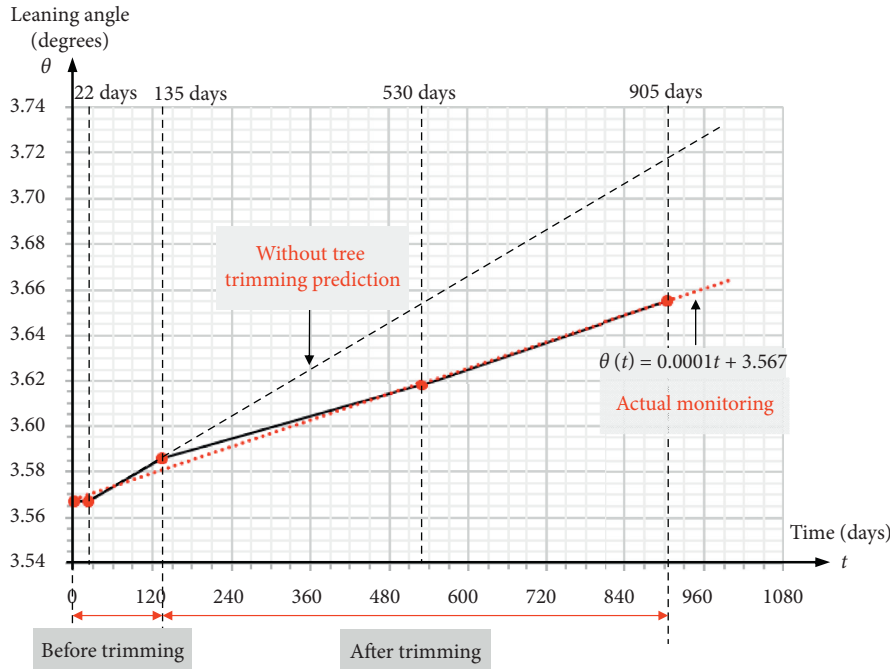


FIGURE 26: The relationship between time and the leaning angle of the Wat Krachee pagoda.

$$\theta(t) = 0.0001t + 3.567, \quad (1)$$

$$\frac{d\theta}{dt} = 0.0001, \quad (2)$$

where θ is the leaning angle of the pagoda in degrees and t is the time in days. Equation (1) was used to forecast the leaning angle of the pagoda with the initial leaning angle equal to 3.567 degrees, as measured in 2018. This equation can also predict the increase in the leaning angle for the structural stability assessment of the pagoda and restoration planning in the future. Moreover, the rate of increase in the leaning angle of the pagoda can be predicted using equation (2).

5. Conclusions

This article has presented an alternative method for the long-term monitoring and preservation of Thai pagodas based on TLS combined with permanent survey markers. The Wat Krachee pagoda in the Ayutthaya Province of Thailand was selected as a case study because of the challenges presented by its geometric configuration and the two intertwined trees growing within it. The massive amount of three-dimensional data from TLS technology is valuable for structural stability assessment in the long term. Moreover, the permanent survey markers were constructed to constrain the point cloud dataset. This method significantly reduced the alignment error in the data processing and increased the accuracy of the data analysis process. Throughout the five monitoring sessions over a period of two years and six months, the results revealed that 3D point cloud models provide high-precision dimensions and geometric shapes for the current pagoda condition. The pagoda leaning angle was assessed to continue to protect it from damage.

Furthermore, a challenge of this project involved deciding whether to trim the trees or not. During a meeting, most of the individuals on the conservation project team agreed to recommend trimming the trees adjacent to the Wat Krachee pagoda. The results revealed that the tree trimming significantly decreased the leaning angle of the pagoda. For long-term monitoring, an equation was developed to predict the pagoda leaning angle for preservation and restoration planning. In addition, data from the terrestrial laser scanner were used to create a realistic drawing of the plan before the reconstruction phase. In 2020, this method was found to be beneficial to the conservation work of the pagoda, and the teams completely and successfully restored the pagoda's Than Pra Thaksin elements. Finally, the original forms of several Thai pagodas need to be preserved, and monitoring using a terrestrial laser scanner would be an efficient alternative method for this preservation work.

Data Availability

The data used to support the findings of this study are included within the article.

Conflicts of Interest

The authors declare that they have no conflicts of interest to report regarding the present study.

Acknowledgments

The authors would like to acknowledge the Thailand Research Fund (TRF), the National Research Council of Thailand (NRCT), and King Mongkut's University of Technology Thonburi (KMUTT) for their joint support

through the Royal Golden Jubilee Ph.D. (RGJ-PHD) Program (Grant No. PHD/0042/2559) and acknowledge the Fine Arts Department in Thailand for their cooperation in our work concerning the Wat Krachee site in Ayutthaya.

References

- [1] Historic England, *3D Laser Scanning for Heritage: Advice and Guidance on the Use of Laser Scanning in Archaeology and Architecture*, Historic England, Swindon, UK, 2018.
- [2] L. Wilson, A. Rawlinson, A. Frost, and J. Hopher, "3D digital documentation for disaster management in historic buildings: applications following fire damage at the mackintosh building, the glasgow school of art," *Journal of Cultural Heritage*, vol. 31, pp. 24–32, 2018.
- [3] N. M. Noor, Z. Kamaruddin, A. Abdullah, M. A. Abdullah, S. S. Eusoff, and M. H. Mustafa, "Using terrestrial laser scanner for malay heritage documentation: preliminary approach to Istana Balai Besar, Kelantan," *International Journal of Development and Sustainability*, vol. 6, no. 6, pp. 1886–1897, 2018.
- [4] J. Shao, W. Zhang, N. Mellado et al., "Automated markerless registration of point clouds from TLS and structured light scanner for heritage documentation," *Journal of Cultural Heritage*, vol. 35, pp. 16–24, 2019.
- [5] M. A. Abbas, D. D. Lichti, A. K. Chong et al., "Improvements to the accuracy of prototype ship models measurement method using terrestrial laser scanner," *Measurement*, vol. 100, pp. 301–310, 2017.
- [6] W. Xie, Q. He, K. Zhang et al., "Application of terrestrial laser scanner on tidal flat morphology at a typhoon event time-scale," *Geomorphology*, vol. 292, pp. 47–58, 2017.
- [7] C. Vanneschi, M. Eyre, M. Francioni, and J. Coggan, "The use of remote sensing techniques for monitoring and characterization of slope instability," *Procedia Engineering*, vol. 191, pp. 150–157, 2017.
- [8] Z. Meng, M. He, Z. Tao et al., "Three-dimensional numerical modeling and roof deformation analysis of yuanjue cave based on point cloud data," *Advances in Civil Engineering*, vol. 2020, Article ID 8825015, 13 pages, 2020.
- [9] X. Xu, H. Yang, and I. Neumann, "Deformation monitoring of typical composite structures based on terrestrial laser scanning technology," *Composite Structures*, vol. 202, pp. 77–81, 2018.
- [10] H. Yang, M. Omidalizarandi, X. Xu, and I. Neumann, "Terrestrial laser scanning technology for deformation monitoring and surface modeling of arch structures," *Composite Structures*, vol. 169, pp. 173–179, 2017.
- [11] A. Pesci, G. Casula, and E. Boschi, "Laser scanning the Garisenda and Asinelli towers in Bologna (Italy): detailed deformation patterns of two ancient leaning buildings," *Journal of Cultural Heritage*, vol. 12, no. 2, pp. 117–127, 2011.
- [12] A. Costa-Jover, J. Lluís i Ginovart, S. Coll-Pla, and M. López Piquer, "Using the terrestrial laser scanner and simple methodologies for geometrically assessing complex masonry vaults," *Journal of Cultural Heritage*, vol. 36, pp. 247–254, 2019.
- [13] C. Castagnetti, E. Bertacchini, A. Capra, and M. Dubbini, "Terrestrial laser scanning for preserving cultural heritage: analysis of geometric anomalies for ancient structures," in *Proceedings of the FIG Working Week 2012*, Rome, Italy, May 2012.
- [14] M. Korumaz, M. Betti, A. Conti et al., "An integrated terrestrial laser scanner (TLS), deviation analysis (DA) and finite element (FE) approach for health assessment of historical structures. A minaret case study," *Engineering Structures*, vol. 153, pp. 224–238, 2017.
- [15] Q. Jiao, H. Jiang, and Q. Li, "Building earthquake damage analysis using terrestrial laser scanning data," *Advances in Civil Engineering*, vol. 2019, Article ID 8308104, 12 pages, 2019.
- [16] G. Fortunato, M. F. Funari, and P. Lonetti, "Survey and seismic vulnerability assessment of the baptistery of san giovanni in Tumba (Italy)," *Journal of Cultural Heritage*, vol. 26, pp. 64–78, 2017.
- [17] E. Quagliarini, P. Clini, and M. Ripanti, "Fast, low cost and safe methodology for the assessment of the state of conservation of historical buildings from 3D laser scanning: the case study of Santa Maria in Portonovo (Italy)," *Journal of Cultural Heritage*, vol. 24, pp. 175–183, 2017.
- [18] F. Micelli and A. Cascardi, "Structural assessment and seismic analysis of a 14th century masonry tower," *Engineering Failure Analysis*, vol. 107, Article ID 104198, 2020.
- [19] E. Bertacchini, E. Boni, A. Capra, C. Castagnetti, and M. Dubbini, "Terrestrial laser scanner for surveying and monitoring middle age towers," in *Proceedings of the XXIV International FIG Congress 2010*, Sydney, Australia, April 2010.
- [20] Y. H. Jo and C. H. Lee, "Displacement analysis of five-story stone pagoda in geumgolsan mountain, jindo, using terrestrial laser scanning," *Indian Journal of Science and Technology*, vol. 9, pp. 1–6, 2016.
- [21] L. Fregonese, G. Barbieri, L. Biolzi, M. Bocciarelli, A. Frigeri, and L. Taffurelli, "Surveying and monitoring for vulnerability assessment of an ancient building," *Sensors*, vol. 13, no. 8, pp. 9747–9773, 2013.
- [22] G. Teza and A. Pesci, "Geometric characterization of a cylinder-shaped structure from laser scanner data: development of an analysis tool and its use on a leaning bell tower," *Journal of Cultural Heritage*, vol. 14, no. 5, pp. 411–423, 2013.
- [23] S. Leelataviwat, C. Athisakul, W. Tangchirapat, and R. Sahamitmongkol, *Development of Engineering Database for Assessment and Structural Health Monitoring of Thailand Historic Structures*, Department of Civil Engineering, Faculty of Engineering, King Mongkut's University of Technology Thonburi, Bangkok, Thailand, (in Thailand), 2018.
- [24] P. Deesomchoke, *Project for Restoring Thai Local Wisdom in Architecture Craftsmen for Conservation of World Heritage Sites Project (Phase 2/Year 1-2018)*, Ayutthaya: Ayutthaya Historical Park Office, Ayutthaya, Thailand, (in Thailand), 2018.
- [25] P. Deesomchoke, *Integration Conference on Preservation Archaeological Remains in World Heritage at Ayuttaya*, Ayutthaya: Ayutthaya Historical Park Office, Ayutthaya, Thailand, (in Thailand), 2018.
- [26] A. Abellán, J. Calvet, J. M. Vilaplana, and J. Blanchard, "Detection and spatial prediction of rockfalls by means of terrestrial laser scanner monitoring," *Geomorphology*, vol. 119, no. 3–4, pp. 162–171, 2010.
- [27] FARO Technologies Inc., *FARO Focus 3D X-330 User Manuals*, FARO Technologies Inc., Lake Mary, FL, USA, 2015.
- [28] P. Pueschel, "The influence of scanner parameters on the extraction of tree metrics from FARO photon 120 terrestrial laser scans," *ISPRS Journal of Photogrammetry and Remote Sensing*, vol. 78, pp. 58–68, 2013.
- [29] The 3rd Regional Office of Fine Arts Department, *The Knowledge Management Project of the Bell-shaped Pagodas in the Ayutthaya Period*, The 3rd Regional Office of Fine Arts Department, Ayutthaya, Thailand, (in Thailand), 2013.

Research Article

A New Artificial Neural Network Model for the Prediction of the Effect of Molar Ratios on Compressive Strength of Fly Ash-Slag Geopolymer Mortar

Shaise K. John,¹ Alessio Cascardi ,² Yashida Nadir ,¹ Maria Antonietta Aiello ,^{2,3} and K. Girija¹

¹Department of Civil Engineering, College of Engineering Trivandrum, Thiruvananthapuram, Kerala, India

²ITC–Construction Technologies Institute, CNR–Italian National Research Council, Bari, Italy

³Department of Innovation Engineering, University of Salento, Lecce, Italy

Correspondence should be addressed to Alessio Cascardi; alessio.cascardi@itc.cnr.it

Received 28 October 2020; Revised 18 March 2021; Accepted 27 April 2021; Published 7 May 2021

Academic Editor: Svetlana Olbina

Copyright © 2021 Shaise K. John et al. This is an open access article distributed under the Creative Commons Attribution License, which permits unrestricted use, distribution, and reproduction in any medium, provided the original work is properly cited.

Geopolymers are inorganic polymers produced by the alkali activation of alumina-silicate minerals. Geopolymer is an alternative cementitious binder to traditional Ordinary Portland Cement (OPC) leading to economical and sustainable construction technique by the utilisation of alumina-silicate waste materials. The strength development in fly ash-slag geopolymer mortar is dependent on the chemical composition of the raw materials. An effective way to study the effect of chemical components in geopolymer is through the evaluation of molar ratios. In this study, an Artificial Neural Network (ANN) model has been applied to predict the effect of molar ratios on the 28-day compressive strength of fly ash-slag geopolymer mortar. For this purpose, geopolymer mortar samples were prepared with different fly ash-slag composition, activator concentration, and alkaline solution ratios. The molar ratios of the geopolymer mortar samples were evaluated and given as input to ANN, and the compressive strength was obtained as the output. The accuracy of the assessed model was investigated by statistical parameters; the mean, median, and mode values of the ratio between actual and predicted strength are equal to 0.991, 0.973, and 0.991, respectively, with a 14% coefficient of variation and a correlation coefficient of 89%. Based on the mentioned findings, the proposed novel model seems reliable enough and could be used for the prediction of compressive strength of fly ash-slag geopolymer. In addition, the influence of molar compositions on the compressive strength was further investigated through parametric studies utilizing the proposed model. The percentages of Na₂O and SiO₂ of the source materials were observed as the dominant chemical compounds in the mix affecting the compressive strength. The influence of CaO was significant when combined with a high amount of SiO₂ in alkaline solution.

1. Introduction

Production of *Ordinary Portland Cement* (OPC) is an energy-intensive process that consumes enormous amount of energy and results in emission of substantial amount of carbon dioxide into the atmosphere leading to global warming and atmospheric pollution [1–3]. Burning of fossil fuels and the calcination of limestone are both responsible for carbon dioxide emission during OPC manufacturing. A cumulative amount of 4.5 GtC has been sequestered in carbonating cement materials from 1930 to 2013, offsetting

43% of the CO₂ emissions from production of cement over the same period, not including emissions associated with fossil use during cement production [4]. For the past few decades, researchers are investigating alternative materials for OPC due to environmental concern, and geopolymer is identified as an excellent solution in this regard. Geopolymer is an inorganic polymer produced by the polymerization of alumina-silicate minerals activated with high-concentration alkali solutions [5]. The most widely available alumina-silicate minerals are Fly Ash (FA), metakaolin, Ground Granulated Blast Furnace Slag (GGBFS), rice husk ash, palm

oil fuel ash, etc. [6]. FA is an industrial waste resulting from the burning of coal in thermal power plant with a chemical composition based essentially on SiO_2 and Al_2O_3 , and GGBFS is produced from slag resulting from steel manufacturing with a chemical composition based essentially on CaO , SiO_2 , and Al_2O_3 . Both FA and GGBFS are pozzolanic materials which are generally blended with OPC to produce Portland pozzolanic cement and are also used as workability-improving admixtures [7]. However, a tremendous amount of these waste materials is still landfilled. A promising solution seems to be the complete substitution of Portland cement with fly ash-based geopolymers, as an eco-friendly and sustainable construction material.

FA-based geopolymers are gaining interest due to their availability as alumina-silicate mineral. In addition, the partial replacement of fly ash by various additives such as GGBFS, lime, and silica resulted in improved mechanical properties; for instance, the combination of FA and GGBFS yielded better compressive strength [8]. Due to improved mechanical properties, fly ash-slag-based geopolymers were found superior to fly ash geopolymers [6, 8–11]. The oxides of calcium are highly reactive and result in increased compressive strength for fly ash-slag geopolymers. In fact, the calcium dissolving from GGBFS is responsible for early- and late-age properties. The presence of GGBFS increases the long-term resistance as it continues the reaction for a longer duration and at the same time accelerates the achievement of short-term resistance. The addition of slag into FA geopolymer is also advantageous for overcoming drawbacks related to reduced workability and setting time [6, 12–14]. Elevated temperature curing in fly ash-based geopolymers causes evaporation of water from the pores resulting in increased pore structure; thus, lower curing temperature and longer curing duration become significant targets [15]. Partial replacement of fly ash by GGBFS enables geopolymerization at ambient curing conditions, which makes it superior for practical applications [16, 17]; in fact, greater compressive strength can be obtained for fly ash-slag geopolymer cured at ambient conditions compared with heat-cured fly ash geopolymer [12].

The chemical composition of the source materials, alkali concentration, and percentage replacement of FA by GGBFS are major factors which influences the strength of FA-slag geopolymer. The chemical components SiO_2 , Al_2O_3 , Na_2O , and CaO of the source materials have significant effect on the properties of geopolymer [18]. Chemical optimisation of Si : Al and Na : Al molar ratios is also found to have an effect on compressive strength [19]. The Al ions appear to have a dominant effect on setting time of geopolymer and increasing the molar ratio of $\text{SiO}_2/\text{Al}_2\text{O}_3$ is largely responsible for high-strength gain at later stages [20]. The composition of C-A-S-H gel produced by the alkaline activation of slag and Na-A-S-H gel produced by FA largely affects the system mechanical strength and durability [21]. The characteristics of the gel depend on the molar ratios CaO/SiO_2 in slag and $\text{SiO}_2/\text{Al}_2\text{O}_3$ in FA geopolymers. Multicomponent activators using sodium hydroxide and sodium silicate solutions are found better than sodium hydroxide or sodium silicate alone. Sodium silicate-to-sodium hydroxide ratios varying

from 1 to 2.5 are suggested for obtaining higher compressive strength [22–25]. The concentration of sodium hydroxide also plays a crucial role in geopolymerization and should be sufficient for the leaching of oxides of alumina-silicates from the source materials [26–28]. Also, the compressive strength increases with the increase in the concentration of sodium hydroxide. Studies show that the optimum compressive strength was obtained at various percentage replacements of FA by GGBFS from 15 to 40% [8, 9, 12]; the variation in strength development and optimum slag content may be due to the FA composition and activator concentrations [29]. The complexity of the effect of variables on the compressive strength can be evaluated through mathematical modelling; in particular, those considering molar ratios as key parameters have been found effective in predicting the compressive strength of alkali activated phosphorous slag [30]. Literatures on the influence of chemical composition on compressive strength of FA-slag geopolymer using ANN are lacking.

In this research, an experimental investigation was conducted to evaluate the influence of alkali concentration, ratio of various alkalis used for geopolymerization, and percentage of replacement of FA by slag on the compressive strength of FA-slag geopolymer mortar. A replacement percentage of FA by slag equal to 10%, 20%, 30%, and 40% is considered in this paper. The NaOH concentrations are varied from 8 M to 14 M with 2 M increment based on previous studies [31–35]. The various ratios of $\text{NaOH}/\text{Na}_2\text{SiO}_3$ were 1, 1.5, 2, and 2.5. The ratios were selected based on previous studies where the optimum value lies between 1 and 2.5 [31]. The 28-day compressive strength for 56 combinations of these parameters was experimentally obtained. The molar compositions of various components are calculated from the chemical composition of each raw material. The experimental results in terms of compressive strength are, thus, reported and discussed. Based on experimental outcomes, an ANN model is proposed, able to predict the compressive strength on the basis of chemical parameters, SiO_2 , Al_2O_3 , Na_2O , and CaO . The reliability of the proposed model is investigated, confirming its effectiveness at least in relation to the range of findings and variables referred to the present experimental campaign.

2. Experimental Program

2.1. Materials. Fly ash used in this study was generated in *Tuticorin* coal-fired thermal power plant, India. The fly ash belonged to class F with a low calcareous content and high siliceous content according to IS 3812-1 [36]. The material had a mean particle size of $24\ \mu\text{m}$, specific gravity of 2.97 kg/mc, and fineness of $365\ \text{m}^2/\text{kg}$ by Blaine's air permeability test. The GGBFS was supplied by JSW Cement Ltd., India. The material had a mean particle size of $20\ \mu\text{m}$, specific gravity of 2.91 kg/mc, and fineness of $382\ \text{m}^2/\text{kg}$ by Blaine's air permeability test. The chemical composition of FA and GGBFS obtained by XRF analysis and expressed as the weight percentage (wt%) is given in Table 1. The raw constituents are shown in Figure 1.

TABLE 1: Chemical composition of fly ash and GGBFS.

Chemical composition	Component (wt%)	
	FA	GGBFS
SiO ₂	61.53	33.81
Al ₂ O ₃	25.19	19.52
Fe ₂ O ₃	5.39	0.49
CaO	1.31	35.22
MgO	0.63	6.68
SO ₃	0.82	1.40
Na ₂ O	0.39	0.34
TiO ₂	0.65	0.94
MnO	0.30	0.96
K ₂ O	0.23	0.44
LOI*	0.95	0.11

*Loss on ignition.

The fine aggregate used was quarry dust [37] obtained as a byproduct from an aggregate crusher and supplied from an M-sand manufacturing unit Poabs Ltd., Trivandrum. The material has a particle size less than 600 μm . The alkaline solution used was a combination of sodium hydroxide (NaOH) and sodium silicate (Na₂SiO₃). For the preparation of NaOH solution, industrial-grade NaOH in flake form and white colour with 98% purity was used. Commercially available liquid sodium silicate light greyish in colour and having 49.7% solid content was used, whose composition is given in Table 2.

2.2. Mix Proportion and Specimen Preparation.

Geopolymer mortar was prepared with a fine aggregate-to-binder ratio 1 : 2 by weight. An alkaline fluid-to-binder ratio of 0.5 was fixed in the study [37]. Four different concentrations of NaOH, viz., 8 M, 10 M, 12 M, and 14 M, and sodium silicate to NaOH ratios, namely, 1, 1.5, 2, and 2.5, were used for the preparation of geopolymer mortar. Fly ash replacement by slag was also considered in various proportions: 10%, 20%, 30%, and 40%. Ambient curing conditions were adopted for all the specimens (i.e., 25–28°C and ~70% RH). The superplasticizer used was Complast SP430-grade from Fosroc Ltd. Table 3 shows the mix proportioning details utilized in the investigation. FA stands for fly ash, NH for sodium hydroxide, NS for sodium silicate, and SP for superplasticizer. The first two numbers in the mix ID stand for percentage replacement of fly ash by slag, S for slag, the next number for the molarity of sodium hydroxide (e.g., 8 M for 8 molar concentration), and the last number for the sodium hydroxide-to-sodium silicate ratio. A total number of 56 mixes were designed as shown in Table 3. For mixes with 14 M concentrations, alkaline solution ratios of 1 and 1.5 were excluded in Table 3 since they had exhibited high viscosity nature like a gel.

2.3. Mixing, Casting, and Curing. The NaOH flakes were diluted in potable water at ambient temperature and then mixed to sodium silicate solution. The alkaline solution was prepared 24 hours prior to mixing to reduce excessive heat generation. The dry binder (fly ash, slag, and fine aggregate)

was mixed for 2 minutes to attain homogeneity. Mixing was done using a handheld putty mixer at 600 rpm. The calculated quantity of premixed alkaline solution was added gradually to the dry binder and mixed thoroughly. Later, the premixed superplasticizer and water were added, and mixing is continued for further 5 minutes. Cylindrical specimens [2] of 70 mm diameter and 140 mm height were cast in PVC moulds. The mould was filled in three layers with each layer compacted by a vibrator. A total of 56 mixes were designed in the study and 6 specimens were cast for each mix. After casting, the specimens were kept in moulds for 48 hours and after demoulding were left at room temperature to achieve 28 days of ambient curing. Before testing, the end faces of the cylinders were smoothed using an angle grinder to avoid any surface irregularities and, thus, possible stress concentrations under loading. Figure 2 shows the mixing, casting, cast, and demoulded geopolymer mortar specimens.

2.4. Testing. Compressive strength of geopolymer mortar was evaluated by compression test on cylindrical specimens made by a UTM of capacity 3000 kN, according to ASTM C873M standard [38]. The UTM was also equipped with a load cell of 50 T capacity for a more accurate and finer reading (see Figure 3). The load cell used had a least count of 0.1 T. The failure type observed in the specimens is similar to that generally expected for cement-based mortar, namely, cracking along the length of the specimen (see Figure 3).

3. Results and Discussion

Figures 4(a)–4(d) indicate the 28-day cylindrical compressive strength of ambient cured fly ash-slag geopolymer mortar for 8 M, 10 M, 12 M, and 14 M NaOH concentrations, respectively.

As the percentage replacement of FA by GGBFS increases, the compressive strength is found to be increasing for all the mixes. The percentage gain in compressive strength for most cases was more pronounced passing from 20% to 30% replacement of FA by GGBFS; this result is evident for 10 M NH concentration and 12 M NH concentration, while for 14 M NH only at NS to NH ratio of 2, the same trend is confirmed. In the case of 8 M NH concentration, the greatest increase of compressive strength occurs when passing from 30% to 40% of GGBFS replacement. The maximum compressive strength was obtained for mix with 40% FA replaced by GGBFS, 10 M NH concentration, and NS/NH ratio of 2. The increased compressive strength with moderate addition of GGBFS is due to the simultaneous formation of two separate phases: NASH gel formed through the activation of fly ash and CASH gel formed through the activation of slag. The addition of slag reduced porosity; the matrix was compact with better space-filling properties of CASH gel compared with the NASH gel. The significant increase in strength is also due to strong load-bearing CASH gel formed [39]. Depending upon the alkalinity, the dissolved calcium from GGBFS increases; the formation of NASH gel and CASH gel competes for soluble silicates and available space for growth. Consequently,

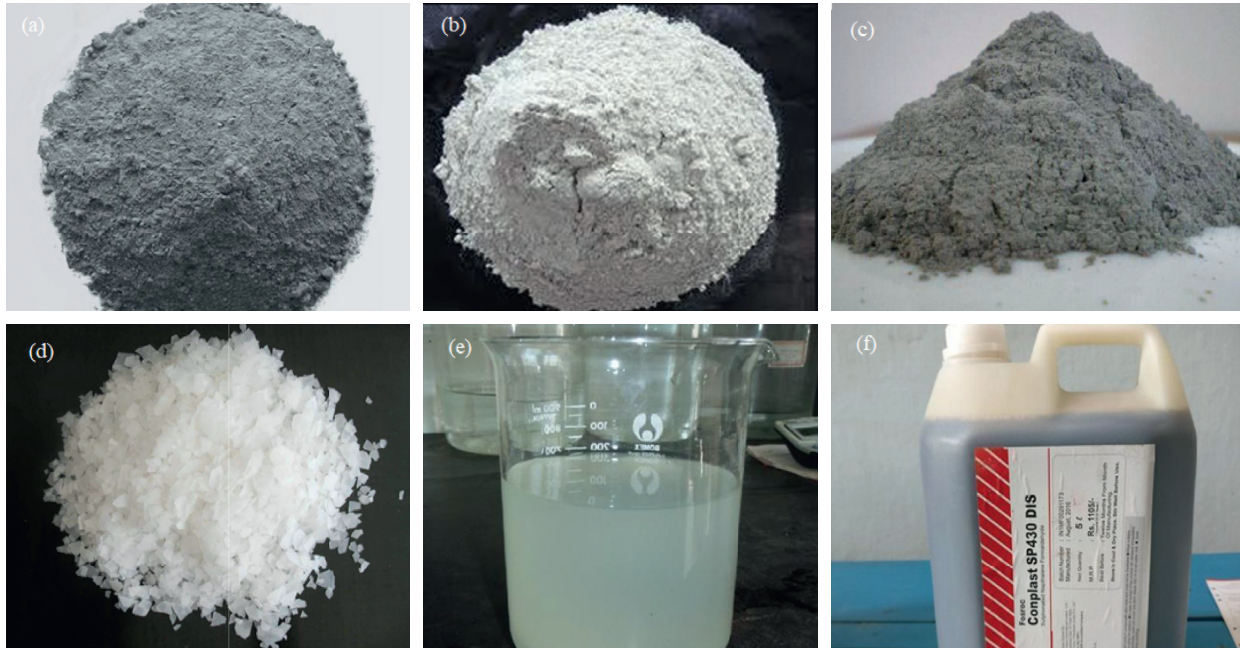


FIGURE 1: Raw constituents of the geopolymer mortar. (a) FA. (b) GGBFS. (c) Quarry dust. (d) NaOH flakes. (e) Sodium silicate solution. (f) Superplasticizer.

instead of having one phase acting as microaggregates, the resultant binder will be disordered with similar-size phases resulting in strength reduction [40].

For 8 M of NH concentration, the strength was relatively lower due to lower Na_2O content. At lower concentrations of NH, the dissolution of Al and Si ions is lesser, which results in weak polymer chains and thus lower strength. At 10 M concentration of NH, the leaching of Al and Si ions is maximum, which enables polycondensation process. Beyond 10 M, leaching of alumina-silicates remains almost constant or hinders polycondensation process [41, 42]. As the NS/NH ratio is increased, the compressive strength increases almost linearly due to the reactive silicate content in the NS. But as the concentration of NH is equal to or more than 10 M, the compressive strength increases up to an NS/NH ratio of 2 and then decreases. When NS/NH ratio is increased, the excess silicate content hinders water evaporation and causes geopolymer chain to break down into individual monomer, thus reducing the strength [43, 44]. The factors affecting the compressive strength of fly ash-slag geopolymer are basically related to the molar compositions; in particular, the alumina-silicate minerals in the source materials (Al_2O_3 and SiO_2), the CaO content in slag, Na_2O content in the alkaline solution, and $(\text{SiO}_2)/\text{L}$ content in the NS. As the influence of these variables is complex in nature, it cannot be experimentally evaluated; mathematical modelling of the molar composition is a possible way to understand its influence. The proposed model is based on ANN to predict the compressive strength of fly ash-slag

TABLE 2: Composition of sodium silicate.

Material	Chemical composition (wt%)		
Na_2SiO_3	Na_2O	SiO_2	Water
	14.7	35	50.3

geopolymer and to evaluate the influence of the molar composition on its values.

4. Artificial Neural Networks (ANNs) Method

Artificial Neural Networks (ANNs) are a biologically inspired computational method able to extract knowledge from a relatively large database. In particular, the development of ANNs was inspired by the running of the human nervous central system. ANNs cannot approach the complexity of the brain, but there are two key correspondences between biological neural networks and ANNs themselves. First, both networks are computational devices with a huge level of interconnection. Second, the connections between neurons determine the function of the network; a human brain approximately has 10^{10} neurons, which communicate through a network. ANNs function as parallel distributed computing networks of n -node, analogous to biological neural systems. Each input is associated with a relative weight (w_1, w_2, \dots, w_n) and a bias (b_1, b_2, \dots, b_n) which affect the impact of the inputs. Weights and bias are adaptive coefficients within the network that determine the intensity of the input signal as reported in equation (1). The output

TABLE 3: Mix proportion details of geopolymer mortar (kg/m³).

Mix ID	FA	GGBFS	Sand	NH	NS	Water	SP
10S8M1	567	63	1260	157.5	157.5	189	3.15
20S8M1	504	126	1260	157.5	157.5	189	3.15
30S8M1	441	189	1260	157.5	157.5	189	3.15
40S8M1	378	252	1260	157.5	157.5	189	3.15
10S8M1.5	567	63	1260	126	189	189	3.15
20S8M1.5	504	126	1260	126	189	189	3.15
30S8M1.5	441	189	1260	126	189	189	3.15
40S8M1.5	378	252	1260	126	189	189	3.15
10S8M2	567	63	1260	105	210	189	3.15
20S8M2	504	126	1260	105	210	189	3.15
30S8M2	441	189	1260	105	210	189	3.15
40S8M2	378	252	1260	105	210	189	3.15
10S8M2.5	567	63	1260	90	225	189	3.15
20S8M2.5	504	126	1260	90	225	189	3.15
30S8M2.5	441	189	1260	90	225	189	3.15
40S8M2.5	378	252	1260	90	225	189	3.15
10S10M1	567	63	1260	157.5	157.5	189	3.15
20S10M1	504	126	1260	157.5	157.5	189	3.15
30S10M1	441	189	1260	157.5	157.5	189	3.15
40S10M1	378	252	1260	157.5	157.5	189	3.15
10S10M1.5	567	63	1260	126	189	189	3.15
20S10M1.5	504	126	1260	126	189	189	3.15
30S10M1.5	441	189	1260	126	189	189	3.15
40S10M1.5	378	252	1260	126	189	189	3.15
10S10M2	567	63	1260	105	210	189	3.15
20S10M2	504	126	1260	105	210	189	3.15
30S10M2	441	189	1260	105	210	189	3.15
40S10M2	378	252	1260	105	210	189	3.15
10S10M2.5	567	63	1260	90	225	189	3.15
20S10M2.5	504	126	1260	90	225	189	3.15
30S10M2.5	441	189	1260	90	225	189	3.15
40S10M2.5	378	252	1260	90	225	189	3.15
10S12M1	567	63	1260	157.5	157.5	189	3.15
20S12M1	504	126	1260	157.5	157.5	189	3.15
30S12M1	441	189	1260	157.5	157.5	189	3.15
40S12M1	378	252	1260	157.5	157.5	189	3.15
10S12M1.5	567	63	1260	126	189	189	3.15
20S12M1.5	504	126	1260	126	189	189	3.15
30S12M1.5	441	189	1260	126	189	189	3.15
40S12M1.5	378	252	1260	126	189	189	3.15
10S12M2	567	63	1260	105	210	189	3.15
20S12M2	504	126	1260	105	210	189	3.15
30S12M2	441	189	1260	105	210	189	3.15
40S12M2	378	252	1260	105	210	189	3.15
10S12M2.5	567	63	1260	90	225	189	3.15
20S12M2.5	504	126	1260	90	225	189	3.15
30S12M2.5	441	189	1260	90	225	189	3.15
40S12M2.5	378	252	1260	90	225	189	3.15
10S14M2	567	63	1260	105	210	189	3.15
20S14M2	504	126	1260	105	210	189	3.15
30S14M2	441	189	1260	105	210	189	3.15
40S14M2	378	252	1260	105	210	189	3.15
10S14M2.5	567	63	1260	90	225	189	3.15
20S14M2.5	504	126	1260	90	225	189	3.15
30S14M2.5	441	189	1260	90	225	189	3.15
40S14M2.5	378	252	1260	90	225	189	3.15

signal of a neuron is produced by the sum function, corresponding roughly to the biological cell body, which algebraically adds all the weighted inputs. In principle, ANNs

are able to adjust their inner structures in order to provide optimal solutions or prediction, given enough data and a proper initialization.



FIGURE 2: Mixing, casting, cast specimens, and demoulded geopolymer mortar specimens.

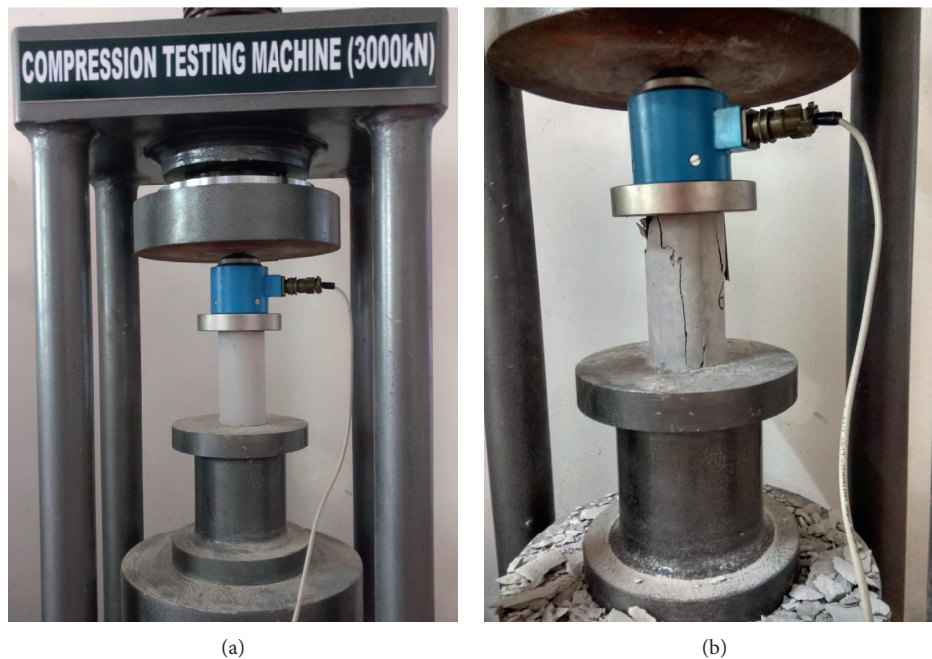


FIGURE 3: Compression test on geopolymer mortar cylinder: test setup (a) and typical failure mode (b).

Among the various types of ANNs, in this paper, a *multilayer perceptron* (MLP) with back-propagation learning algorithms is focused on. MLP is the ANN commonly used for a wide variety of problems [45–54]. It is based on a supervised procedure and generally comprises at least three

layers: *input* (i), *hidden* (h), and *output* (o). The procedure continually adjusts the weights of the connections in the network through a back-propagation method in order to minimize the scatter between the actual output vector of the network and the desired output vector (target of the

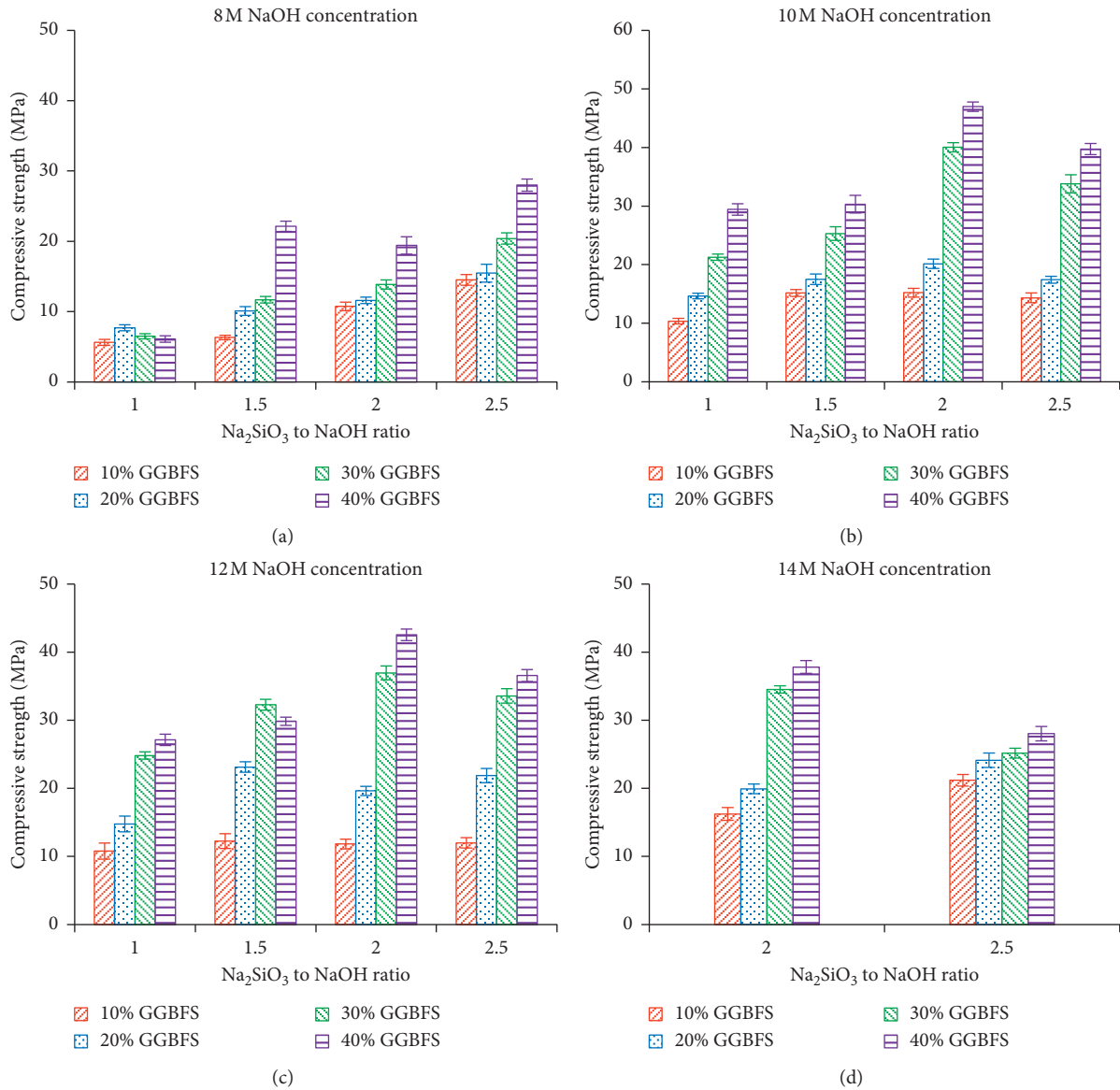


FIGURE 4: 28-day cylindrical compressive strength of fly ash-slag geopolymer mortar.

analysis). The information passes from the input layer to output layer through the hidden layer. All neurons from one layer are connected to the neurons in the next layers. These connections are represented as weights (connection intensity) in the computational process. The number of neurons in the input layer depends on the number of independent variables in the model, while the number of neurons in the output layer is equal to the number of dependent variables. Moreover, both the numbers of hidden layers and their neurons are dependent on the complexity of the model (set by the user) and are important parameters in the development of the MLP model. An MLP is trained/learned to minimize errors between the desired target values and the values computed from the model. If the network provides errors greater than a given threshold, the weights are updated for minimizing them. Thus, errors are reduced up to a small enough value. Finally, an activation function

(generally sigmoidal-like) passes the sum results in a [0, 1] range; in such way, the best-fitting neural path is identified.

$$y = b_n + \sum_{i=1}^n x_n \cdot w_n, \quad (1)$$

where b is the bias; x is the input; n is the number of datasets; y is the output; and w is the weight.

The ANN has also widely been used to model the behavior of concrete mixtures and elements, e.g., in [50–55].

5. The Proposed ANN-Model

Based on the abovementioned experimental evidence, a database was set for the ANN purpose as reported in Table 4. Since the molar composition was made up of five different

TABLE 4: ANN database.

#	Label	Molar composition (kg/m ³)					Inputs					Output $\sigma = f_c$
		Na ₂ O	(SiO ₂)L	SiO ₂	Al ₂ O ₃	CaO	i_1	i_2	i_3	i_4	i_5	
1	10S8M1	62.21	55.13	370.18	155.12	29.62	0.09	0.08	0.55	0.23	0.04	5.63
2	20S8M1	62.21	55.13	352.71	151.55	50.98	0.09	0.08	0.52	0.23	0.08	7.71
3	30S8M1	62.21	55.13	335.25	147.98	72.34	0.09	0.08	0.50	0.22	0.11	6.50
4	40S8M1	62.21	55.13	317.78	144.41	93.71	0.09	0.08	0.47	0.21	0.14	6.11
5	10S8M1.5	59.03	66.15	370.18	155.12	29.62	0.09	0.10	0.54	0.23	0.04	6.33
6	20S8M1.5	59.03	66.15	352.71	151.55	50.98	0.09	0.10	0.52	0.22	0.07	10.10
7	30S8M1.5	59.03	66.15	335.25	147.98	72.34	0.09	0.10	0.49	0.22	0.11	11.70
8	40S8M1.5	59.03	66.15	317.78	144.41	93.71	0.09	0.10	0.47	0.21	0.14	22.14
9	10S8M2	56.91	73.50	370.18	155.12	29.62	0.08	0.11	0.54	0.23	0.04	10.75
10	20S8M2	56.91	73.50	352.71	151.55	50.98	0.08	0.11	0.51	0.22	0.07	11.61
11	30S8M2	56.91	73.50	335.25	147.98	72.34	0.08	0.11	0.49	0.22	0.11	13.87
12	40S8M2	56.91	73.50	317.78	144.41	93.71	0.08	0.11	0.46	0.21	0.14	19.41
13	10S8M2.5	55.40	78.75	370.18	155.12	29.62	0.08	0.11	0.54	0.23	0.04	14.52
14	20S8M2.5	55.40	78.75	352.71	151.55	50.98	0.08	0.11	0.51	0.22	0.07	15.47
15	30S8M2.5	55.40	78.75	335.25	147.98	72.34	0.08	0.11	0.49	0.21	0.10	20.41
16	40S8M2.5	55.40	78.75	317.78	144.41	93.71	0.08	0.11	0.46	0.21	0.14	27.99
17	10S10M1	71.98	55.13	370.18	155.12	29.62	0.11	0.08	0.54	0.23	0.04	10.36
18	20S10M1	71.98	55.13	352.71	151.55	50.98	0.11	0.08	0.52	0.22	0.07	14.65
19	30S10M1	71.98	55.13	335.25	147.98	72.34	0.11	0.08	0.49	0.22	0.11	21.27
20	40S10M1	71.98	55.13	317.78	144.41	93.71	0.11	0.08	0.47	0.21	0.14	29.42
21	10S10M1.5	66.84	66.15	370.18	155.12	29.62	0.10	0.10	0.54	0.23	0.04	15.17
22	20S10M1.5	66.84	66.15	352.71	151.55	50.98	0.10	0.10	0.51	0.22	0.07	17.51
23	30S10M1.5	66.84	66.15	335.25	147.98	72.34	0.10	0.10	0.49	0.21	0.11	25.30
24	40S10M1.5	66.84	66.15	317.78	144.41	93.71	0.10	0.10	0.46	0.21	0.14	30.33
25	10S10M2	63.42	73.50	370.18	155.12	29.62	0.09	0.11	0.54	0.22	0.04	15.21
26	20S10M2	63.42	73.50	352.71	151.55	50.98	0.09	0.11	0.51	0.22	0.07	20.15
27	30S10M2	63.42	73.50	335.25	147.98	72.34	0.09	0.11	0.48	0.21	0.10	40.04
28	40S10M2	63.42	73.50	317.78	144.41	93.71	0.09	0.11	0.46	0.21	0.14	46.97
29	10S10M2.5	60.98	78.75	370.18	155.12	29.62	0.09	0.11	0.53	0.22	0.04	14.34
30	20S10M2.5	60.98	78.75	352.71	151.55	50.98	0.09	0.11	0.51	0.22	0.07	17.42
31	30S10M2.5	60.98	78.75	335.25	147.98	72.34	0.09	0.11	0.48	0.21	0.10	33.80
32	40S10M2.5	60.98	78.75	317.78	144.41	93.71	0.09	0.11	0.46	0.21	0.13	39.73
33	10S12M1	81.74	55.13	370.18	155.12	29.62	0.12	0.08	0.54	0.22	0.04	10.79
34	20S12M1	81.74	55.13	352.71	151.55	50.98	0.12	0.08	0.51	0.22	0.07	14.78
35	30S12M1	81.74	55.13	335.25	147.98	72.34	0.12	0.08	0.48	0.21	0.10	24.83
36	40S12M1	81.74	55.13	317.78	144.41	93.71	0.12	0.08	0.46	0.21	0.14	27.12
37	10S12M1.5	74.66	66.15	370.18	155.12	29.62	0.11	0.10	0.53	0.22	0.04	12.26
38	20S12M1.5	74.66	66.15	352.71	151.55	50.98	0.11	0.10	0.51	0.22	0.07	23.14
39	30S12M1.5	74.66	66.15	335.25	147.98	72.34	0.11	0.09	0.48	0.21	0.10	32.28
40	40S12M1.5	74.66	66.15	317.78	144.41	93.71	0.11	0.09	0.46	0.21	0.13	29.85
41	10S12M2	69.93	73.50	370.18	155.12	29.62	0.10	0.11	0.53	0.22	0.04	11.83
42	20S12M2	69.93	73.50	352.71	151.55	50.98	0.10	0.11	0.50	0.22	0.07	19.63
43	30S12M2	69.93	73.50	335.25	147.98	72.34	0.10	0.11	0.48	0.21	0.10	36.96
44	40S12M2	69.93	73.50	317.78	144.41	93.71	0.10	0.11	0.45	0.21	0.13	42.55
45	10S12M2.5	66.56	78.75	370.18	155.12	29.62	0.10	0.11	0.53	0.22	0.04	12.00
46	20S12M2.5	66.56	78.75	352.71	151.55	50.98	0.10	0.11	0.50	0.22	0.07	21.88
47	30S12M2.5	66.56	78.75	335.25	147.98	72.34	0.09	0.11	0.48	0.21	0.10	33.58
48	40S12M2.5	66.56	78.75	317.78	144.41	93.71	0.09	0.11	0.45	0.21	0.13	36.57
49	10S14M2	76.44	73.50	370.18	155.12	29.62	0.11	0.10	0.53	0.22	0.04	16.25
50	20S14M2	76.44	73.50	352.71	151.55	50.98	0.11	0.10	0.50	0.21	0.07	19.93
51	30S14M2	76.44	73.50	335.25	147.98	72.34	0.11	0.10	0.48	0.21	0.10	34.53
52	40S14M2	76.44	73.50	317.78	144.41	93.71	0.11	0.10	0.45	0.20	0.13	37.83
53	10S14M2.5	72.14	78.75	370.18	155.12	29.62	0.10	0.11	0.52	0.22	0.04	21.19
54	20S14M2.5	72.14	78.75	352.71	151.55	50.98	0.10	0.11	0.50	0.21	0.07	24.13
55	30S14M2.5	72.14	78.75	335.25	147.98	72.34	0.10	0.11	0.47	0.21	0.10	25.17
56	40S14M2.5	72.14	78.75	317.78	144.41	93.71	0.10	0.11	0.45	0.20	0.13	28.03

substances (i.e., Na_2O , $(\text{SiO}_2)_L$, SiO_2 , Al_2O_3 , and CaO), a total of five input nodes were considered referring to the molar fraction computed according to equation (2). Thus, the sum of the input value always provides 1. A ternary diagram which displays the proportion of *three-by-three* selected variables (from Table 4) using centroid coordinates is shown in Figure 5. The coordinate axes of such a diagram reported in the x -, y -, and z -axes were scaled so that $0 \leq x$; y ; $z \leq 1$. In order to achieve all the possible combinations, five graphs were plotted (see Figures 5(a)–5(e)), and the constant value was assumed to be the compressive strength (see Output in Table 1) defined in five ranges as follows:

- (i) 1 means $0 \leq \text{compressive strength } (f_c) \leq 10 \text{ MPa}$
- (ii) 2 means $10 < \text{compressive strength } (f_c) \leq 20 \text{ MPa}$
- (iii) 3 means $20 < \text{compressive strength } (f_c) \leq 30 \text{ MPa}$
- (iv) 4 means $30 < \text{compressive strength } (f_c) \leq 40 \text{ MPa}$
- (v) 5 means $40 < \text{compressive strength } (f_c) \leq 50 \text{ MPa}$

$$i_n = \frac{y_m}{y_t}, \quad (2)$$

It was found that in case of combinations illustrated in Figures 5(d) and 5(e), nonsensitivity with respect to the compressive strength was detected. Contrarily, the percentage of Na_2O , SiO_2 , and Al_2O_3 was dominant in the combinations illustrated in Figures 5(a)–5(c), respectively. Definitely, the relationship between the molar composition and the compressive strength of the geopolymer (f_c) is not robust because very small modification of the molar fraction implies a large variation of the relative compressive strength. For this reason, a predictive model assumes a crucial role because the manufacturing of FA-based matrices may produce large differences in their compressive strength depending on the type and the amount of the raw burned material. where i_n is the generic input; $n = 1, \dots, 5$; y_m is the molar quantity of the j -substance; and y_t is the total molar quantity.

The R-code was used for the ANN-model definition [55]. Many models were set by varying the architecture and the minimum average scatter with respect to the experimental finding was met by the proposal illustrated in Figure 6 (with the relative legend). In particular, it was set as follows:

- (i) One input layer with 5 nodes
- (ii) One hidden layer with 10 nodes
- (iii) One output layer with 1 node where f_c is attended

$$h_k = b_k + \sum_{n=1}^{k=10} x_n \cdot w_{kn}, \quad (3)$$

So, summing up, the ANN proposed model is reported in equations (2)–(5). The weight and bias are summarized in

Tables 5 and 6 for the different ANN layers. The optimized architecture was found by trial and error method for minimizing the experimental versus theoretical scatter. No input normalization was computed since the molar fraction is dimensionless. In order to activate the h -neurons, a sigmoidal-shaped activation function (namely, activation) was selected as reported in equation (4). While an identity function was imposed for the activation of the output node (see Figure 6), sum functions were also needed in the hidden and output layers in order to process the additives (*weight and bias*), i.e., equations (3) and (5), respectively. The “*trial and error method*” was used by considering 1/3 and 2/3 of the database for the training and the learning phases, respectively. where $k = 1, \dots, 10$, according to Table 5, and $n = 1, \dots, 5$, according to Table 4 and equation (2).

$$\text{act}(h_k) = \frac{1}{(1 + e^{-h_k})}, \quad (4)$$

$$f_c = o = B + \sum_{n=1}^{n=5} x_n \cdot w_j + \sum_{k=1}^{k=10} \text{act}(h_k) \cdot w_j, \quad (5)$$

where $n = 1, \dots, 5$, according to Table 4 and equation (2), $k = 1, \dots, 10$, according to Table 5, $j = 1, \dots, 15$, according to Table 6, and B , according to Table 6.

Obviously, the mixture proportions have significant influence on the fresh and hardened properties of the mortars. In other words, the amount of sand, coarse aggregate, and water-to-cement ratio can affect the compressive strength. In our study, the values of these factors have been fixed. Therefore, the results of the ANN modelling can only be valid for the condition under which the models have been developed.

6. ANN Model Evaluation

The proposed ANN model allows predicting the compressive strength of the considered geopolymer-based mortar. The sample-by-sample comparison is reported in Figure 7 by reporting both the actual (or experimental) and predicted (or theoretical) outcomes. It can be seen that the ANN model significantly overestimates the relative experimental data only for sample number 39, i.e., *30S12M1.5*, while a satisfactory prediction was reached in all the other cases. Moreover, a correlation index (R^2) equal to 0.89 was obtained as illustrated in Figure 8. In addition, the 25% scatter area was plotted demonstrating that almost all the predictions are within it. It can be noticed that the trend line of the

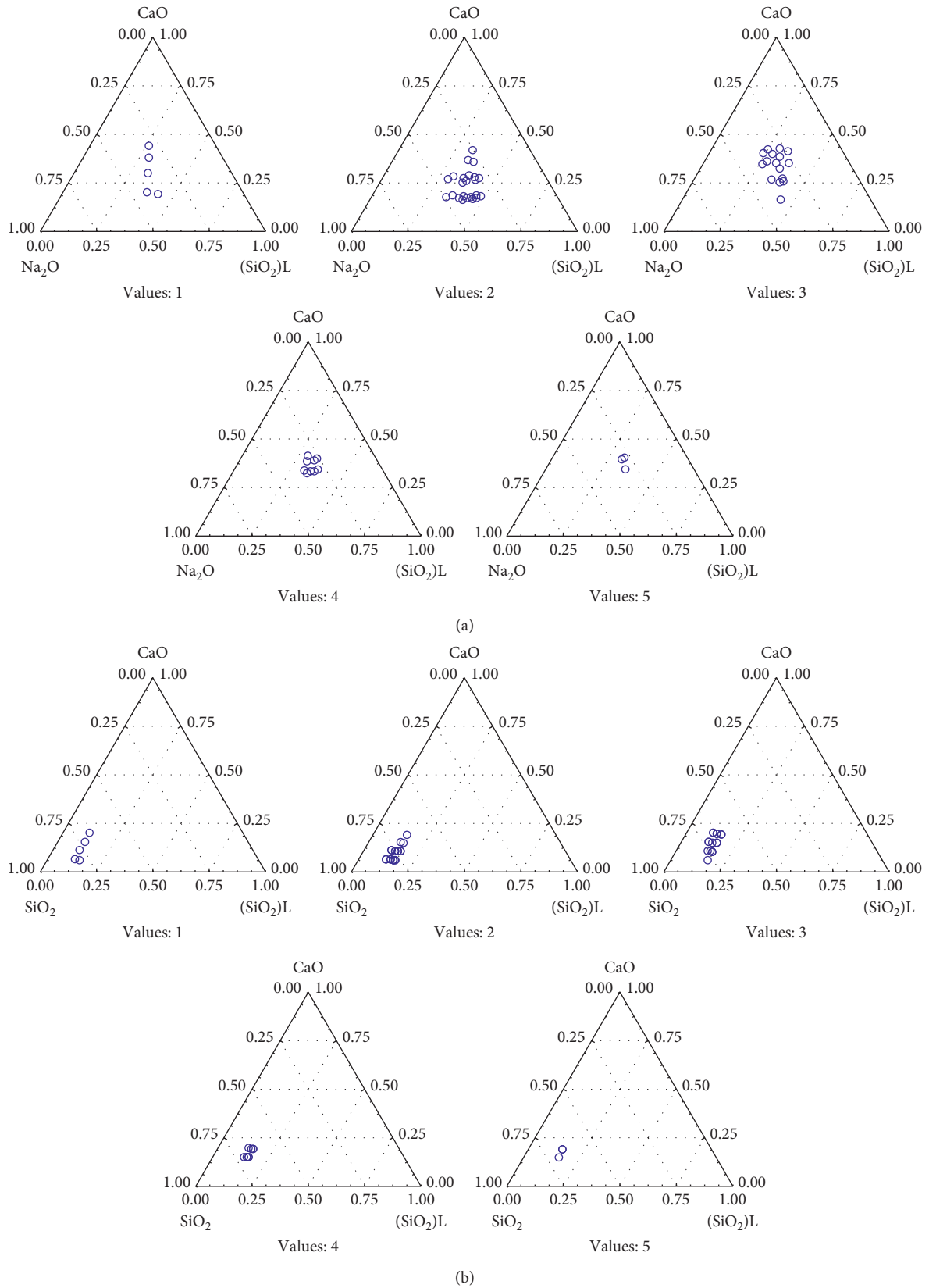
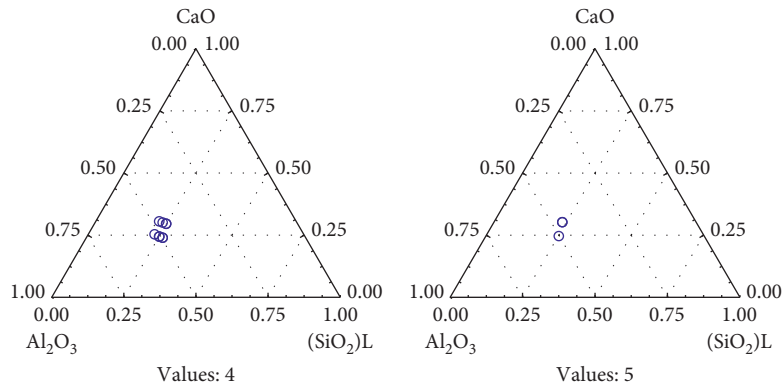
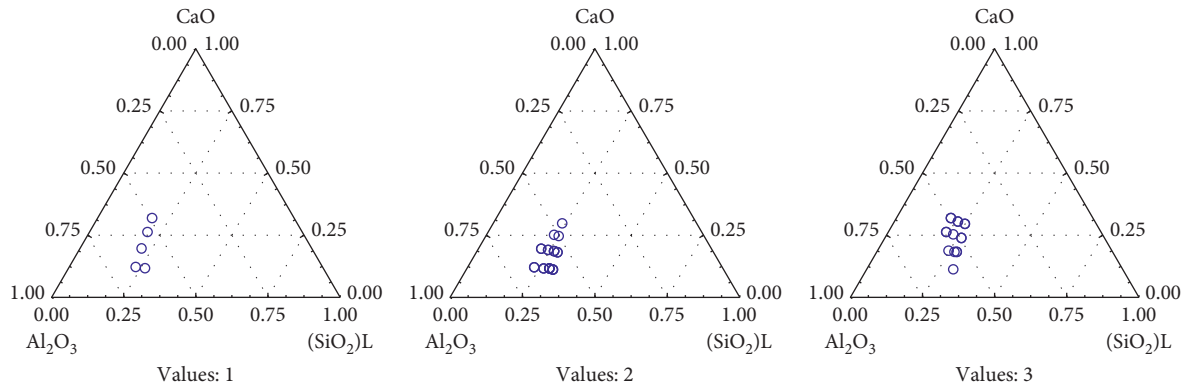
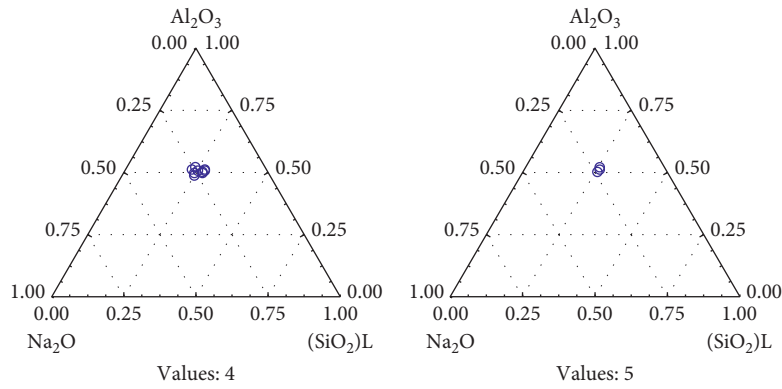
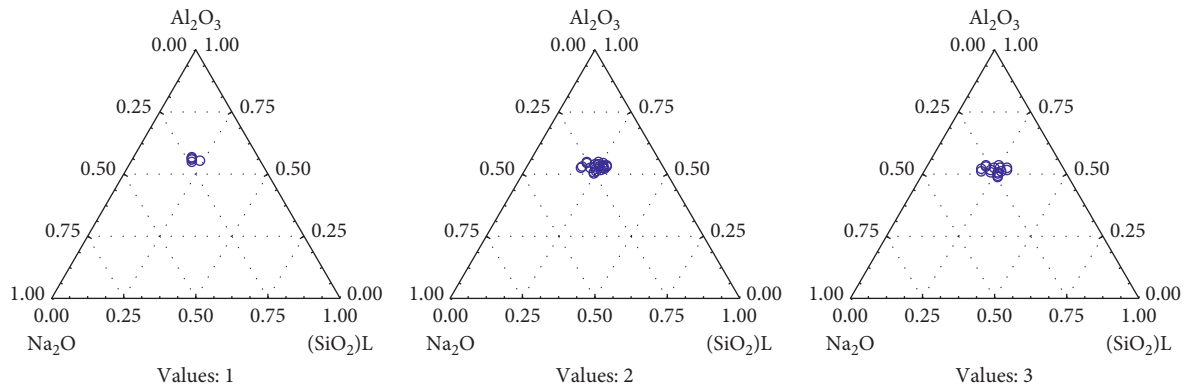


FIGURE 5: Continued.



(c)



(d)

FIGURE 5: Continued.

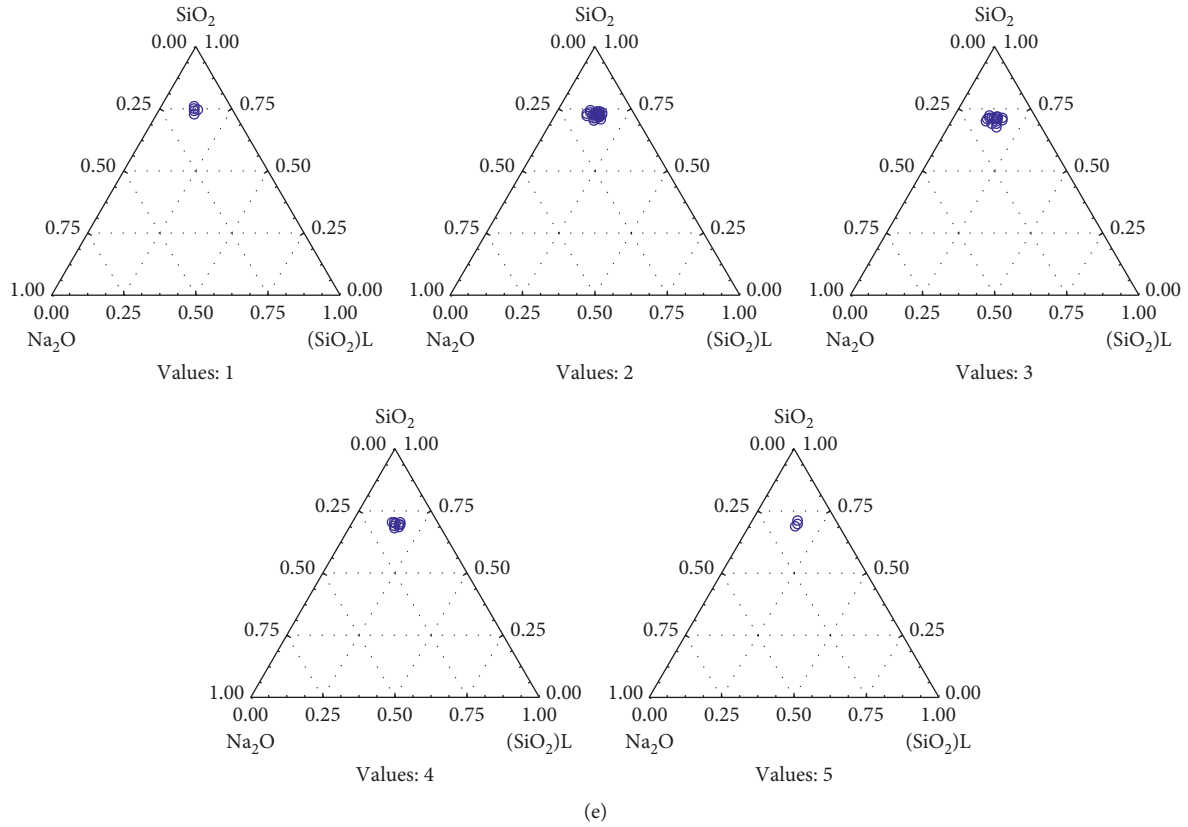


FIGURE 5: Ternary plot of the molar composition with respect to the compressive strength (values: 1 = 0–10 MPa; 2 = 10–20 MPa; 3 = 20–30 MPa; 4 = 30–40 MPa; 5 = 40–50 MPa).

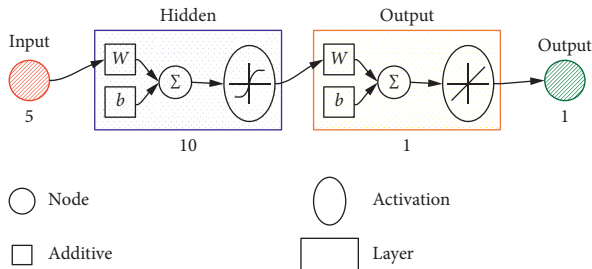


FIGURE 6: Architecture of the proposed ANN model.

TABLE 5: Weight matrix and bias vector of the hidden layer.

Label	Weight (w_{kn})						Bias (b_k)
h_1	387.62	74.34	-148.41	-86.69	-157.70	69.33	
h_2	3.99	7.11	-54.74	-13.79	48.92	-8.28	
h_3	22.18	172.70	-208.02	-60.03	149.32	77.01	
h_4	2.49	2.34	-3.60	0.01	8.52	10.00	
h_5	28.29	38.41	-16.3	-5.49	5.07	48.89	
h_6	-91.99	-21.12	-84.44	1.75	216.12	19.56	
h_7	106.19	240.86	262.65	-89.65	105.64	100.45	
h_8	-3.71	-33.66	6.03	6.45	24.38	-2.31	
h_9	7.45	10.33	-30.81	-4.46	47.17	28.27	
h_{10}	8.27	16.53	-3.63	-2.82	0.27	17.09	

TABLE 6: Weight matrix and bias value of the output layer.

Label	Weight (w_j)	Bias (B)
i_1 to o_1	-21.83	
i_2 to o_1	42.09	
i_3 to o_1	-132.17	
i_4 to o_1	-31.31	
i_5 to o_1	132.33	
h_1 to o_1	65.13	
h_2 to o_1	31.32	
h_3 to o_1	-68.89	-9.51
h_4 to o_1	-4.19	
h_5 to o_1	54.90	
h_6 to o_1	30.28	
h_7 to o_1	62.76	
h_8 to o_1	-11.65	
h_9 to o_1	-24.70	
h_{10} to o_1	6.60	

points in figure (red dots) quite approximates the green line (perfect prediction $x = y$). Finally, the frequency distribution of the ratio between the actual and predicted values is shown in Figure 9. The mean, median, and mode values were 0.991, 0.973, and 0.991, respectively, with a 14% coefficient of variation. Since the mean, median, and mode are so close,

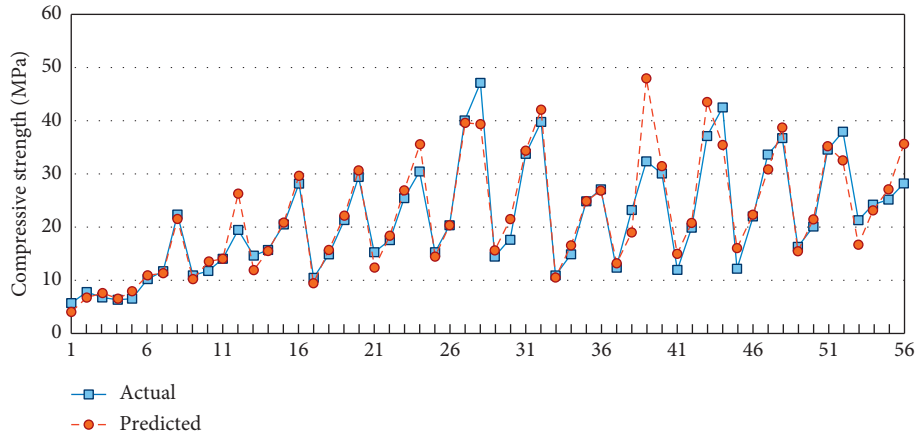


FIGURE 7: Actual vs. predicted values of the geopolymer's cylindrical compressive strength.

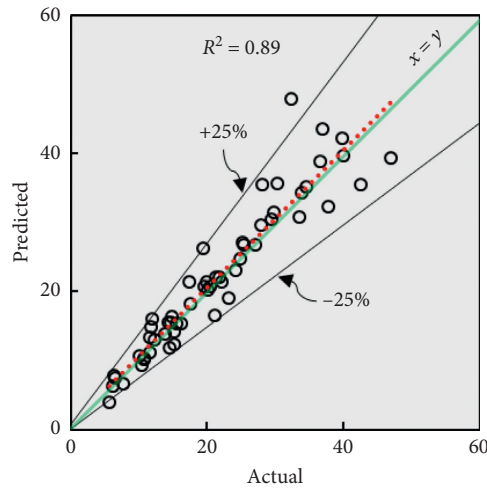


FIGURE 8: Scatter plot of the actual vs. predicted values of the geopolymer's cylindrical compressive strength (MPa).

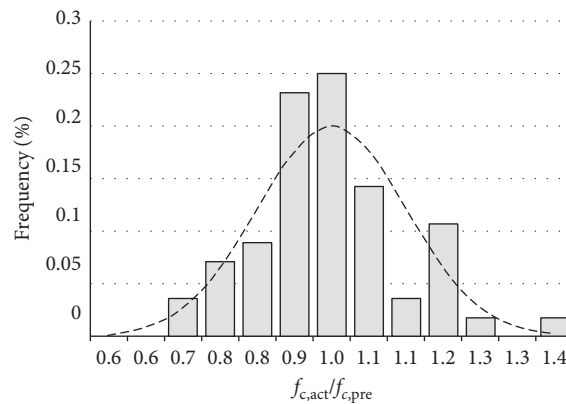


FIGURE 9: Frequency distribution of the actual/predicted values of the geopolymer's cylindrical compressive strength.

the frequency distribution is symmetric, and its axis of symmetry is $x \sim 1$ = perfect prediction. Furthermore, the lower and upper outliers were 0.75 and 1.23, respectively. In fact, only two findings were minor of 0.75 and two were over 1.23.

7. Parametric Analysis

A parametric analysis is reported in Figures 10(a)–10(c) by relating the molar fractions (x - and y -axes) to the compressive strength prediction in MPa (o) on the z -axis

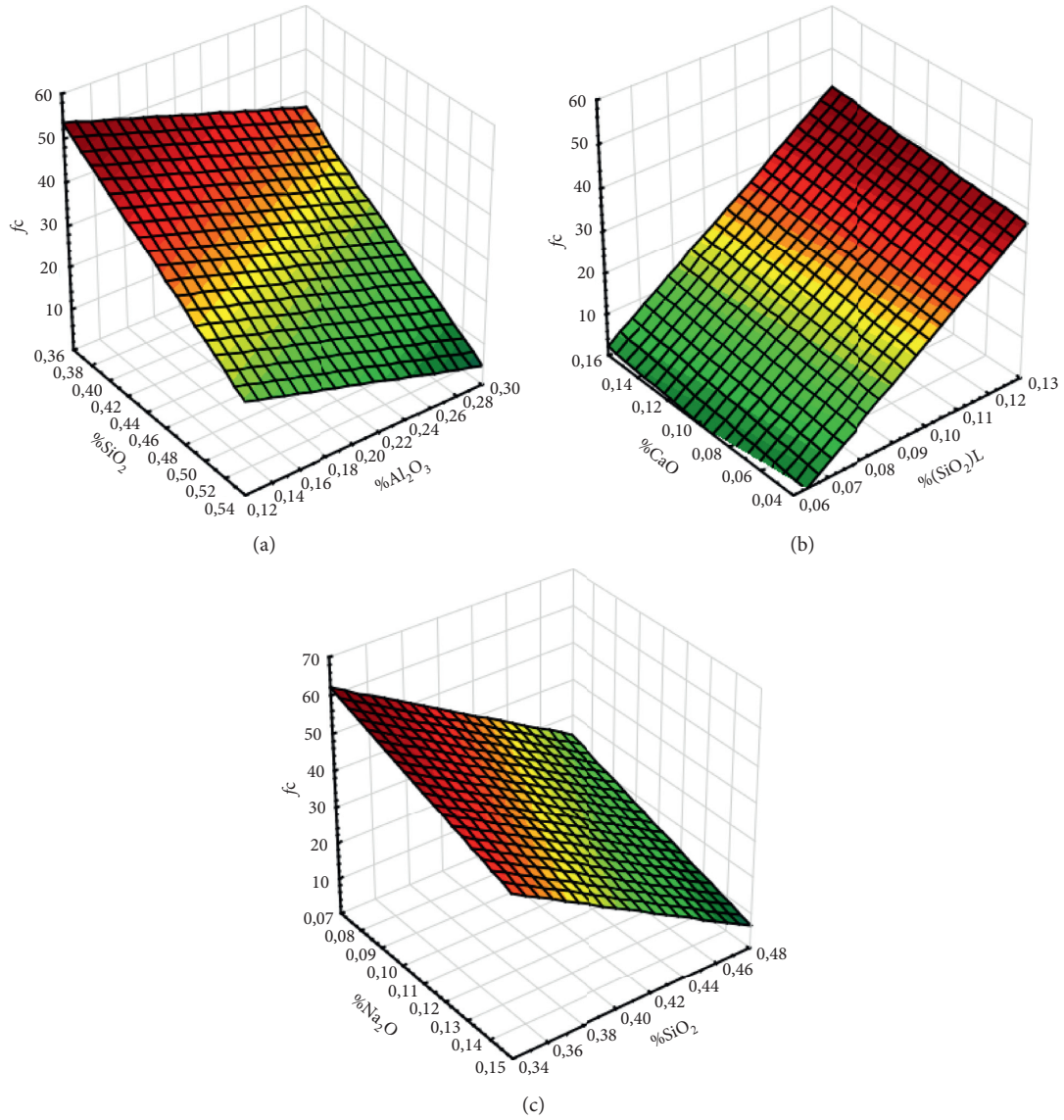


FIGURE 10: 3D surface plot of the molar fractions with respect to the compressive strength: (a) %SiO₂ vs %Al₂O₃; (b) %CaO vs % (SiO₂) L; (c) %Na₂O vs %SiO₂.

TABLE 7: Predicted inputs corresponding to mortar compressive strength $f_c > 80$ MPa.

#	%Na ₂ O	%(SiO ₂)L	%SiO ₂	%Al ₂ O ₃	%CaO	f_c (MPa)
1	0.13	0.11	0.49	0.20	0.07	83.53
2	0.13	0.14	0.52	0.15	0.06	84.69
3	0.11	0.13	0.47	0.24	0.05	82.65
4	0.13	0.12	0.46	0.23	0.05	80.58
5	0.12	0.11	0.46	0.25	0.06	80.88
6	0.13	0.12	0.51	0.15	0.08	82.41
7	0.10	0.14	0.49	0.21	0.06	80.53
8	0.12	0.13	0.49	0.20	0.06	81.16
9	0.12	0.11	0.45	0.26	0.06	80.07
10	0.15	0.12	0.51	0.16	0.06	84.15
11	0.13	0.12	0.50	0.19	0.06	82.86
12	0.15	0.10	0.48	0.20	0.07	83.80
13	0.12	0.13	0.49	0.21	0.06	82.08

TABLE 7: Continued.

#	%Na ₂ O	%(SiO ₂)L	%SiO ₂	%Al ₂ O ₃	%CaO	f_c (MPa)
14	0.12	0.13	0.50	0.19	0.06	83.43
15	0.13	0.12	0.48	0.21	0.06	82.24
16	0.14	0.12	0.50	0.18	0.06	83.74
17	0.13	0.10	0.46	0.25	0.07	80.42
18	0.11	0.14	0.50	0.19	0.07	81.04
19	0.15	0.11	0.50	0.17	0.06	81.50
20	0.14	0.10	0.46	0.23	0.06	84.00

throughout a linear surface interpolation. Within this scope, a database of 1500 possible combination of the five constituents was randomly processed, with a variation range consistent with Table 4 (i.e., $0.10 \pm 11\%$; $0.10 \pm 12\%$; $0.50 \pm 6\%$; $0.22 \pm 3\%$; and $0.09 \pm 39\%$ for i_1 ; i_2 ; i_3 ; i_4 ; and i_5 , resp.). The molar fractions were considered *two-by-two* while the remaining three were assumed constant and equal to the relative average value from Table 4 data. The target was forecasted by means of the proposed ANN model, excluding negative outcomes. The colour maps indicate the value of the theoretical compressive strength. The theoretical trends were found consistent and coherent with the experimental one. Na₂O and SiO₂ were dominant in the mix for reaching high levels of compressive strength, while CaO mostly affected the output when combined with high amount of (SiO₂)L according to Figure 10(b). Furthermore, a compressive strength >80 MPa was computed for the input's combinations reported in Table 7 (20 cases on the total 1500).

8. Conclusions

The present study shows the application of ANN methods to predict the cylindrical compressive strength of fly ash-slag geopolymer mortar varying the molar compositions of SiO₂, Al₂O₃, Na₂O, and CaO, based on an experimental investigation carried out on several mix proportions. A new analytical formula was assessed. Despite the variability of the input parameters, the proposed ANN model presents good precision and accuracy. The satisfying performance of the proposed model was clearly indicated by the mean, median, and mode values of $f_{c,act}/f_{c,pre}$, equal to 0.991, 0.973, and 0.991, respectively, with a 14% coefficient of variation and a correlation value of 0.89, indicating the reliability of the proposed model. Parametric analysis was conducted to evaluate the effect of molar fractions on the compressive strength. Na₂O and SiO₂ were dominant in the mix for reaching greater compressive strength. The influence of CaO is significant when combined with a high amount of SiO₂ in alkaline solution.

The results of the study are valid for the variation ranges of the inputs, herein experimentally found. Further experimental investigations are required for the ANN model validation when different inputs, in terms of chemical composition, are considered.

Data Availability

The data supporting the findings of this study are available within the article.

Conflicts of Interest

The authors declare that they have no conflicts of interest regarding the publication of this paper.

Acknowledgments

This study was executed as a part of the funded project of Research Promotion Scheme-National Doctoral Fellowship (File no. 8-11/RIFD/RPS-NDF/Policy-1/2018-19), All India Council for Technical Education, India.

References

- [1] N. K. Lee, J. G. Jang, and H. K. Lee, "Shrinkage characteristics of alkali-activated fly ash/slag paste and mortar at early ages," *Cement and Concrete Composites*, vol. 53, pp. 239–248, 2014.
- [2] E. J. Guades, "Experimental investigation of the compressive and tensile strengths of geopolymer mortar: the effect of sand/fly ash (S/FA) ratio," *Construction and Building Materials*, vol. 127, pp. 484–493, 2016.
- [3] C. D. Atiş, E. B. Görür, O. Karahan, C. Bilim, S. Ilkentapar, and E. Luga, "Very high strength (120 MPa) class F fly ash geopolymer mortar activated at different NaOH amount, heat curing temperature and heat curing duration," *Construction and Building Materials*, vol. 96, pp. 673–678, 2015.
- [4] F. Xi, S. J. Davis, P. Ciais et al., "Substantial global carbon uptake by cement carbonation," *Nature Geoscience*, vol. 9, no. 12, pp. 880–883, 2016.
- [5] J. L. Provis, "Alkali-activated materials," *Cement and Concrete Research*, vol. 114, pp. 40–48, 2018.
- [6] P. Nath and P. K. Sarker, "Effect of GGBFS on setting, workability and early strength properties of fly ash geopolymer concrete cured in ambient condition," *Construction and Building Materials*, vol. 66, pp. 163–171, 2014.
- [7] A. C. Ayachit, P. Nikam, S. N. Pise, A. D. Shah, and V. H. Pawar, "Mix design of fly ash based geopolymer concrete," *International Journal of Scientific and Research Publications*, vol. 6, pp. 381–385, 2016.
- [8] R. Mustafa, K. N. Shivaprasad, and B. B. Das, "Effect of various additives on the properties of fly ash based geopolymer mortar," *Lecture Notes in Civil Engineering*, vol. 25, pp. 707–715, 2019.
- [9] M. Hojati and A. Radlińska, "Shrinkage and strength development of alkali-activated fly ash-slag binary cements," *Construction and Building Materials*, vol. 150, pp. 808–816, 2017.
- [10] O. G. Rivera, W. R. Long, C. A. Weiss et al., "Effect of elevated temperature on alkali-activated geopolymeric binders compared to portland cement-based binders," *Cement and Concrete Research*, vol. 90, pp. 43–51, 2016.

- [11] F. N. Degirmenci, "Effect of sodium silicate to sodium hydroxide ratios on durability of geopolymer mortars containing natural and artificial pozzolans," *Ceramics-Silikaty*, vol. 61, pp. 340–350, 2017.
- [12] S. J. Chithambaram, S. Kumar, and M. M. Prasad, "Thermo-mechanical characteristics of geopolymer mortar," *Construction and Building Materials*, vol. 213, pp. 100–108, 2020.
- [13] S. K. Saxena, M. Kumar, and N. B. Singh, "Fire resistant properties of alumino silicate geopolymer cement mortars," *Materials Today: Proceedings*, vol. 4, no. 4, pp. 5605–5612, 2017.
- [14] H. Y. Zhang, V. Kodur, B. Wu, L. Cao, and F. Wang, "Thermal behavior and mechanical properties of geopolymer mortar after exposure to elevated temperatures," *Construction and Building Materials*, vol. 109, pp. 17–24, 2016.
- [15] G. Kürklü, "The effect of high temperature on the design of blast furnace slag and coarse fly ash-based geopolymer mortar," *Composites Part B: Engineering*, vol. 92, pp. 9–18, 2016.
- [16] G. Ishwarya, B. Singh, S. Deshwal, and S. K. Bhattacharyya, "Effect of sodium carbonate/sodium silicate activator on the rheology, geopolymerization and strength of fly ash/slag geopolymer pastes," *Cement and Concrete Composites*, vol. 97, pp. 226–238, 2019.
- [17] J. G. Jang, N. K. Lee, and H. K. Lee, "Fresh and hardened properties of alkali-activated fly ash/slag pastes with superplasticizers," *Construction and Building Materials*, vol. 50, pp. 169–176, 2014.
- [18] P. De Silva, S. Hanjitsuwan, and P. Chindaprasirt, "The role of SiO₂ and Al₂O₃ on the properties of geopolymers with and without calcium," *Ceramic Engineering and Science Proceedings*, vol. 34, no. 10, p. 25, 2013.
- [19] M. Rowles and B. O'Connor, "Chemical optimisation of the compressive strength of aluminosilicate geopolymers synthesised by sodium silicate activation of metakaolinite," *Journal of Materials Chemistry*, vol. 13, no. 5, pp. 1161–1165, 2003.
- [20] P. D. Silva, K. Sagoe-Crenstil, and V. Sirivivatnanon, "Kinetics of geopolymerization: role of Al₂O₃ and SiO₂," *Cement and Concrete Research*, vol. 37, no. 4, pp. 512–518, 2007.
- [21] J. A. Labrincha, C. Leonelli, A. Palomo, and P. Chindaprasirt, "Handbook of alkali-activated cements, mortars and concretes," in *Woodhead Publishing Series in Civil and Structural Engineering* Elsevier, Amsterdam, Netherlands, 2015.
- [22] E. Gomaa, S. Sargon, C. Kashosi, and M. ElGawady, "Fresh properties and compressive strength of high calcium alkali activated fly ash mortar," *Journal of King Saud University-Engineering Sciences*, vol. 29, no. 4, pp. 356–364, 2017.
- [23] P. Pavithra, M. S. Reddy, P. Dinakar, H. Rao, B. K. Satpathy, and A. N. Mohanty, "Effect of the Na₂SiO₃/NaOH ratio and NaOH molarity on the synthesis of fly ash-based geopolymer mortar," *Geo-Chicago 2016 GSP*, vol. 272, pp. 336–344, 2016.
- [24] A. B. Malkawi, M. F. Nuruddin, A. Fauzi, H. Almattarneh, and B. S. Mohammed, "Effects of alkaline solution on properties of the HCFA geopolymer mortars," *Procedia Engineering*, vol. 148, pp. 710–717, 2016.
- [25] M. N. S. Hadi, M. Al-azzawi, and T. Yu, "Effects of fly ash characteristics and alkaline activator components on compressive strength of fly ash-based geopolymer mortar," *Construction and Building Materials*, vol. 175, pp. 41–54, 2018.
- [26] S. Samantasinghar and S. P. Singh, "Synthesis of fly ash-GGBS-blended geopolymer composites," *Lecture Notes in Civil Engineering*, vol. 1, pp. 83–91, 2019.
- [27] W.-C. Wang, H.-Y. Wang, and M.-H. Lo, "The fresh and engineering properties of alkali activated slag as a function of fly ash replacement and alkali concentration," *Construction and Building Materials*, vol. 84, pp. 224–229, 2015.
- [28] G. M. Rao and T. D. G. Rao, "Final setting time and compressive strength of fly ash and GGBS-based geopolymer paste and mortar," *Arabian Journal for Science and Engineering*, vol. 40, pp. 3067–3074, 2015.
- [29] M. H. Al-majidi, A. Lampropoulos, A. Cundy, and S. Meikle, "Development of geopolymer mortar under ambient temperature for in situ applications," *Construction and Building Materials*, vol. 120, pp. 198–211, 2016.
- [30] H. Mehdizadeh and E. N. Kani, "Modeling the influence of alkali-activated phosphorus slag cement using statistical design," *Canadian Journal of Civil Engineering*, vol. 45, no. 12, pp. 1073–1083, 2018.
- [31] S. K. John, Y. Nadir, and K. Girija, "Effect of source materials, additives on the mechanical properties and durability of fly ash and fly ash-slag geopolymer mortar: a review," *Construction and Building Materials*, vol. 280, p. 122443, 2021.
- [32] J. S. Tenepalli and D. Neeraja, "Properties of class F fly ash based geopolymer mortar produced with alkaline water," *Journal of Building Engineering*, vol. 19, pp. 42–48, 2018.
- [33] S. Hanjitsuwan, S. Hunpratub, P. Thongbai, S. Maensiri, V. Sata, and P. Chindaprasirt, "Effects of NaOH concentrations on physical and electrical properties of high calcium fly ash geopolymer paste," *Cement and Concrete Composites*, vol. 45, pp. 9–14, 2014.
- [34] T. Phoo-Ngernkham, V. Sata, S. Hanjitsuwan, C. Ridtirud, S. Hatanaka, and P. Chindaprasirt, "High calcium fly ash geopolymer mortar containing Portland cement for use as repair material," *Construction and Building Materials*, vol. 98, pp. 482–488, 2015.
- [35] A. F. Jimenez and A. Palomo, "Composition and microstructure of alkali activated fly ash binder: effect of the activator," *Cement and Concrete Research*, vol. 35, pp. 1984–1992, 2005.
- [36] Bureau of Indian Standard (BIS), *IS 3812:2003 Pulverized Fuel Ash-Specification*, BIS, New Delhi, India, 2003.
- [37] T. V. Madhav, I. B. R. Reddy, V. G. Ghorpade, and S. Jyothirmai, "Compressive strength study of geopolymer mortar using quarry rock dust," *Materials Letters*, vol. 231, pp. 105–108, 2018.
- [38] ASTM C873/C873M-10, *Standard Test Method for Compressive Strength of Concrete Cylinders Cast in Place in Cylindrical Molds*, ASTM International, West Conshohocken, PA, USA, 2010.
- [39] M. Criado, W. Aperador, and I. Sobrados, "Microstructural and mechanical properties of alkali activated Colombian raw materials," *Materials (Basel)*, vol. 9, pp. 1–16, 2016.
- [40] C. K. Yip, G. C. Lukey, and J. S. J. Van Deventer, "The co-existence of geopolymeric gel and calcium silicate hydrate at the early stage of alkaline activation," *Cement and Concrete Research*, vol. 35, no. 9, pp. 1688–1697, 2005.
- [41] G. Görhan and G. Kürklü, "The influence of the NaOH solution on the properties of the fly ash-based geopolymer mortar cured at different temperatures," *Composites Part B: Engineering*, vol. 58, pp. 371–377, 2014.
- [42] S. Samantasinghar and S. P. Singh, "Effect of synthesis parameters on compressive strength of fly ash-slag blended geopolymer," *Construction and Building Materials*, vol. 170, pp. 225–234, 2018.

- [43] M. S. Morsy, S. H. Alsayed, Y. Al-Salloum, and T. Almusallam, "Effect of sodium silicate to sodium hydroxide ratios on strength and microstructure of fly ash geopolymer binder," *Arabian Journal for Science and Engineering*, vol. 39, no. 6, pp. 4333–4339, 2014.
- [44] F. Skvara, L. Kopecky, J. Nemecek, and Z. Bittnar, "Microstructure of geopolymer materials based on fly ash," *Ceram-Silikaty*, vol. 50, pp. 208–215, 2006.
- [45] M. Y. Mansour, M. Dicleli, J. Y. Lee, and J. Zhang, "Predicting the shear strength of reinforced concrete beams using artificial neural networks," *Engineering Structures*, vol. 26, no. 6, pp. 781–799, 2004.
- [46] Z. Sterjovski, D. Nolan, K. R. Carpenter, D. P. Dunne, and J. Norrish, "Artificial neural networks for modelling the mechanical properties of steels in various applications," *Journal of Materials Processing Technology*, vol. 170, no. 3, pp. 536–544, 2005.
- [47] A. Cascardi, F. Micelli, and M. A. Aiello, "Analytical model based on artificial neural network for masonry shear walls strengthened with FRM systems," *Composites Part B: Engineering*, vol. 95, 2016.
- [48] A. Cascardi, F. Micelli, and M. A. Aiello, "An Artificial Neural Networks model for the prediction of the compressive strength of FRP-confined concrete circular columns," *Engineering Structures*, vol. 140, pp. 199–208, 2017.
- [49] P. G. Asteris and V. Plevris, "Anisotropic masonry failure criterion using artificial neural networks," *Neural Computing and Applications*, vol. 28, no. 8, 2016.
- [50] V.-L. Tran and S.-E. Kim, "Efficiency of three advanced data-driven models for predicting axial compression capacity of CFDST columns," *Thin-Walled Structures*, vol. 152, p. 106744, 2020.
- [51] F. Demir, "Prediction of elastic modulus of normal and high strength concrete by artificial neural networks," *Construction and Building Materials*, vol. 22, no. 7, pp. 1428–1435, 2008.
- [52] Z. H. Duan, S. C. Kou, and C. S. Poon, "Using artificial neural networks for predicting the elastic modulus of recycled aggregate concrete," *Construction and Building Materials*, vol. 44, pp. 524–532, 2013.
- [53] Z. Duan, C. S. Poon, and J. Xiao, "Using artificial neural networks to assess the applicability of recycled aggregate classification by different specifications," *Materials and Structures*, vol. 50, pp. 1–14, 2017.
- [54] E. M. Golafshani and A. Behnood, "Application of soft computing methods for predicting the elastic modulus of recycled aggregate concrete," *Journal of Cleaner Production*, vol. 176, pp. 1163–1176, 2018.
- [55] B. D. Ripley, "The R project in statistical computing," *MSOR Connections*, vol. 1, no. 1, pp. 23–25, 2001.

Research Article

Study on the Seismic Performance of Small-Diameter Bolts Reinforced in Grottoes

Ningbo Peng ^{1,2}, Bo Sun ^{3,4}, Jizhong Huang ¹, Yun Dong ² and Ye Zhu ²

¹*Institute of Applied Mathematics and Mechanics, Shanghai Key Laboratory of Mechanics in Energy Engineering, School of Mechanics and Engineering Science, Institute for Conservation of Cultural Heritage, Shanghai University, Shanghai 200444, China*

²*Faculty of Architecture and Civil Engineering, Huaiyin Institute of Technology, Huai'an 223001, China*

³*Northwest Research Institute Co. Ltd. of China Railway Engineering Corporation, Lanzhou 730000, China*

⁴*Key Laboratory of Mechanics on Disaster and Environment in Western China, The Ministry of Education of China, School of Civil Engineering and Mechanics, Lanzhou University, Lanzhou 730000, China*

Correspondence should be addressed to Ye Zhu; zhuye1986@hyit.edu.cn

Received 2 February 2021; Accepted 1 March 2021; Published 11 March 2021

Academic Editor: Alessio Cascardi

Copyright © 2021 Ningbo Peng et al. This is an open access article distributed under the Creative Commons Attribution License, which permits unrestricted use, distribution, and reproduction in any medium, provided the original work is properly cited.

The Yungang Grottoes, a World Heritage Site in Datong, consist of 252 caves that are noted for their collection of 5th- and 6th-century Buddhist grotto sculptures and reliefs. Various diseases have appeared in the grottoes under the general influence of natural and artificial factors. Bolt support is a commonly employed method for grotto reinforcement and has been widely applied in many projects. Small-diameter bolts have also been used in the reinforcement projects at the Yungang Grottoes, but the corresponding effect on the seismic performance of grottoes is still unclear. In this paper, a dynamic analysis via the numerical modelling of an ear grotto of the 19th grotto in Yungang is established, and the rock displacement, acceleration, and bolt axial force responses under a seismic wave are analyzed. The results show that the seismic dynamic responses of grottoes are greatly affected by the cliff structure. The displacement and acceleration responses of the cliff body vary greatly within the abrupt transition of the cliff structure. Based on this variation, the seismic capacity of small-diameter bolts in the vertical direction is greater than that in the horizontal direction. The axial force of a bolt is small at both ends of the bolt, large in the middle of the bolt, small on the top of a cliff, and large at the bottom of the cliff. Although the axial force is small, the upper rock mass of the grotto has a tendency to undergo relative movement compared with the outer rock mass. The results also indicate that based on the structural defects in the vertical direction of the cliff body caused by grotto excavation, the inclined angle of the bolt should be increased as far as possible or vertical support should be adopted to enhance the stability of the rock mass at the top of the grotto.

1. Introduction

A grotto cliff body is a special kind of artificial rock slope that is usually dug on the edge of a cliff body. This digging causes cliff bodies to become steep inclined slopes with large inclined angles that are nearly vertical to the ground. As investigated, grottoes have irregular shapes and a variety of statues [1]. After years of weathering and human destruction, cracks have appeared in rock masses of grottoes, which tend to produce more diseases [2–4].

Investigation shows that the collapse and destruction of numerous grottoes are related to earthquakes, especially in

areas with strong seismic activity. Historically, grotto temples, as permanent cultural relics, are always at the risk of earthquakes. As recorded, nearly 70% of grotto temples in China were destroyed because of their location in high-intensity and earthquake-prone areas [1]. For example, the Tiantishan Grottoes in Wuwei, Gansu Province, China, were seriously damaged in the Wuwei Earthquake (1927), which caused the collapse and irreversible destruction of numerous grottoes, while the nearby unexcavated mountain did not experience major damage, and no large cracks appeared. The overall situation is still being mitigated. This case shows that the existence of the grottoes has a substantial impact on the

stability of the mountain structure, and the destruction of the grottoes by the earthquake is disastrous. Therefore, an investigation of the seismic safety of grottoes is critical to reduce the impact of earthquake disasters.

Anchoring can strengthen and reinforce the weak or broken rock and soil mass with materials that have relatively large stiffness; it substantially improves the self-stability of the rock and soil mass, which stabilizes the engineering structure [5, 6]. Bolts have been widely applied in rock and soil mass support engineering, including grottoes [7]. Many research achievements on bolt seismic reinforcement have been made, but most of them were developed by analyzing the slope, underground chamber, and tunnel reinforcement engineering. These previous studies cannot fully illustrate the seismic mechanism of grottoes because these rock heritages are more unstable than the slope and more open than the underground chamber; they also have more dimensions and characteristics than tunnels. Logically, the seismic analysis of grottoes is quite different from that of slopes, underground chambers, and tunnels.

In the reinforcement and protection project of the Yungang Grottoes, small full-length bonded bolts have been installed in many spots. Practically, small-diameter bolts can improve the integrity of fractured rock mass and cause few disturbances to the cultural relic body. However, an evaluation system or method for the aseismic effect of a small anchor on the grotto rock is lacking. To explore the aseismic effect on the cliff bodies of grottoes, the ear grotto of the 19th grotto in Yungang was adopted as a research target, in which a numerical model of grottoes and anchoring were established. By this study, the seismic effect and principle of reinforcing rock grottoes with small bolts are analyzed by numerical calculation under dynamic action.

2. Rock Slope Analysis Model

2.1. Grotto Overview. The Yungang Grottoes in Datong city, Shanxi Province, represent the outstanding achievement of Buddhist art in China in the 5th and 6th century, with 252 caves and 51,000 statues. The Yungang Grottoes, Mogao Grottoes in Dunhuang, and Longmen Grottoes in Luoyang are known as China's three largest ancient grottoes; they are famous as world cultural heritages. Under the action of long-term natural forces, the surrounding rock of these grottoes has suffered numerous serious geological diseases [8–10].

The total protection area of the Yungang Grottoes is approximately 3.6 km², with the Shili River in the south and low hills in the north. The geographical terrain of the grottoes is slightly undulating, with a maximum height difference of approximately 55 m. The geomorphologic types of the grottoes can be generally divided into two forms: a high platform structure with denudation in the low hills at the top of the Yungang Grottoes and valley erosion accumulation on the terrace of the Shili River [11]. The grotto rock mass has moderate softness and hardness, which is suitable for carving, but has poor resistance to weathering. The composition of the 19th grotto consists of grayish-white medium sandstone on the top of the grotto with a distribution between 4 and 5 m; medium sand and fine sandstone

with mudstone and sandy mudstone in the interlayer with a distribution between 5 and 10 m; and light brown and grayish-white medium sand and fine sandstone 10 m above the grotto [12, 13]. The geological section of the grotto cliff body is shown in Figure 1. To obtain the calculation parameters of the rock mass that occurs in the grottoes, four types of rocks were taken from the same stratum of the mountain near the grottoes (Figure 2(a)), and the rocks were cut into samples for test (Figure 2(b)). The physical and mechanical parameters of the rock mass were obtained by experiments (Figures 2(c) and 2(d)). The parameters of the rock mass that occurs in the grottoes are shown in Table 1.

The 19th grotto of the Yungang Grottoes is one of the most representative grottoes at the research site. The main cave is oval in shape, with a vault roof, a door, and clear windows. The height of the seated Buddha in the main cave is 16.8 m, and it is the second highest statue in the Yungang Grottoes. One ear grotto is cut approximately 5 m from the ground to the east and west of the grotto, in which a sitting statue with a height of 8 m is carved. The research object of this paper is the west ear grottoes and their cliff bodies, as shown in Figure 3(a). After an earthquake, the fore wall of the 20th grotto and the west ear grotto of the 19th grotto collapsed. Part of the cave wall between the ear grotto and the main grotto is relatively thin, and there is a broken hole on the cave wall, as shown in Figure 3(b). The thinnest part is less than 10 cm; the cause of this damage is unknown.

2.2. Calculation Model and Boundary Conditions. In previous research, the time-history analysis of the seismic dynamics of the grottoes' cliff bodies is relatively rare. Grottoes are usually reduced to regular caves, while the statues in grottoes are large in size and irregular in shape, which affect the stress distribution of their cliff bodies. The geometries of the grottoes may have greater influence on the dynamic response under dynamic action. Therefore, the shapes of the statues in the grottoes should not be disregarded in the dynamic response analysis of the grottoes' cliff bodies, and the morphologies of the grottoes should be reflected in the model for better observation or modelling. The three-dimensional model of the grottoes' cliff bodies is established, and the three-dimensional point cloud of the facade and the inner main grotto walls of the grottoes' cliff bodies are obtained. The finite element software ANSYS is employed for auxiliary modelling, and the model is imported into FLAC3D for calculation. The built model is shown in Figure 4(a). The total height of the model is 29.25 m; the east-west (X -axis direction) width is 12.12 m; the north-south (Y -axis direction) length is 20 m; and the model has 48,029 nodes and 255,463 units. Because the cracks in the grottoes' cliff bodies have been treated by grouting, the influence of cracks is not considered in this model.

2.3. Anchorage Design and Calculation Parameters. Small bolts are applied to reinforce the upper rock mass of the ear grottoes, as shown in Figure 4(b). A full-length bonded bolt is adopted for support: the length of the bolt $l=7$ m; transverse and vertical spacing $D=2$ m; angle $=10^\circ$; bolt

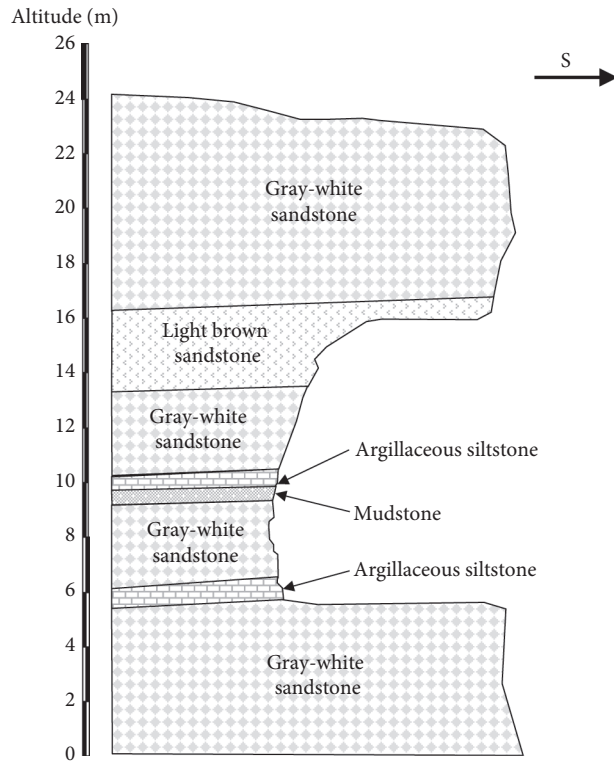


FIGURE 1: Typical geological section profile of the study area.



FIGURE 2: Rock mechanics experiment: (a) primary sample, (b) sample cutting, (c) rock shear test, and (d) uniaxial compression experiment.

diameter $r = 12$ mm; and design load is 40 kN. From the left boundary of the model, a row of bolts was installed with an interval of 2 m, 5 vertical rows, 4 bolts in each row, and a

total of 20 small bolts. For the convenience of analysis, 5 rows of bolts were numbered as groups X1 to X5 from left to right along the x -axis. From low to high along the elevation

TABLE 1: Physical and mechanical parameters of the rock mass in the grottoes.

Rock type	Density ($\text{g}\cdot\text{cm}^{-3}$)	Elasticity modulus (GPa)	Poisson's ratio	Cohesion (MPa)	Internal friction angle ($^{\circ}$)	Tensile strength (MPa)
Gray-white sandstone	2.16	27.90	0.198	1.0	30.45	5.39
Light brown sandstone	2.55	23.70	0.144	0.8	32.13	1.25
Argillaceous siltstone	1.79	13.39	0.298	0.5	14.07	0.01
Mudstone	1.71	8.29	0.280	0.3	13.13	0.02

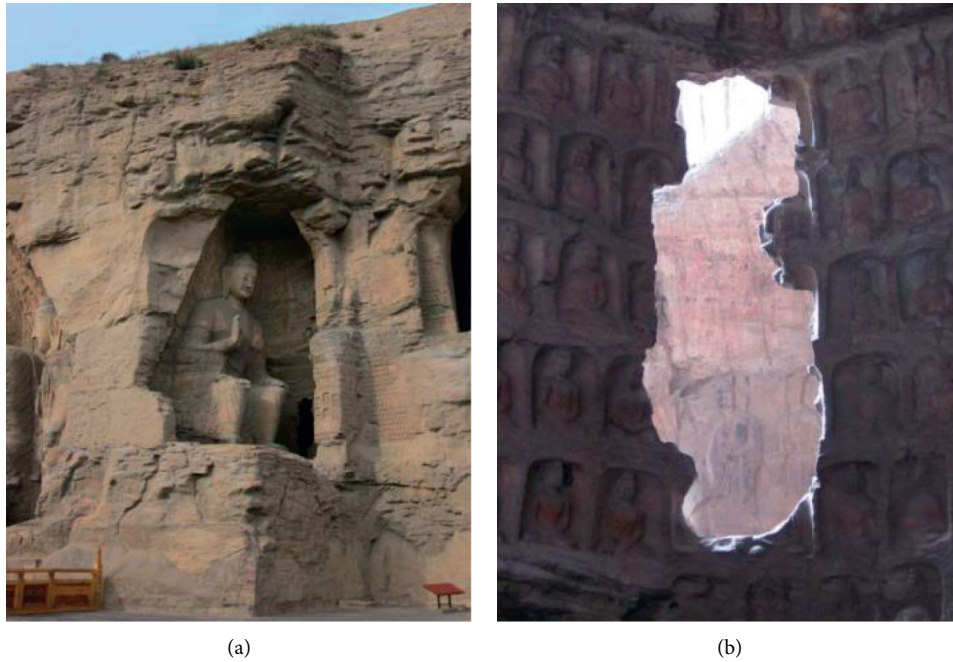


FIGURE 3: (a) Western ear grotto of the 19th grotto in Yungang. (b) Damage to the thin wall between the ear grotto and the main grotto.

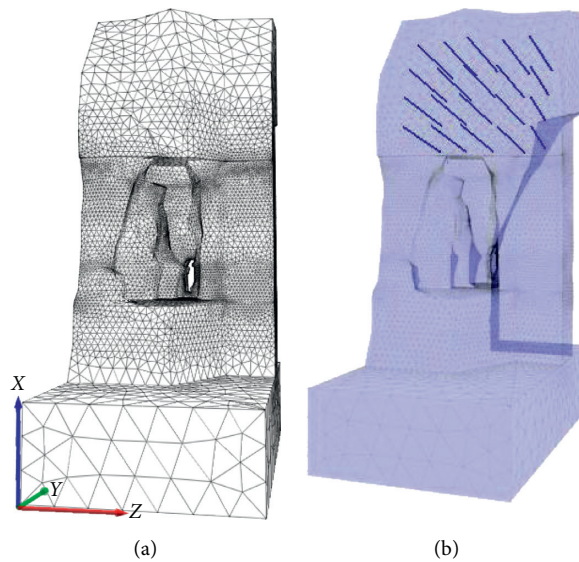


FIGURE 4: Numerical model: (a) numerical model of the unanchored grotto and mesh generation; (b) schematic of bolt support design.

direction, the bolts were numbered as groups Z1 to Z4. According to the position, the bolts could be numbered as group XZ, in which X and Z represent the x -direction of the bolts and the z -direction of the bolts, respectively.

2.4. Cable Structural Elements. Structural units provided for anchor/cable simulation in FLAC3D include Cable and Pile [14]. The axial stress of the small bolt, which has a small diameter and a weak bending resistance, is considered. Therefore, a cable is chosen to simulate the anchor rod within the research. Each cable structural element is defined by its geometric, material, and grout properties. CableSEL is assumed to be a straight segment of uniform cross-sectional and material properties that is located between two nodal points. An arbitrarily curved structural cable can be modeled as a curvilinear structure that is composed of a collection of cableSELS. CableSEL behaves as an elastic-perfectly plastic material that can yield in tension and compression but cannot resist a bending moment.

Each cableSEL has a unique coordinate system, as shown in Figure 5, to define the average axial cable direction. The cableSEL coordinate system is defined by the locations of its two nodal points, which are labeled 1 and 2. The cableSEL coordinate system is defined as follows:

- (1) The centroidal axis coincides with the x -axis
- (2) The x -axis is directed from node 1 to node 2
- (3) The y -axis is aligned with the projection of the global y - or x -direction (whichever is not parallel with the local x -axis) onto the cross-sectional plane

The two active degrees of freedom of the cable finite element are shown in Figure 5. For each axial displacement shown in the figure, there is a corresponding axial force. The stiffness matrix of the cable finite element includes a single degree of freedom at each node, which represents axial action within a cable structure.

Naturally, the shear behavior of the cable-rock interface is cohesive and frictional. Within this model, the system is conceptualized and represented numerically as a spring-slider system that is located at the nodal points along the cable axis. In evaluating the axial forces that develop in the reinforcement, displacements are computed at the nodal points along the reinforcement axis, as shown in Figure 6. Out-of-balance forces at each node are computed from the axial force in the reinforcement, and the shear forces contributed via the shear interaction along the grout annulus. Axial displacements are computed by integrating the nodal accelerations using the out-of-balance axial force and a mass that is lumped at each node.

In the calculation of anchoring, the grotto model without anchoring is analyzed, and the boundary conditions of dynamic-static force, monitoring point setting, and input seismic waves remain the same as the original model. Only the bolt element is added to the upper rock mass of the original model. The material parameters of the small bolt in the model are shown in Table 2.

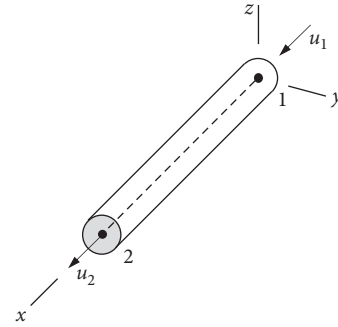


FIGURE 5: CableSEL coordinate system and 2 active degrees of freedom of the cable finite element.

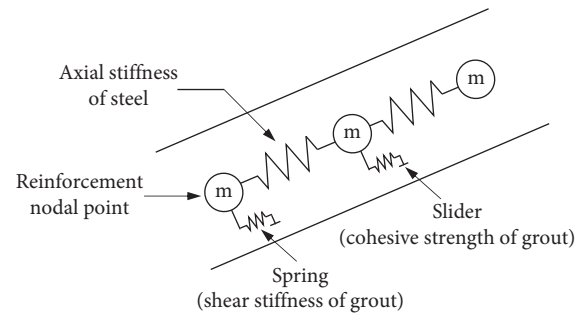


FIGURE 6: Mechanical representation of fully bonded reinforcement.

2.5. Boundary Conditions and Seismic Waves. Numerical analysis of the seismic response of surface structures, such as dams, requires the discretization of a region of the material adjacent to the foundation. The seismic input is normally represented by plane waves that propagate upward through the underlying material. The boundary conditions at the sides of the model must be accounted for in the free-field motion that exists in the absence of the structure. These boundaries need to be placed at distances that are sufficient for minimizing the wave reflections and achieving free-field conditions. To apply the free-field boundary in FLAC3D (Figure 7), the model should be oriented such that the base is horizontal, its normal is in the direction of the z -axis, the sides are vertical, and their normals are in the direction of either the x - or y -axis.

The Kobe seismic wave with a maximum positive acceleration of 2 m/s^2 is selected as the input seismic wave in the calculation of the seismic force within the grotto cliff body. The duration of the seismic wave is 18 s, and the preeminent frequency range is 1–3 Hz. The input direction is positive in the y -axis. The time-history curve of acceleration is shown in Figure 8.

2.6. Monitoring Stations. To facilitate the subsequent analysis and generate the final calculation results, monitoring points were established before processing the calculation. The distribution of the monitoring points is shown in Figure 9. A total of 38 monitoring points in three groups—E1–E12, M1–M14, and W1–W12—were set up along the

TABLE 2: Material parameters of the small bolt.

Modulus of elasticity (GPa)	Yield load (kN)	Bond stiffness (N/m ²)	Bond strength (N/m)	Anchor bar diameter (mm)	Anchor hole diameter (mm)
200	300	1.0×10^9	2×10^8	12	30

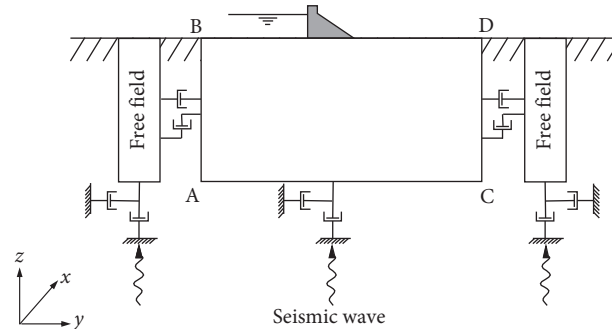


FIGURE 7: Model for seismic analysis of surface structures and free-field mesh.

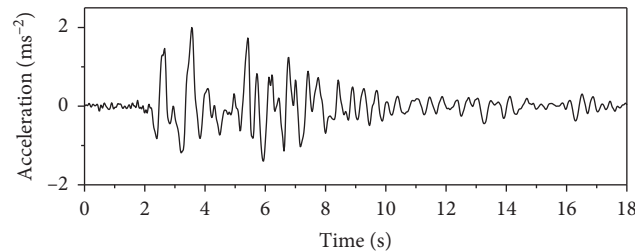


FIGURE 8: Input seismic wave of the model.

elevation at different x -coordinates of the model facade, as shown in Figure 9(a). A group of 12 monitoring points were set up along the elevation of the inner wall of the model, namely, the wall of the main grotto, as shown in Figure 9(b).

3. Analysis Results

3.1. Displacement Response. To analyze the influence of the small bolt support on the horizontal seismic permanent displacements of grottoes, the y -direction relative displacement-time history curve of the small bolt support is compared with the bolt-free support of the grotto cliff body at some monitoring points (consider group M's monitoring points as an example), as shown in Figure 10(a).

On the position of different monitoring points, the final horizontal displacement of the anchored cliff is larger than that of the unanchored cliff, as shown in Figures 10(b)–10(d). For monitoring point M9 (Figure 10(c)), where the difference in the displacement between the two points is relatively large, the final horizontal relative displacement of the unanchored cliff body is -29.57 mm and the anchored cliff body is -29.95 mm. After anchoring, the horizontal relative displacement of the cliff body increases by 0.38 mm, which is approximately 1.29% ; this increase can be considered negligible.

Under the support of small bolts, the horizontal displacement of the seismic response of the grotto cliff body

increases slightly because of the difference in the seismic wave propagation caused by the improvement in the integrity by anchoring the rock mass. The difference between the anchored rock mass and the unanchored rock mass is almost negligible; the support of small bolts has almost no influence on the y -direction displacement response of the grottoes under the action of earthquake. This finding indicates that the small bolts have no clear function in reducing the permanent displacement of the cliff body in the horizontal direction.

Although only the axial force is considered in the calculation process of the cable unit, there is a certain angle between the anchor bolt and the horizontal displacement with a reflection of the effect on the vertical displacement of the cliff body. To analyze the effect of the bolt support on the settlement of grottoes in the z -direction, the uneven settlement of the rock inside and outside the top of the model is compared before and after anchoring, as shown in Figure 11. For the majority of the seismic action, the settlement value of the anchored cliff is less than that of the unanchored cliff. The largest difference between the anchored cliff and the unanchored cliff occurs when the seismic action lasts for 7.654 s. The uneven settlement of the unanchored cliff body and anchored cliff body is 12.180 mm and 9.437 mm, respectively, which is a reduction of 22.52% . At the end of the seismic action, the uneven settlement of the unanchored cliff and anchored cliff was 32.970 mm and 31.593 mm, which is a

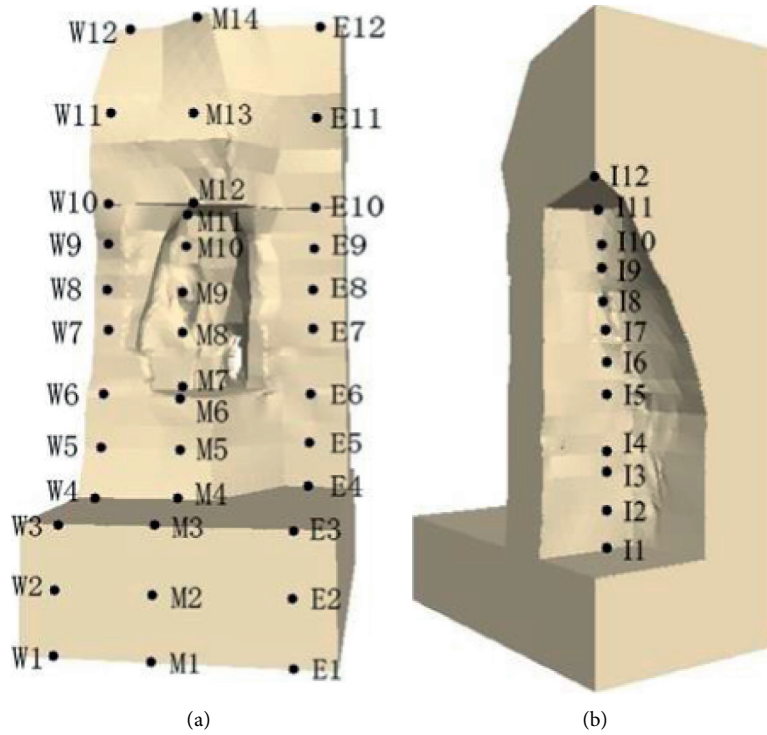


FIGURE 9: Distribution of monitoring points: (a) a total of 38 monitoring points were set up in groups E, M, and W on the model facade; (b) inner wall monitoring points were set up with a group of 12 monitoring points.

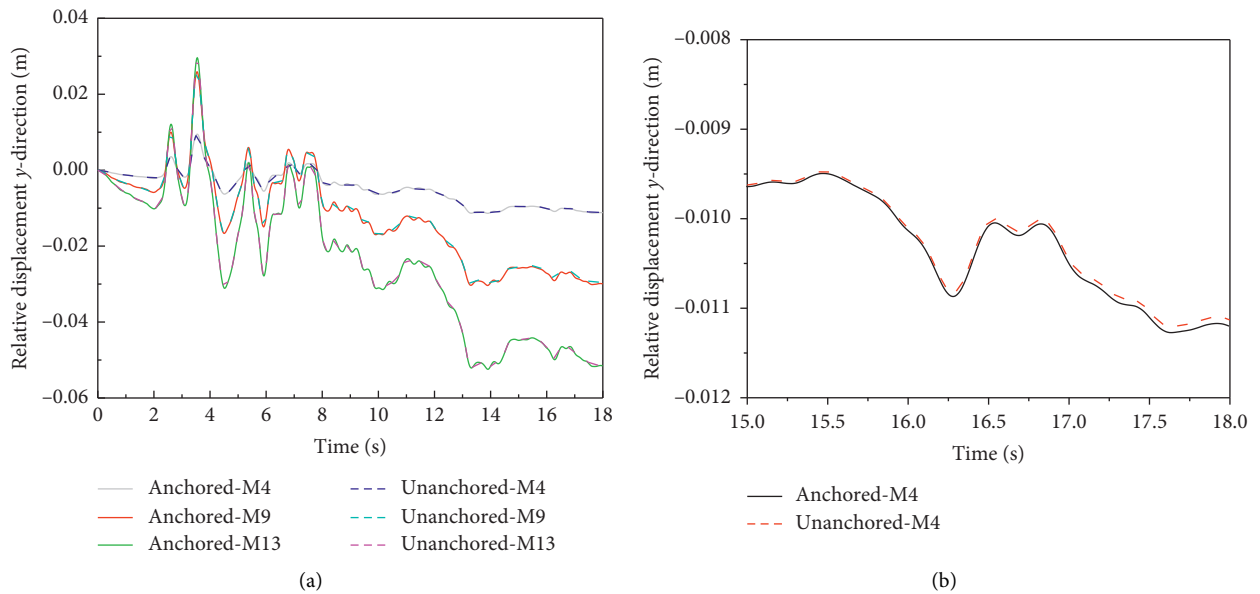


FIGURE 10: Continued.

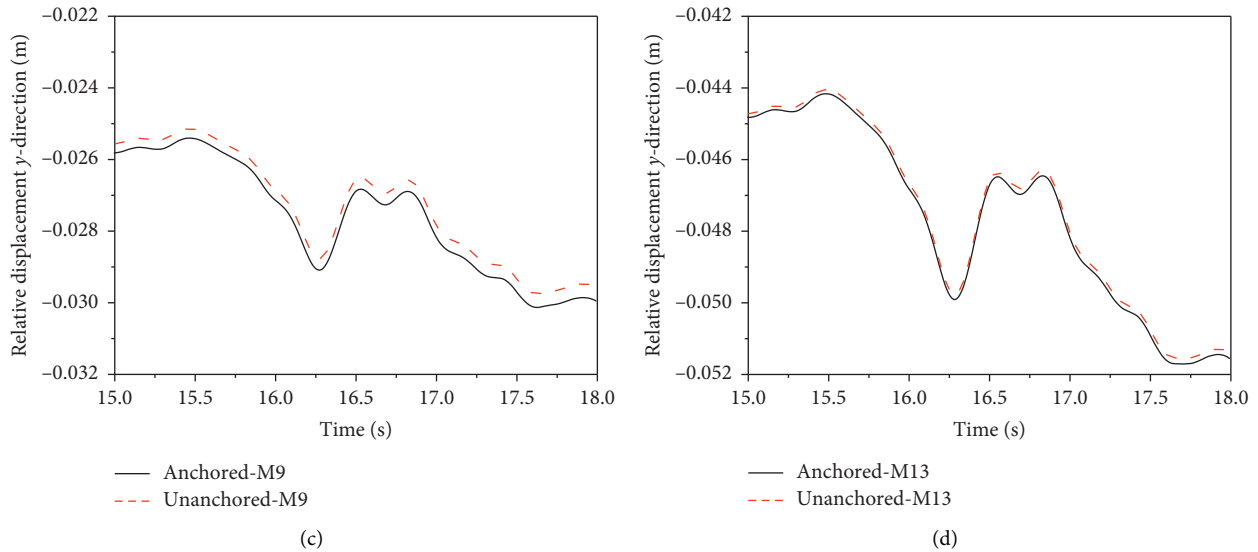


FIGURE 10: Relative displacement in the y -direction of anchorage grottoes: (a) relative horizontal displacement-time history of some monitoring points with and without anchoring; (b) local magnification of relative horizontal displacement-time history at monitoring point M4 with and without anchoring; (c) local magnification of relative horizontal displacement-time history at monitoring point M9 with and without anchoring; (d) local magnification of relative horizontal displacement-time history at monitoring point M13 with and without anchoring.

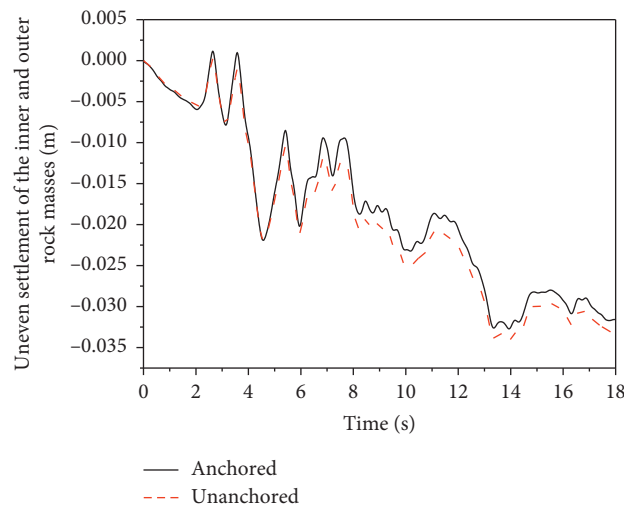


FIGURE 11: Uneven settlement curves of grottoes with and without anchors.

reduction of 1.377 mm or 4.18%. Therefore, for different moments of earthquake action, the effect of the anchor on the uneven settlement of the cliff body is inconsistent. By comparison, the effect of the anchor on the vertical settlement of the grotto is slightly more significant than that of the horizontal displacement of the grotto. However, the seismic effect of the small bolt is still not ideal, with regard to the reduction in the final displacement, because the seismic effect of the small bolt is not fully realized.

3.2. Acceleration Response. Within the dynamic calculation of the slope, the slope surface usually amplifies the effect of

seismic waves. To explore the ground motion response law of the grotto cliff body, the PGA (peak ground acceleration) amplification factor is defined as the ratio between the peak acceleration response of each record point and the peak acceleration response at the bottom of the model. Figure 12 shows the line diagram of the PGA amplification factor, which varies within the elevations of the 4 sets of monitoring points.

The PGA amplification factor of the cliff body shows an initial increasing trend and then a decreasing trend, among which monitoring point M10 was near 130. This trend also presents an order of magnitude that differs from the PGA amplification factor that has been investigated by previous

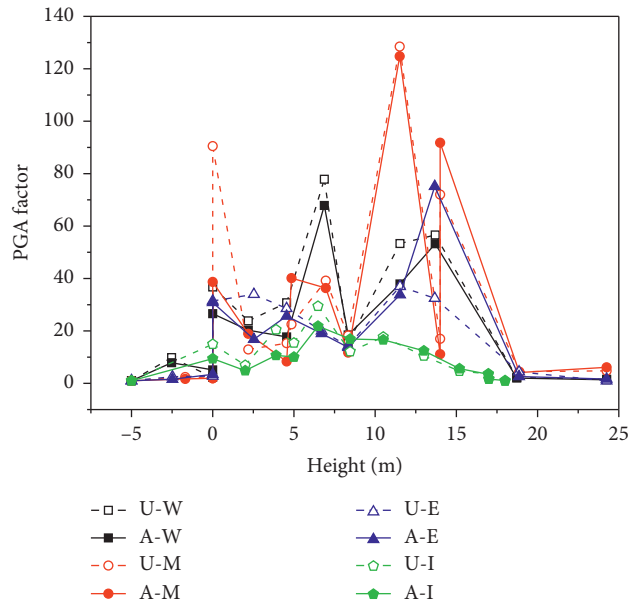


FIGURE 12: PGA amplification factor at different monitoring points of the anchorage and original cliff body.

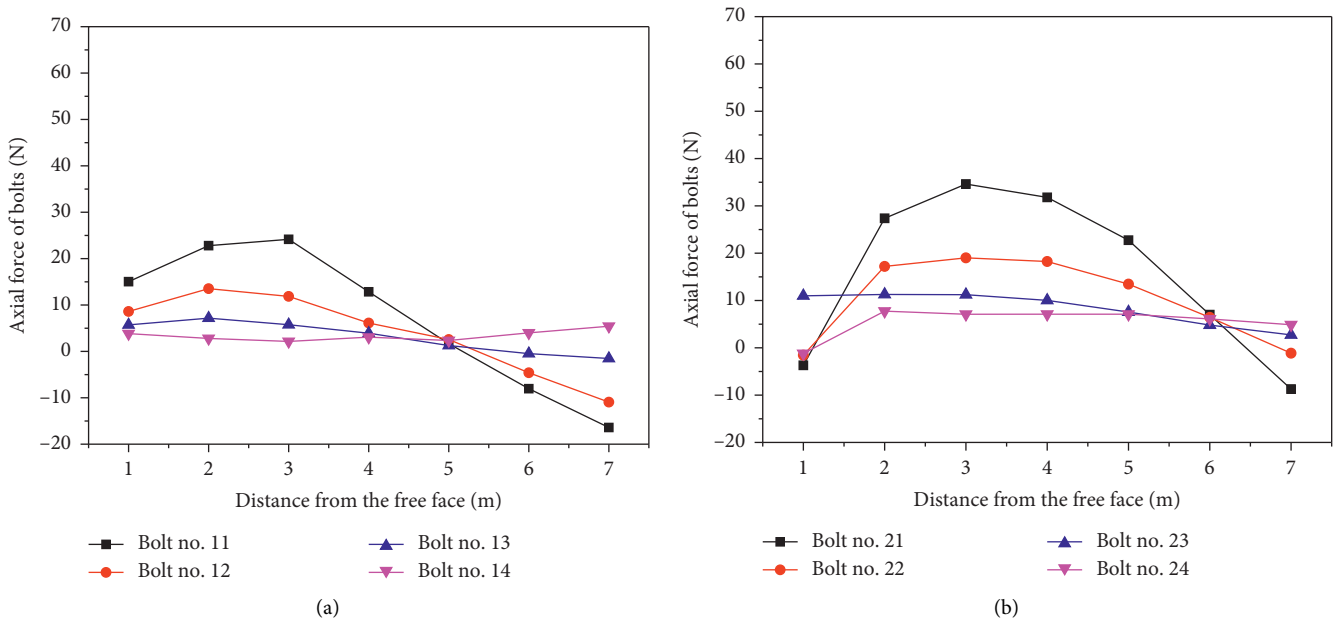


FIGURE 13: Continued.

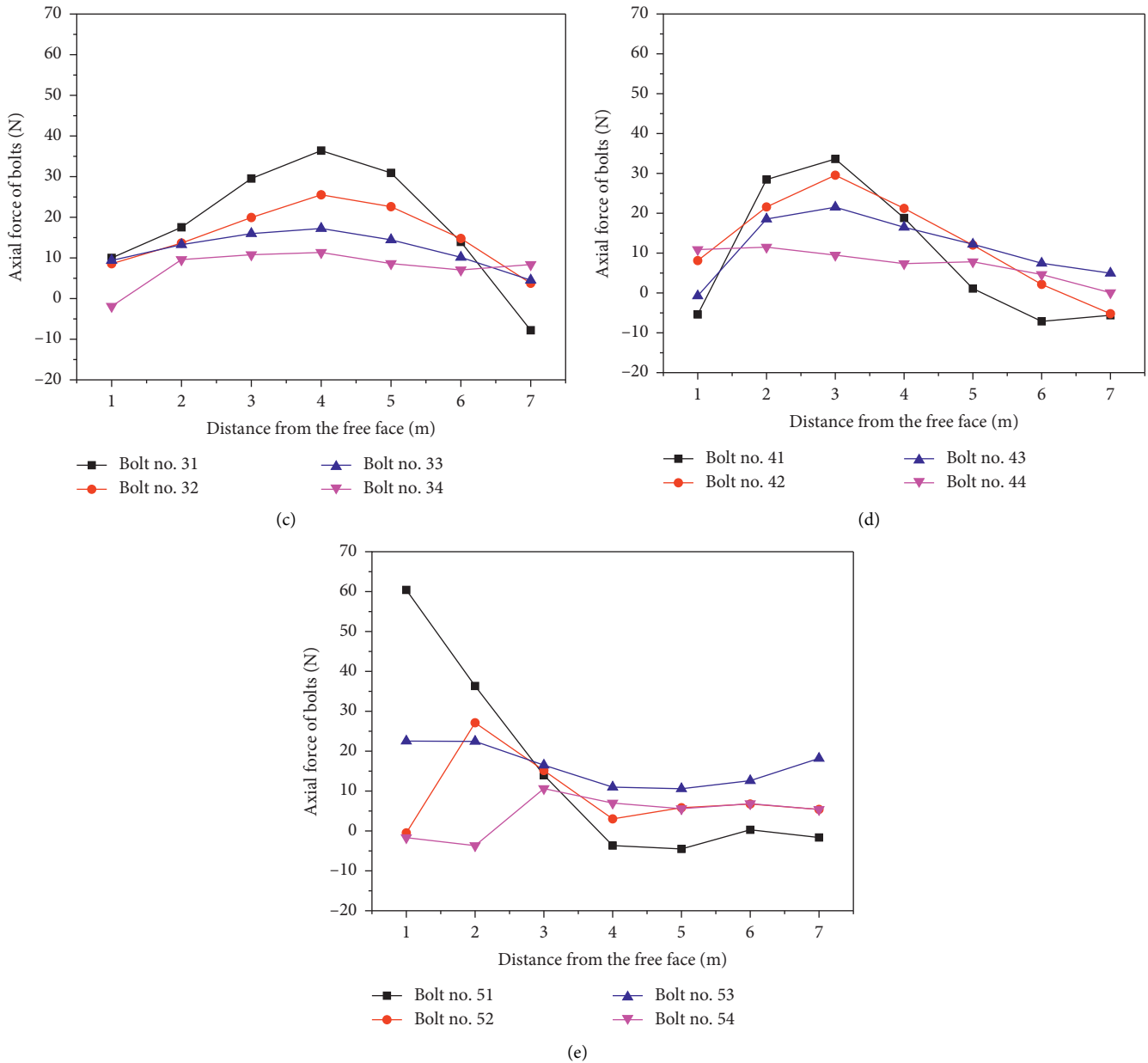


FIGURE 13: Bolt axial force distribution.

scholars in the dynamic response of the slope. The PGA amplification factor does not increase along the elevation; it first increases and then decreases and presents a strong fluctuation. Apparently, the PGA amplification factor of the monitoring point in the elevation area where the ear hole is located is relatively large because the digging makes the rock mass of grottoes have a special geometric structure. The rock mass has two groups of irregular facing surfaces, and its geometric characteristics are more complex. During the process of seismic wave propagation, there will be more reflection and superposition between the two groups of surfaces, which is more complicated than the normal engineering slope. Considerably, the significant increase in the PGA amplification factor prompts the installation of

monitoring devices to achieve a better illustration of the effect.

It can also be shown in Figure 12 that, at the point of geometric structure mutation, the PGA amplification factor changes significantly even if the elevation remains constant, such as M3 and M4, between M11 and M12. Although they are located at the same height, their PGA amplification coefficient difference is very large. This finding further indicates that the geometry of the rock mass has a considerable influence on its seismic dynamic response. From the top of the grottoes to the top of the model, the PGA amplification factor decreases sharply, which indicates that the seismic wave dissipates more at the location of the rock at the top of the ear grottoes.

The analysis of the PGA amplification coefficient of the anchor-reinforced cliff body and original cliff body reveals that the PGA amplification coefficient of the anchor-reinforced cliff body and cliff body without anchoring is different but still retains the original cliff body distribution characteristics of the PGA amplification coefficient. The PGA amplification coefficient shows a decreasing trend after the initial increase, and in the elevation range of ear grottoes, the PGA amplification factor is relatively large.

3.3. Axial Force Response of the Bolt. By the analysis of the displacement and acceleration response of the anchor-reinforced cliff body, it can be seen that the anchoring effect of the small bolt is not fully exerted, and the axial force response of the bolt is small. The axial force distribution of the bolt is shown in Figure 13. With regard to the overall distribution, most of the bolt axial force is still small at both ends and large in the middle, with a smaller bolt axial force. As reflected by one of the most significant axial forces, the force of the no. 51 bolt (Figure 13(e)) is only 60.42 N, which is substantially less than its design load of 40 kN. This small axial force does not fully exhibit its anchoring effect. The analysis confirms that the bolt has no significant effect on the seismic reinforcement. The analysis results of the axial force of the bolts among different groups indicate that the maximum axial force of the bolts in each group decreases, which is consistent with the increase in elevation and is similar to the distribution law of the axial force of the bolts in the homogeneous anchored slope [15].

4. Conclusion

As indicated by this analysis, the horizontal displacement of the anchor-reinforced cliff body is increasing rather than decreasing; this trend is also observed in the region without the anchor support. This condition is attributed to the difference in the seismic wave propagation caused by the changes in the material properties of the original cliff body after installation of the anchor support. The change in the material properties of the rock mass causes a difference between the distribution of the PGA amplification factor of the reinforced anchor and the original cliff body. Consequently, the use of small bolts for the reinforcement method has no significant influence on the horizontal displacement responses of the grottoes calculated in this study. However, in the vertical direction, there is a certain angle between the bolt and the horizontal direction that can have a certain role in the vertical direction. Within the whole process of seismic action, the uneven settlement of the anchor is controlled to some extent, but the final results show that the seismic effect of the anchor is not ideal.

According to the existing literature, bolt support mainly changes or improves the structural characteristics of the rock mass. Because the fracture and structural plane characteristics of the grotto rock mass are not considered in this study, the structural characteristics of the upper rock mass of the cliff body are not significantly improved in the horizontal direction even with the support of the bolt. Otherwise,

within the vertical direction, ear grotto digging produces a discontinuous rock mass defect. Although the force of the bolt in the vertical direction is not large, it still has a certain controlling effect on the uneven settlement of the upper rock mass and can prevent fracture between the inner rock mass and outer rock mass at the top of the grotto. In addition, as the axial force of the bolt is directly related to the relative displacement of the rock around the bolt, with the relatively small displacement of the rock in the cliff body, the axial force response of the bolt is quite small with no indication of its supporting role.

With this calculation model, this kind of support with small bolts cannot reduce the relative displacement of the upper rock mass of the grotto cliff body in the horizontal direction. However, in the vertical direction, the support has a certain role in controlling the uneven settlement of the upper rock mass. The axial force in the bolt is very small, which also indicates that its supporting effect on the rock mass has not been fully realized.

By observing the structural defects in the vertical direction of the cliff body caused by the grotto excavation, the inclined angle of the bolt should be increased as far as possible or the vertical support should be adopted to enhance the stability of the rock mass at the top of the grotto. The results show that the anchoring effect of the bolt on the slope is mainly reflected in changing or improving the structural characteristics of the rock mass under the action of an earthquake.

Data Availability

All the relevant data underlying this research are included within this paper.

Conflicts of Interest

The authors declare that they have no conflicts of interest.

Acknowledgments

This study was financed by the National Natural Science Foundation of China (no. 51808246), National Key Research and Development Program of China (no. 2019YFC1520500), Research Project of China Railway Academy Co., Ltd. (no. 2020KJ009Z009A2), the Six Talent Peaks Project in Jiangsu Province of China (no. JZ-011), the New Wall Materials and Bulk Cement Support Projects of Jiangsu Province (no. 2017-21), and the Open Fund of Jiangsu Engineering Laboratory of Assembly Technology on Urban and Rural Residence Structure (no. JSZP201901).

References

- [1] F. Gao, Y. C. Shi, K. Wei, and R. D. Qiu, "The influence of anchor bolt supports on seismic responses of strengthening grottoes," *World Earthquake Engineering*, vol. 22, no. 2, pp. 84–88, 2006, in Chinese.
- [2] W. Chen, Z. Q. Guo, J. K. Zhang, and F. He, "Evaluation of long-term stability of Mogao grottoes caves under enhanced

- loading conditions of tourists,” *Journal of Performance of Constructed Facilities*, vol. 32, no. 4, 2018.
- [3] C. S. Christoforou, L. G. Salmon, and G. R. Cass, “Deposition of atmospheric particles within the Buddhist cave temples at Yungang, China,” *Atmospheric Environment*, vol. 28, no. 12, pp. 2081–2091, 1994.
- [4] R. Z. Liu, B. J. Zhang, H. Zhang, and M. F. Shi, “Deterioration of Yungang grottoes: diagnosis and research,” *Journal of Cultural Heritage*, vol. 12, no. 4, pp. 494–499, 2011, in Chinese.
- [5] Z. Huang, *Stabilizing of Rock Cavern Roofs by Rock Bolts*, Norwegian University of Science and Technology, Trondheim, Norway, 2001.
- [6] Y. Shi, R. Qiu, J. Sun, and M. Hu, “Analysis of dynamic response of dangerous rock mass reinforced by prestressed anchor cables under seismic loads,” *Rock and Soil Mechanics*, vol. 32, no. 4, pp. 1157–1162, 2011, in Chinese.
- [7] X. Wang, Q. Guo, S. Yang, Q. Pei, and Y. Fan, “The engineering geological problems and conservation of cliff face of Dunhuang Mogao Grottoes, China,” *Engineering Geology for Society and Territory*, vol. 8, pp. 183–187, 2015.
- [8] Q.-L. Guo, X.-D. Wang, H.-Y. Zhang, Z.-X. Li, and S.-L. Yang, “Damage and conservation of the high cliff on the northern area of Dunhuang Mogao grottoes, China,” *Landslides*, vol. 6, no. 2, pp. 89–100, 2009.
- [9] L. Li, J. Du, H. Liu, R. Chen, and T. Liu, “Dynamic characteristics and seismic responses of painted sculptures of Dunhuang Mogao Grottoes,” *Journal of Cultural Heritage*, vol. 22, pp. 1040–1048, 2016.
- [10] Q. X. Liu, Y. H. Duan, and J. Y. Deng, “Geological protection project of the longmen grottoes in Luoyang,” *Advanced Materials Research*, vol. 594-597, pp. 155–160, 2012.
- [11] J. Huang, “Study on the geological characteristics of Yungang grottoes,” *Southeast Culture*, vol. 5, pp. 91–93, 2003, in Chinese.
- [12] E. Yan and Y. Fang, “Quantitative evaluation on the safety of the column rock masses in Yungang Grotto,” *Chinese Journal of Rock Mechanics and Engineering*, vol. 23, no. s2, pp. 5046–5049, 2004, in Chinese.
- [13] X. Yang, T. Peng, G. Li et al., “Study on long term strength of pillar rockmass at Yungang Grottoes,” *Chinese Journal of Rock Mechanics and Engineering*, vol. 28, no. s2, pp. 3402–3408, 2009, in Chinese.
- [14] Itasca, *FLAC3D Version 4.0 (Fast Lagrangian Analysis of Continua in 3 Dimensions) User’s Manual*, Itasca Consulting Group Inc, Minneapolis, MN, USA, 2009.
- [15] H. Ye, Y. Zheng, X. Lu, and A. Li, “Shaking table test on anchor bars of slope under earthquake,” *China Civil Engineering Journal*, vol. 44, pp. 152–157+176, 2011.